



## TOPICAL REVIEW

## OPEN ACCESS







## Point defects, compositional fluctuations, and secondary phases in non-stoichiometric kesterites

RECEIVED  
8 April 2019REVISED  
23 May 2019ACCEPTED FOR PUBLICATION  
2 October 2019PUBLISHED  
10 December 2019

Original content from this work may be used under the terms of the [Creative Commons Attribution 3.0 licence](#).

Any further distribution of this work must maintain attribution to the author(s) and the title of the work, journal citation and DOI.



Susan Schorr<sup>1,2</sup> , Galina Gurieva<sup>1</sup> , Maxim Guc<sup>3,4</sup> , Mirjana Dimitrievska<sup>3,5,6</sup>,  
Alejandro Pérez-Rodríguez<sup>3,7</sup>, Victor Izquierdo-Roca<sup>3</sup>, Claudia S Schnohr<sup>8</sup> , Juran Kim<sup>9</sup>, William Jo<sup>9</sup>  and  
José Manuel Merino<sup>10</sup> 

<sup>1</sup> Department Structure and Dynamics of Energy Materials, Helmholtz-Zentrum Berlin fuer Materialien und Energie, Hahn-Meitner-Platz 1, 14109 Berlin, Germany

<sup>2</sup> Institute of Geosciences, Freie Universität Berlin, Malteserstr. 74-100, 12449 Berlin, Germany

<sup>3</sup> Catalonia Institute for Energy Research (IREC), Jardins de les Dones de Negre 1, 08930 Sant Adrià de Besòs, Spain

<sup>4</sup> Institute of Applied Physics, Academiei str. 5, MD 2023 Chisinau, Moldova

<sup>5</sup> NIST Center for Neutron Research, National Institute of Standards and Technology, Gaithersburg, MD 20899-6102, United States of America

<sup>6</sup> National Renewable Energy Laboratory, Golden, CO 80401, United States of America

<sup>7</sup> IN<sup>2</sup>UB, Departament d'Enginyeria Electrònica i Biomèdica, Universitat de Barcelona, C. Martí i Franquès 1, 08028 Barcelona, Spain

<sup>8</sup> Felix Bloch Institute for Solid State Physics, Leipzig University, Linnéstraße 5, 04103 Leipzig, Germany

<sup>9</sup> Department of Physics, Ewha Womans University, Seoul 03760, Republic of Korea

<sup>10</sup> Faculty of Science, Universidad Autónoma de Madrid, Ciudad Universitaria de Cantoblanco C/Francisco Tomás y Valiente 7, 28049 Madrid, Spain

E-mail: [susan.schorr@helmholtz-berlin.de](mailto:susan.schorr@helmholtz-berlin.de)

**Keywords:** kesterites, point defects, stoichiometry deviations, secondary phases, diffraction, Raman spectroscopy, Kelvin probe force microscopy

## Abstract

The efficiency of kesterite-based solar cells is limited by various non-ideal recombination paths, amongst others by a high density of defect states and by the presence of binary or ternary secondary phases within the absorber layer. Pronounced compositional variations and secondary phase segregation are indeed typical features of non-stoichiometric kesterite materials. Certainly kesterite-based thin film solar cells with an off-stoichiometric absorber layer composition, especially Cu-poor/Zn-rich, achieved the highest efficiencies, but deviations from the stoichiometric composition lead to the formation of intrinsic point defects (vacancies, anti-sites, and interstitials) in the kesterite-type material. In addition, a non-stoichiometric composition is usually associated with the formation of an undesirable side phase (secondary phases). Thus the correlation between off-stoichiometry and intrinsic point defects as well as the identification and quantification of secondary phases and compositional fluctuations in non-stoichiometric kesterite materials is of great importance for the understanding and rational design of solar cell devices. This paper summarizes the latest achievements in the investigation of identification and quantification of intrinsic point defects, compositional fluctuations, and secondary phases in non-stoichiometric kesterite-type materials.

## Introduction

This work focuses on structural variations in kesterite-type compound semiconductors, in particular Cu/Zn disorder and intrinsic point defects, as well as on compositional variations, in particular stoichiometry deviations in the kesterite-type phase and the segregation of related binary and ternary phases.

This review provides the vital approaches by discussing results and trends concerning intrinsic point defects and structural disorder, compositional fluctuations, and secondary phases on a macroscopic and microscopic scale and even on the nano-scale. Various analytical methods have been used in these studies.

The review comprises five parts:

- A. Crystal structure, structural disorder, and intrinsic point defects in kesterites
- B. Raman spectroscopy investigations on kesterites

- C. Homogeneity of kesterites studied by synchrotron-based techniques
- D. Homogeneity of kesterites investigated by Kelvin probe force microscopy (KPFM)
- E. Ellipsometry and band structure of kesterites

## A. Crystal structure, structural disorder, and intrinsic point defects in kesterites

### 1. Introduction

#### 1.1. Crystal structure

The compound semiconductors  $\text{Cu}_2\text{ZnSnS}_4$  (CZTS),  $\text{Cu}_2\text{ZnSnSe}_4$  (CZTSe),  $\text{Cu}_2\text{ZnGeSe}_4$  (CZGeSe) as well as the solid solution series  $\text{Cu}_2\text{ZnSn}(\text{S}, \text{Se})_4$  (CZTSSe) crystallize in the kesterite-type structure (space group  $I\bar{4}$ ) [1–4]. In this type of structure, one Cu occupies the 2a (0, 0, 0) position, with Zn and the remaining Cu ordered at 2d (0,  $\frac{1}{4}$ ,  $\frac{3}{4}$ ) and 2c (0,  $\frac{1}{2}$ ,  $\frac{1}{4}$ ) respectively, Sn is located at 2b (0, 0,  $\frac{1}{2}$ ) and the anion lies on the 8g (x, y, z) position [5] (see figure 1, middle). Due to this cation arrangement, the kesterite-type structure is characterized by alternating cation layers of Cu–Sn, Cu–Zn, Cu–Sn, Cu–Zn, and Cu–Sn at  $z = 0, \frac{1}{4}, \frac{1}{2}, \frac{3}{4}$  and 1 (figure 1, left). Because of the small difference between the atomic coordinates x and y of the anion position (x, y, z) (in space group  $I\bar{4}$ ) in CZTS and CZTSe, the anion position in those compounds might be described with (x, x, z) which would result in the space group  $I\bar{4}2m$  [1, 2].

#### 1.2. Cu/Zn disorder

In CZTS, CZTSe, CZTSSe as well as in CZGeSe it has been found experimentally by neutron diffraction, that a ‘Cu/Zn disorder’ occurs in the layers at  $z = \frac{1}{4}$  and  $\frac{3}{4}$  resulting in  $\text{Zn}_{\text{Cu}}$  and  $\text{Cu}_{\text{Zn}}$  anti-sites on the Wyckoff positions 2c and 2d (figure 1, right) [1–4]. Because of this disorder the term ‘disordered kesterite’ has arisen [6]. The degree of disorder, which can be expressed by the order parameter Q with

$$Q = \frac{[\text{Cu}_{2c} + \text{Zn}_{2d}] - [\text{Zn}_{2c} + \text{Cu}_{2d}]}{[\text{Cu}_{2c} + \text{Zn}_{2d}] + [\text{Zn}_{2c} + \text{Cu}_{2d}]}$$

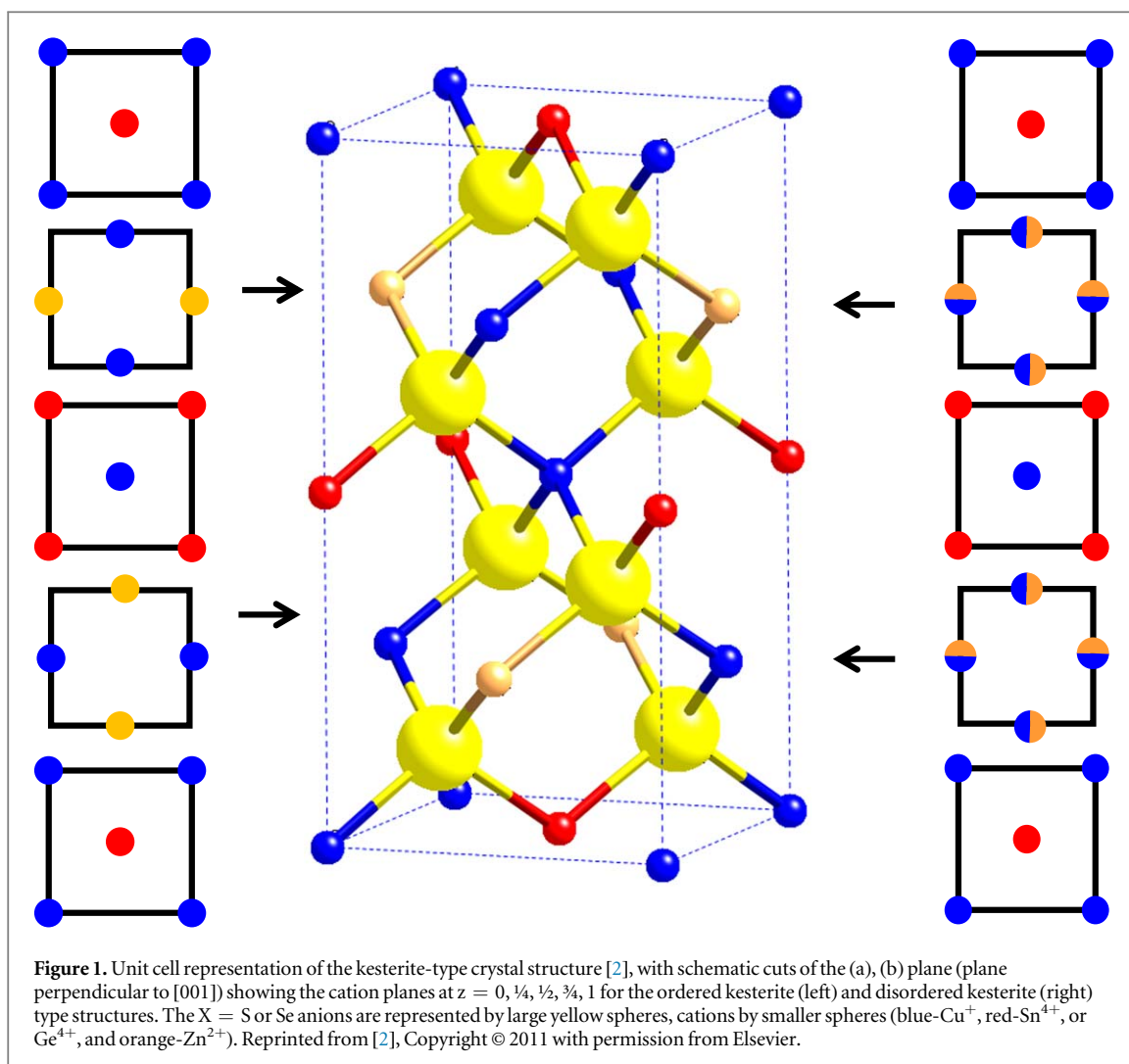
depending on the synthesis parameters, especially the annealing temperature [7]. The first hint of a temperature dependent change in the cation arrangement within the kesterite-type structure was observed in CZTS by *in situ* synchrotron x-ray diffraction (XRD) [8]. In this study the lattice parameter *a* shows a linear increase with increasing temperature, but for the lattice parameter *c* a kink was observed at about 250 °C. Later on an order–disorder phase transition was proved at  $259 \pm 10$  °C in CZTS [9] and at  $200 \pm 20$  °C in CZTSe [10]. Both studies are based on Raman spectroscopy which is an indirect method to investigate the order–disorder transition in a qualitative way. Anomalous XRD studies on CZTSe have shown the order–disorder transition at  $203 \pm 6$  °C [11]. This method allows not only a qualitative but also a quantitative investigation of the Cu/Zn disorder. The Cu/Zn disorder influences the optoelectronic properties like band gap energy [10] and band gap fluctuations [11].

#### 1.3. Stoichiometry deviations and the off-stoichiometry model

The best performing kesterite-based thin film solar cells were obtained with a material quite different from the stoichiometric compound, especially with a Cu-poor/Zn-rich composition [12]. Such deviations from the stoichiometric composition lead to the formation of intrinsic point defects (vacancies, anti-sites, and interstitials) in the compound, which significantly influence the electrical and optical properties of the material [13, 14]. The formation of such defects is driven thermodynamically by minimizing the Gibbs free energy of the crystal. Moreover the formation of secondary phases is highly probable. The correlation between off-stoichiometry and intrinsic point defects is of great importance for the understanding and rational design of solar cell devices.

The existence of off-stoichiometric CZTS, CZTSe, CZTSSe, and CZGeSe has been shown in extended and systematic studies of powder series [3, 4, 15, 16]. These investigations proved the ability of kesterite-type compounds to tolerate deviations from stoichiometric composition keeping the kesterite-type structure but showing cation ratios  $\text{Cu}/(\text{Zn} + \text{Sn})$  and  $\text{Zn}/\text{Sn}$  lower or higher than 1. The ‘cation ratio plot’ (figure 2) is used to illustrate the off-stoichiometry in kesterite-type materials.

The structural flexibility originates from the propensity of the kesterite-type structure to stabilize copper vacancies, anti-sites, and interstitials. In these compounds, the charge balance is ensured by appropriate substitutions on the cationic sites. If the oxidation states of cations and anions are retained in off-stoichiometric



kesterites, only certain substitutions can be envisioned to account for the charge balance in the off-stoichiometric material. Thus the off-stoichiometric composition corresponds to certain point defects. This correlation is the basis for the ‘off-stoichiometry model,’ first proposed by Lafond *et al* [17]. A summary of the off-stoichiometry types, referred to as A–L [16], is presented in table 1.

The limits of the structural flexibility of the kesterite-type structure were examined in CZTSe [18]. In this study it was shown that the synthesis of CZTSe powder material with an intended far off-stoichiometric composition ( $0.4 \leq \text{Cu}/(\text{Zn} + \text{Sn}) \leq 2.0$  and  $0.33 \leq \text{Zn}/\text{Sn} \leq 3$ ) ended up in much less off-stoichiometric kesterite-type phases and co-existing secondary phases. According to this study CZTSe kesterite-type phases with an off-stoichiometric composition are always within the rectangle  $0.6 \leq \text{Cu}/(\text{Zn} + \text{Sn}) \leq 1.7$  and  $0.5 \leq \text{Zn}/\text{Sn} \leq 1.6$ .

## 2. Determination of type of intrinsic point defect and concentration by neutron diffraction

Elastic coherent neutron scattering (neutron diffraction) allows a non-destructive analysis of the crystal structure of photovoltaic absorber materials like kesterites from the surface deep into the volume of the sample. With the use of neutrons a differentiation between the electronic similar elements copper and zinc in the crystal structure is possible. Our systematic studies are based on powder sample series synthesized by solid state reaction, neutron powder diffraction measurements, their Rietveld analysis as well as the application of the average neutron scattering length analysis method [19].

The general formulae for the calculation of the average neutron scattering length  $\bar{b}_j$  of a crystallographic site  $j$  is as follows:

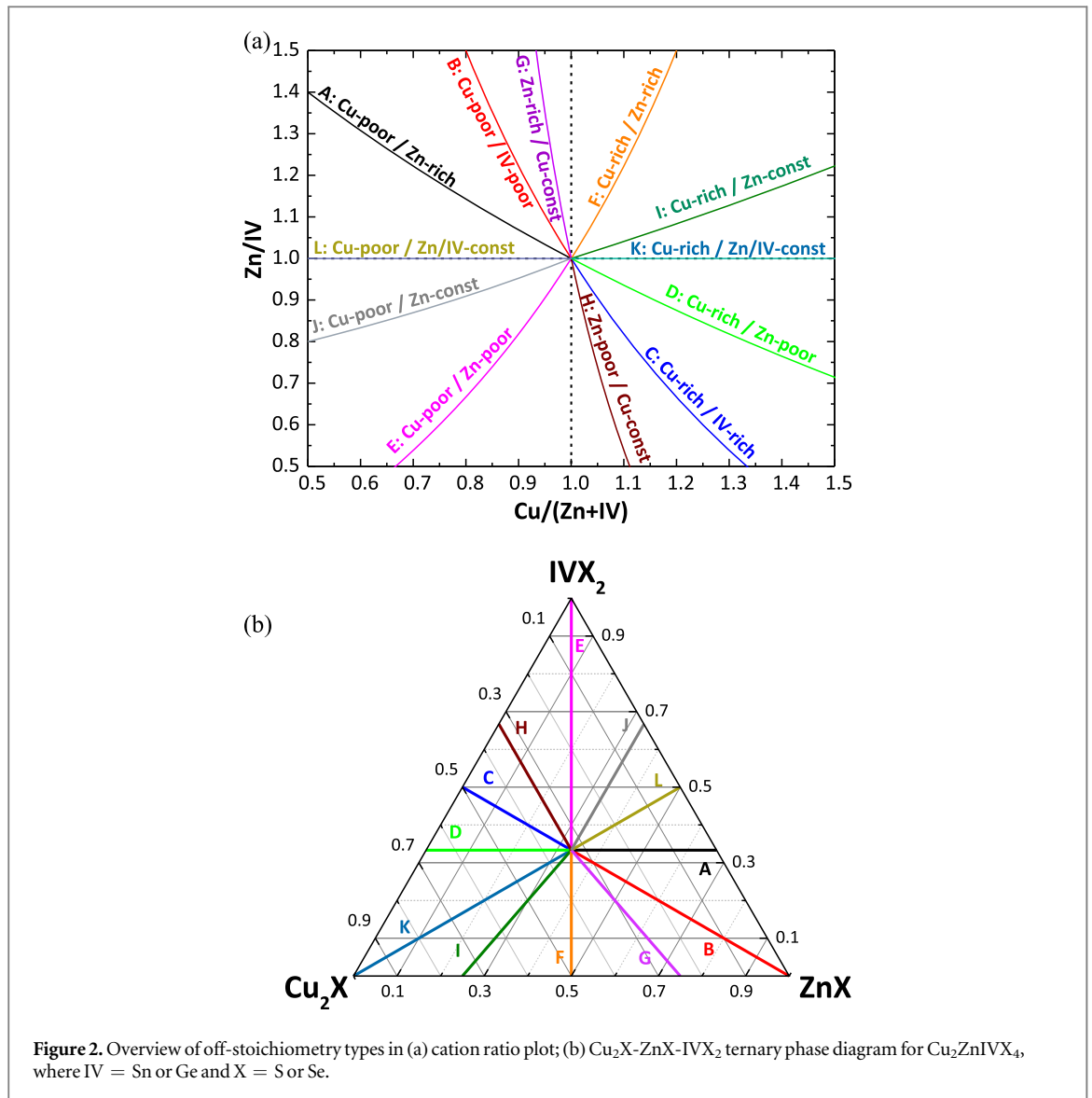


Figure 2. Overview of off-stoichiometry types in (a) cation ratio plot; (b)  $\text{Cu}_2\text{X-ZnX-IVX}_2$  ternary phase diagram for  $\text{Cu}_2\text{ZnIVX}_4$ , where IV = Sn or Ge and X = S or Se.

$$\bar{b}_j = A_j \cdot b_A + B_j \cdot b_B + V_j,$$

where  $A$  and  $B$  are two different cations,  $b_A$  and  $b_B$  are the coherent neutron scattering lengths of the cations  $A$  and  $B$ ,  $V$  represents possible vacancies, and  $j$  stands for the Wyckoff position. The following equations were derived for the calculation of the experimental average neutron scattering lengths  $\bar{b}_j^{\text{exp}}$  for a material with kesterite-type structure ( $j = 2a, 2c, 2d$ ), for example CZTS or CZTSe:

$$\begin{aligned} \bar{b}_{2a}^{\text{exp}} &= \text{SOF}_{2a} \cdot b_{\text{Cu}} & \bar{b}_{2b}^{\text{exp}} &= \text{SOF}_{2b} \cdot b_{\text{Sn}} \\ \bar{b}_{2c}^{\text{exp}} &= \text{SOF}_{2c} \cdot b_{\text{Zn}} & \bar{b}_{2d}^{\text{exp}} &= \text{SOF}_{2d} \cdot b_{\text{Cu}}. \end{aligned}$$

The cation site occupancy values  $\text{SOF}_j$  result from the Rietveld analysis of neutron diffraction data. Based on the cation distribution according to the off-stoichiometry model the kesterite-type compound belongs to, an average neutron scattering length can be calculated

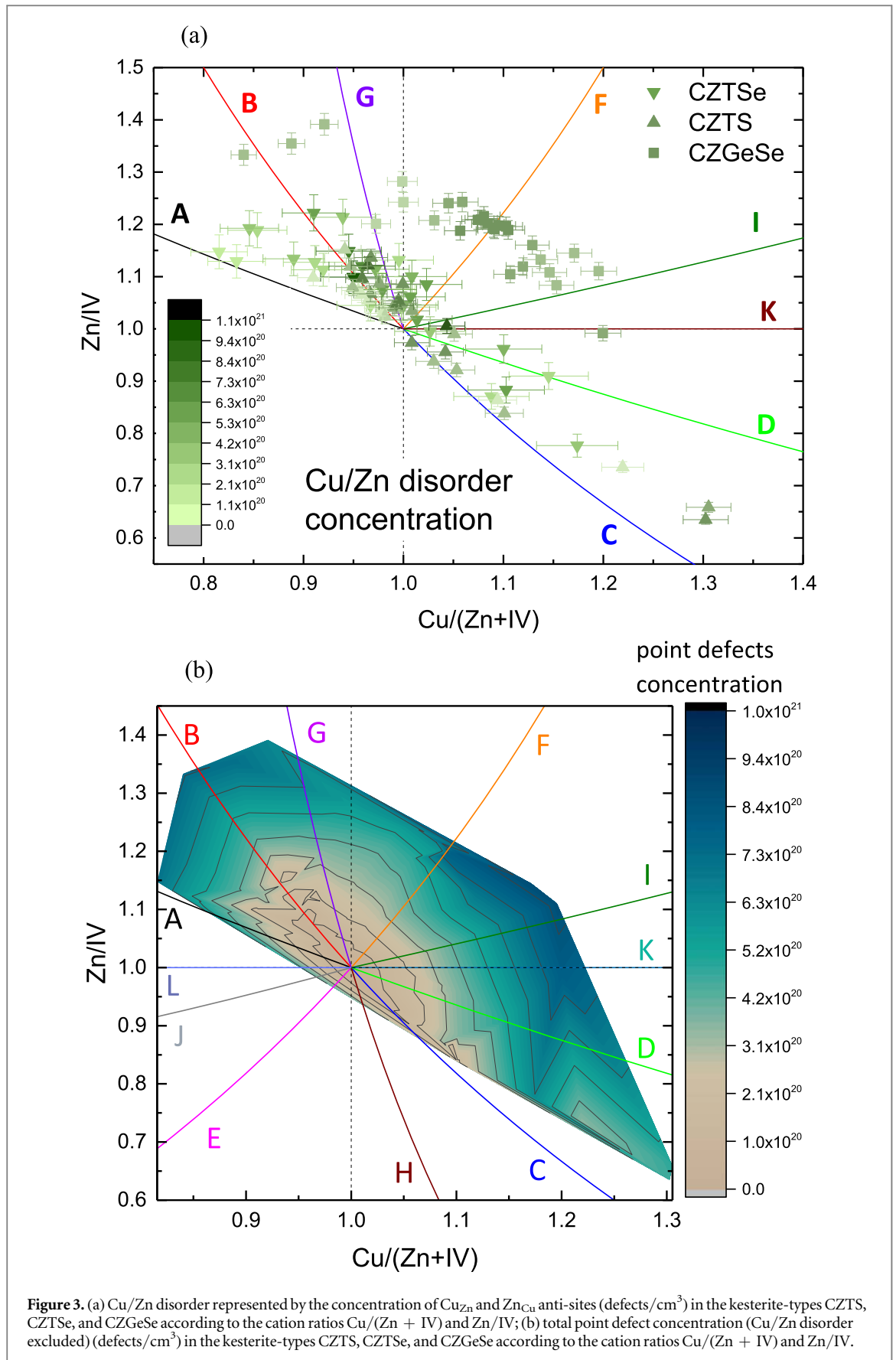
$$\bar{b}_j^{\text{calc}} = \sum_k (k)_j^{\text{model}}$$

where  $(k)_j^{\text{model}}$  is the fraction of the cation  $k$  on the crystallographic site  $j$  ( $2a, 2b, 2c, 2d$ ) and  $b_k$  is the neutron scattering length of the cation  $k$ . In this calculation two additional requirements have to be taken into account: (1) each cation site is fully occupied by cations or by cations and vacancies ( $(k)_j^{\text{model}} + V_j^{\text{model}} = 1$ ,  $V$  stands for vacancies) and (2) the sum of a cation species in the model is the cation species amount measured by wavelength dispersive spectroscopy (WDX) in the chemical analysis of the sample

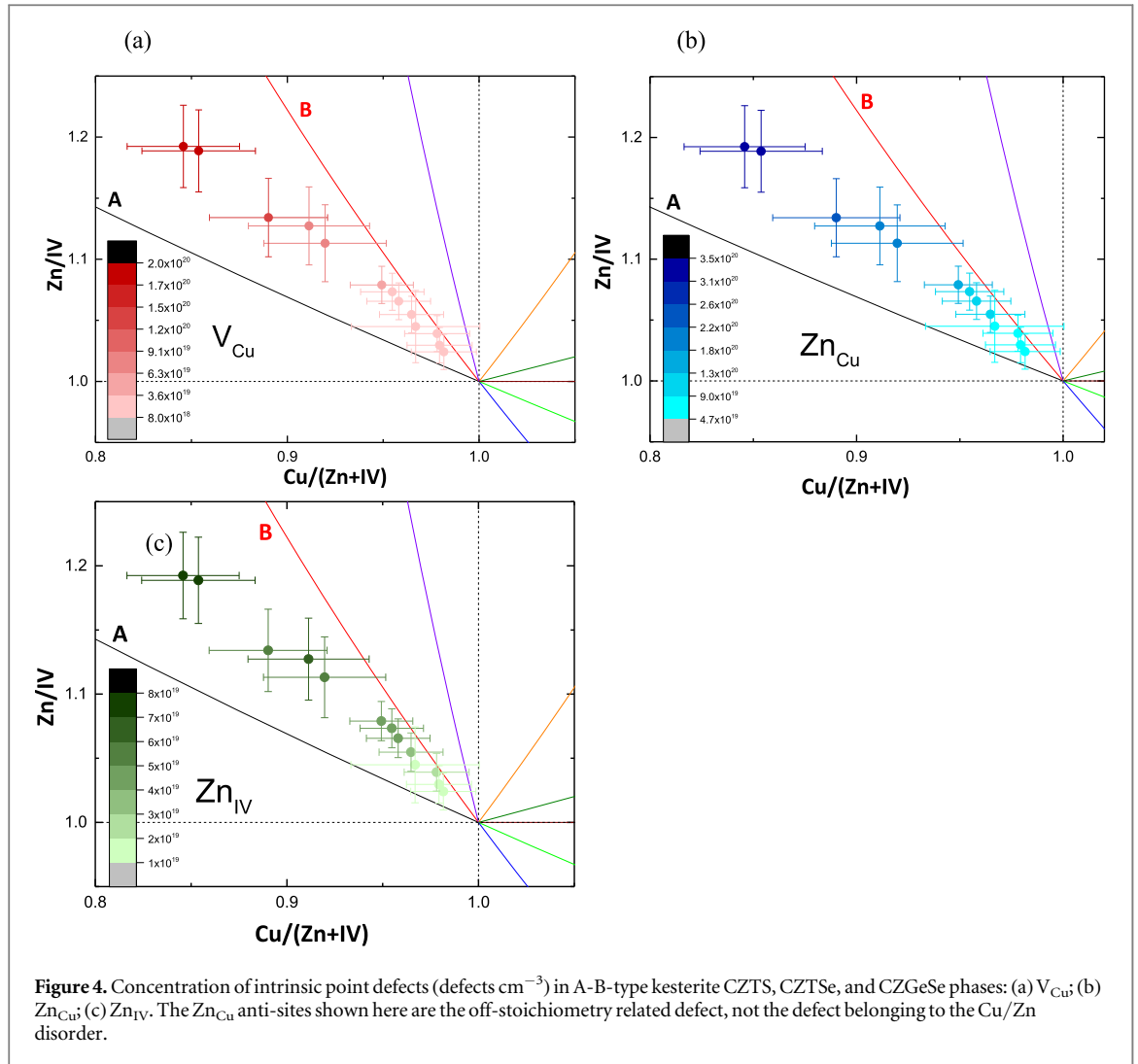
$$\sum_j (k)_j^{\text{model}} = k^{\text{WDX}}.$$

**Table 1.** Overview of off-stoichiometry types in kesterite-type  $\text{Cu}_2\text{ZnIVX}_4$ , where IV = Sn or Ge and X = S or Se.

Type	Composition	Cation substitution reaction	Intrinsic point defect	Chemical formulae
A	Cu-poor, Zn-rich, IV-const.	$2\text{Cu}^+ \rightarrow \text{Zn}^{2+}$	$\text{V}_{\text{Cu}} + \text{Zn}^{2+}_{\text{Cu}}$	$\text{Cu}_{2-2a}\text{Zn}_{1+a}\text{IVX}_4$
B	Cu-poor, Zn-rich, IV-poor	$2\text{Cu}^+ + \text{IV}^{4+} \rightarrow 3\text{Zn}^{2+}$	$2\text{Zn}^{2+}_{\text{Cu}} + \text{Zn}^{2+}_{\text{IV}}$	$\text{Cu}_{2-2b}\text{Zn}_{1+3b}\text{IV}_{1-b}\text{X}_4$
C	Cu-rich, Zn-poor, IV-rich	$3\text{Zn}^{2+} \rightarrow 2\text{Cu}^+ + \text{IV}^{4+}$	$2\text{Cu}^+_{\text{Zn}} + \text{IV}^{4+}_{\text{Zn}}$	$\text{Cu}_{2+2c}\text{Zn}_{1-3c}\text{IV}_{1+c}\text{X}_4$
D	Cu-rich, Zn-poor, IV-const.	$\text{Zn}^{2+} \rightarrow 2\text{Cu}^+$	$\text{Cu}^+_{\text{Zn}} + \text{Cu}_i$	$\text{Cu}_{2+2d}\text{Zn}_{1-d}\text{IVX}_4$
E	Cu-poor, Zn-poor, IV-rich	$2\text{Cu}^+ + \text{Zn}^{2+} \rightarrow \text{IV}^{4+}$	$2\text{V}_{\text{Cu}} + \text{Zn}^{2+}_{\text{IV}} \text{ or } \text{IV}^{4+}_{\text{Cu}} + \text{V}_{\text{Cu}} + \text{V}_{\text{Zn}}$	$\text{Cu}_{2-2e}\text{Zn}_{1-e}\text{IV}_{1+e}\text{X}_4$
F	Cu-rich, Zn-rich, IV-poor	$\text{IV}^{4+} \rightarrow \text{Zn}^{2+} + 2\text{Cu}^+$	$\text{Zn}^{2+}_{\text{IV}} + 2\text{Cu}^+_i \text{ or } \text{Cu}^+_{\text{IV}} + \text{Cu}^+_i + \text{Zn}^{2+}_i$	$\text{Cu}_{2+2f}\text{Zn}_{1+f}\text{IV}_{1-f}\text{X}_4$
G	Cu-const., Zn-rich, IV-poor	$\text{IV}^{4+} \rightarrow 2\text{Zn}^{2+}$	$\text{Zn}^{2+}_{\text{IV}} + \text{Zn}^{2+}_i$	$\text{Cu}_2\text{Zn}_{1+2g}\text{IV}_{1-g}\text{X}_4$
H	Cu-const., Zn-poor, IV-rich	$2\text{Zn}^{2+} \rightarrow \text{IV}^{4+}$	$\text{IV}^{4+}_{\text{Zn}} + \text{V}_{\text{Zn}}$	$\text{Cu}_2\text{Zn}_{1-h}\text{IV}_{1+1/2h}\text{X}_4$
I	Cu-rich, Zn-const., IV-poor	$\text{IV}^{4+} \rightarrow 4\text{Cu}^+$	$\text{Cu}^+_{\text{IV}} + 3\text{Cu}^+_i$	$\text{Cu}_{2+4i}\text{ZnIV}_{1-i}\text{X}_4$
J	Cu-poor, Zn-const., IV-rich	$4\text{Cu}^+ \rightarrow \text{IV}^{4+}$	$\text{IV}^{4+}_{\text{Cu}} + 3\text{V}_{\text{Cu}}$	$\text{Cu}_{2-2j}\text{Zn}_{1-j}\text{IV}_{1+1/2j}\text{X}_4$
K	Cu-rich, Zn/IV = 1 = const.	$\text{Zn}^{2+} + \text{IV}^{4+} \rightarrow 6\text{Cu}^+$	$\text{Cu}^+_{\text{Zn}} + \text{Cu}^+_{\text{IV}} + 4\text{Cu}^+_i$	$\text{Cu}_{2+6k}\text{Zn}_{1-k}\text{IV}_{1-k}\text{X}_4$
L	Cu-poor, Zn/IV = 1 = const.	$6\text{Cu}^+ \rightarrow \text{Zn}^{2+} + \text{IV}^{4+}$	$\text{Zn}^{2+}_{\text{Cu}} + \text{IV}^{4+}_{\text{Cu}}$	$\text{Cu}_{2-2l}\text{Zn}_{1+1/3l}\text{IV}_{1+1/3l}\text{X}_4$



In order to establish a reasonable cation distribution model, the experimental average neutron scattering lengths  $\bar{b}_j^{exp}$  and the calculated average neutron scattering lengths  $\bar{b}_j^{calc}$  are compared minimizing their difference by varying the cation fractions  $(k)_j^{model}$  (agreement within the experimental error). From the resulting cation



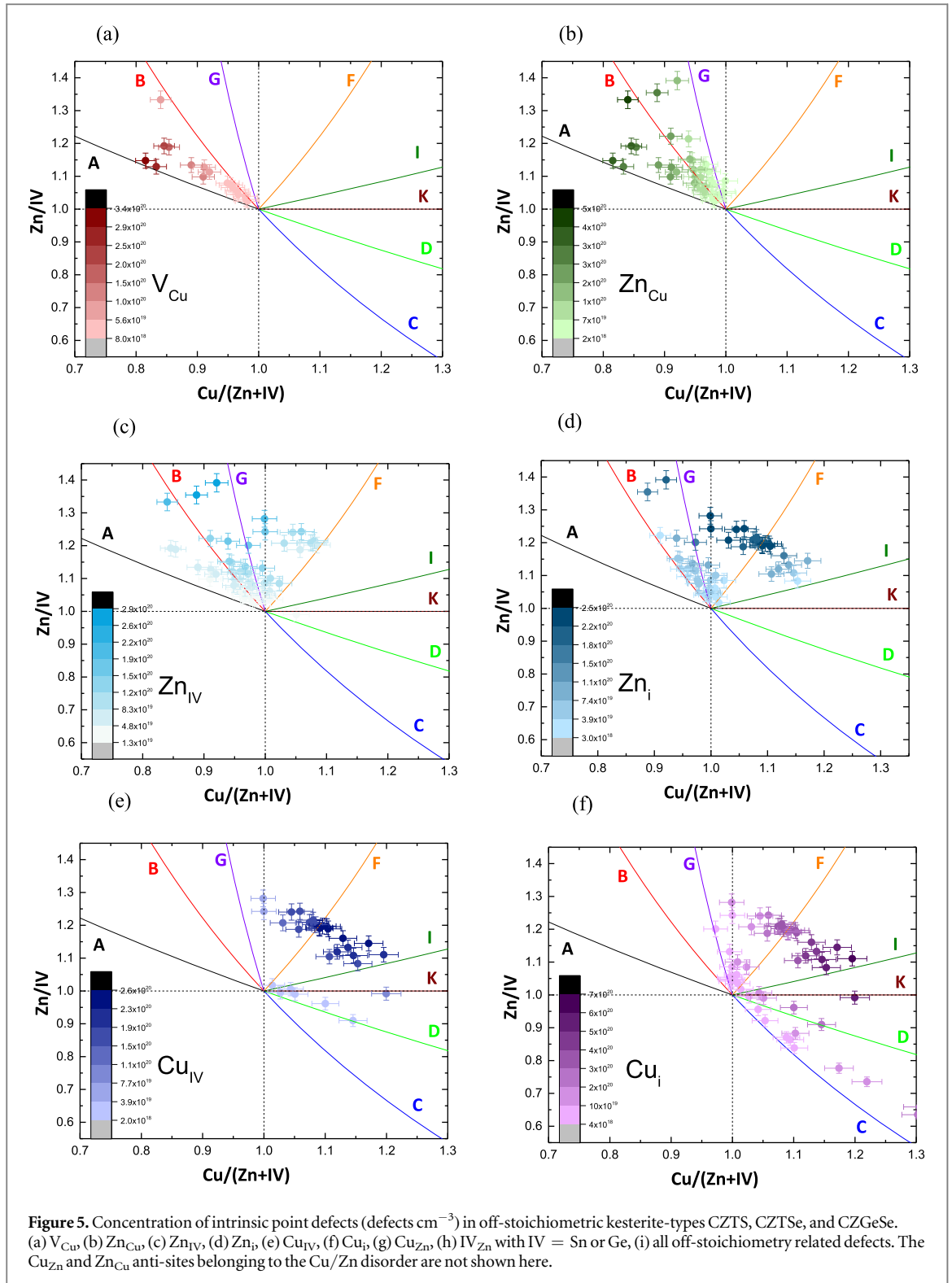
distribution ( $(k)_j^{\text{model}}$ ) the intrinsic point defects (ant-sites, vacancies) can be concluded. In the case of an excess of a cation species, i.e., the sum of a cation species distributed at the cation sites exceeds the amount determined by WDX, interstitials are assumed. The cation distribution model for all off-stoichiometric kesterite-type phases was deduced by this method, applying the same principles. In this way we were able to evaluate experimentally the off-stoichiometry and intrinsic point defect concentrations as well as the Cu/Zn disorder in kesterite-type semiconductors.

An overview of the experimentally observed intrinsic point defects in CZTS, CZTSe, and CZGeSe is presented in figure 3. Here a distinction is made between Cu/Zn disorder (figure 3(a) shows the concentration of  $\text{Cu}_{\text{Zn}}$  and  $\text{Zn}_{\text{Cu}}$  anti-sites causing the Cu/Zn disorder) and intrinsic point defects (vacancies, anti-sites, interstitials) belonging to an off-stoichiometry type (figure 3(b)). The following trends can be observed:

- (1) Cu-poor kesterites show less Cu/Zn disorder than Cu-rich kesterites.
- (2) The concentration of intrinsic point defects increases with increasing off-stoichiometry.

Figure 4 summarizes the intrinsic cation point defects determined in kesterite-types CZTS, CZTSe, and CZTGeSe whose cation ratios lie between the A-type and B-type lines in the cation ratio plot, which means they represent an A-B mixture. This compositional region is of special interest, because the integral composition of the absorber layer of best performing kesterite-based thin film solar cells lay in that area. According to the off-stoichiometry model, these kesterites contain copper vacancies  $V_{\text{Cu}}$ ,  $Zn_{\text{Cu}}$ , and  $Zn_{\text{IV}}$  (e. g.  $Zn_{\text{Sn}}$  or  $Zn_{\text{Ge}}$ ) anti-sites (see table 1). According to the results obtained by neutron diffraction the dominating point defects in A-B-type mixtures are copper vacancies and  $Zn_{\text{Cu}}$  anti-sites, both exhibiting shallow levels in the band gap [13]. As suggested in literature [13], these defects could form neutral defect clusters. Additional  $Zn_{\text{IV}}$  anti-site defects occur due to the B-type character present in A-B mixtures. In CZTS and CZTSe this defect is connected to deep





levels in the band gap which may act as traps [13]. With increasing off-stoichiometry in the A-B-type mixtures the concentration of intrinsic point defects increases gradually.

The experimentally determined intrinsic point defect concentrations for different off-stoichiometry CZTS, CZTSe, and CZGeSe kesterite phases are summarized in figure 5. It is obvious that the observed defect types agree very well with the defect types predicted by the off-stoichiometry model (table 1). The following conclusions can be deduced:

- (1) Copper vacancies ( $V_{\text{Cu}}$ ) exist within the A-B off-stoichiometry area only (A-B off-stoichiometry mixtures). The copper vacancy concentration decreases with increasing B-type fraction in these mixtures. Kesterite-type phases



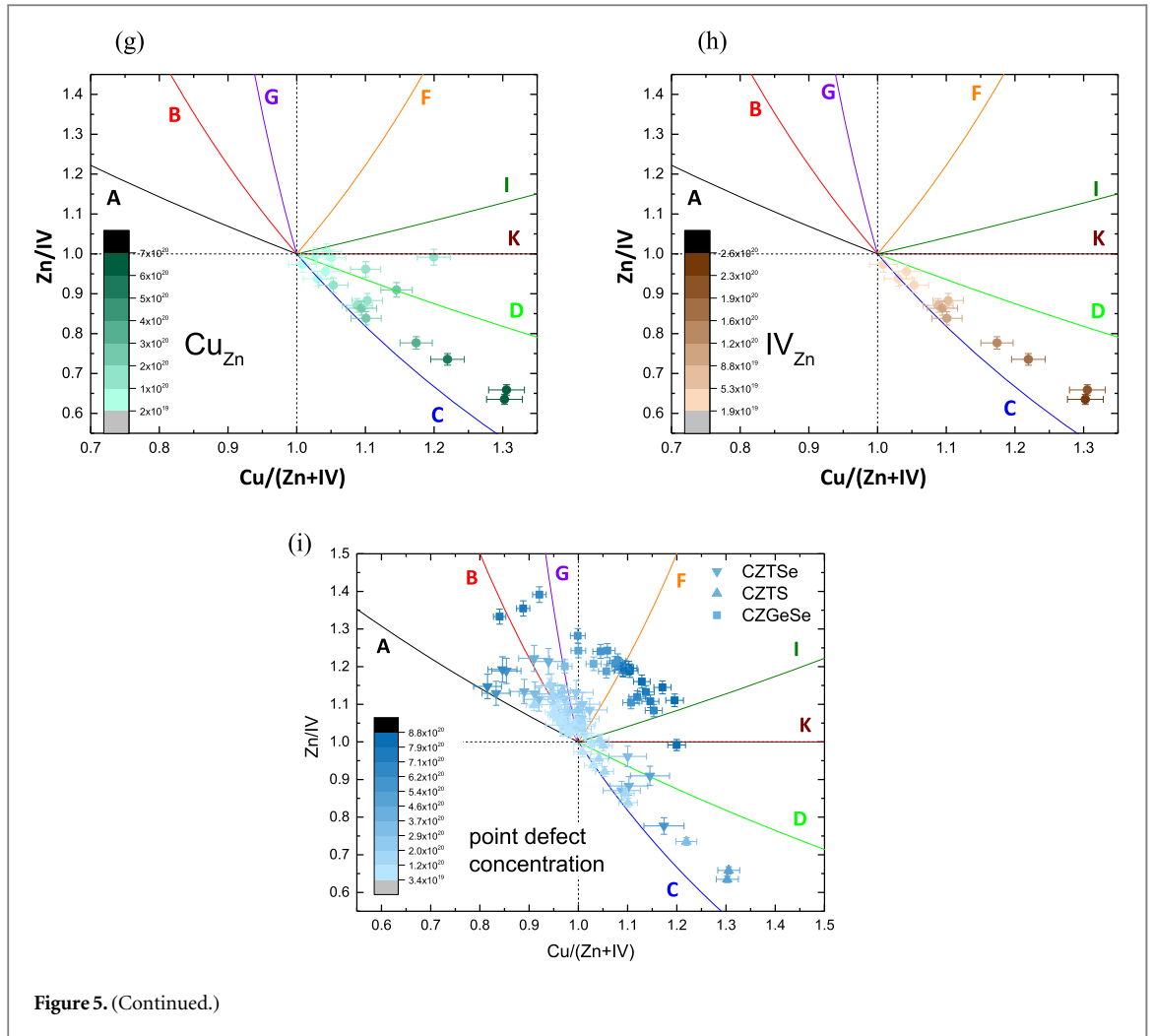


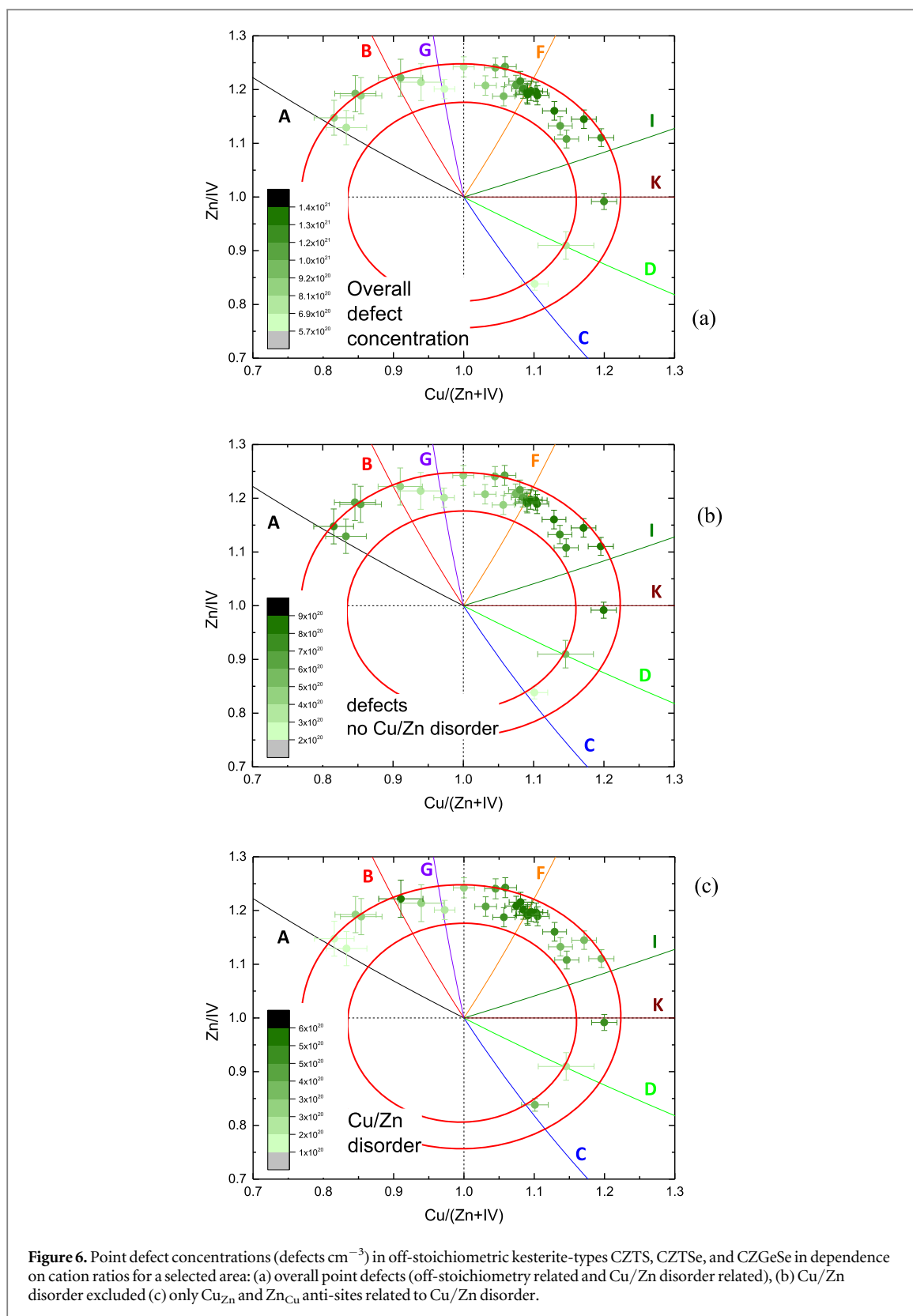
Figure 5. (Continued.)

within the B-G off-stoichiometry area are Cu-poor and Zn-rich as well, but there are no copper vacancies present.

- (2)  $Zn_{Cu}$  anti-sites (not related to Cu/Zn disorder) occur within the A-B-G off-stoichiometry area, but not in the Cu-poor and Zn-rich G-F off-stoichiometry area.
- (3)  $Zn_{IV}$  anti-sites (IV = Ge or Sn) exist mainly in the B-G-F off-stoichiometry area. In A-B off-stoichiometry mixtures this defect is only in the B-type rich kesterite-type phases present.
- (4)  $Cu_{IV}$  anti-sites (IV = Ge or Sn) occur in the G-F-I-K-D off-stoichiometry area. The highest concentration is reached in F-I off-stoichiometry mixtures.
- (5) Copper interstitials ( $Cu_i$ ) exist in Cu-rich kesterite-type phases regardless of whether they are Zn-poor or Zn-rich (G-F-I-K-L-D-C off-stoichiometry area). The highest concentration is reached for F-I and I-K off-stoichiometry mixtures.
- (6)  $Cu_{Zn}$  anti-sites (not related to Cu/Zn disorder) occur within the K-D off-stoichiometry area.
- (7)  $IV_{Zn}$  anti-sites (IV = Ge or Sn) occur only in D-C off-stoichiometry mixtures.

Comparing the intrinsic point defect concentration in kesterite-type CZTS, CZTSe, and CZGeSe phases with the same level of off-stoichiometry (see figure 6) then it becomes obvious, that Cu-rich/Zn-rich kesterites show the highest overall intrinsic point defect concentrations (i.e. vacancies, anti-sites, interstitials as well as  $Cu_{Zn}$  and  $Zn_{Cu}$  anti-sites caused by Cu/Zn disorder). The following trends can be observed:

- (1) The concentration of intrinsic point defects (without taking Cu/Zn disorder into account) is higher in A-B-type off-stoichiometric kesterites than in B-G and G-F-type off-stoichiometric kesterites.



In F-I-type off-stoichiometric kesterites the defect concentration increases to higher values than in A-B-type off-stoichiometric kesterites.

- (2) The Cu/Zn disorder is the lowest in kesterites with mainly A-type off-stoichiometry. It increases gradually from A-B over B-G and G-F-type off-stoichiometric kesterites and decreases afterward in F-I type kesterites again.

### 3. Conclusions

The systematic investigations by neutron diffraction revealed the structural origin of point defects in off-stoichiometric CZTS, CZTSe, CZTSSe, and CZGeSe kesterite phases. The correlations between the cation ratios of CZTS, CZTSe, and CZGeSe kesterite-type phases and occurring intrinsic point defects were clearly demonstrated. These established relationships which reflect the off-stoichiometry model, allow the prediction of the occurring intrinsic point defect types in kesterites only by chemical composition (cation ratios) of the kesterite phase.

Further progress in kesterite-based thin film devices could be inspired by these correlations showing dangerous compositional regions, even in the advantageous Cu-poor/Zn-rich range.

### B. Raman spectroscopy investigations on kesterites

#### 4. Introduction

First observations of the Raman scattering effect were made by Raman and his student Krishnan in organic liquids, and independently by Landsberg and Mandelstam in inorganic crystals in 1928 [20, 21]. Since then, Raman spectroscopy has become one of the leading techniques for the evaluation of vibrational properties in the materials. The details of Raman scattering theory and technical aspects of the spectroscopy were published in numerous books (e.g. see [22–25]), starting from the first systematic study performed by Placzek [26]. Raman scattering is a process caused by the interaction of light with a medium (gas, liquid, or solid), and it is related to the inelastic scattering of the photons on molecules or atoms vibrations [22]. In this way all the material's properties, which influence the vibrational properties, i.e. the phonons (quasiparticle of atoms or molecule vibration), can affect the Raman spectra.

The Raman spectrum presents the intensity of the inelastically scattered radiation from a material as a function of frequency (Raman shift), and for crystalline materials consists of the individual Lorentzian shaped peaks (physical representation of Raman modes) related to individual phonons. Spectral distribution of the Raman peak intensity can be expressed in the following way:

$$I(\omega) = \frac{2A}{\pi} \frac{\Gamma}{4(\omega - \omega_{ph})^2 + \Gamma^2}, \quad (1)$$

where  $\Gamma$  is the full width at half maximum (FWHM) of the Raman peak, related to the phonons lifetime,  $\omega_{ph}$  is the phonon frequency, and  $A$  is an amplitude, correlated with the phonons density of states. As Raman spectra presents a superposition of multiple vibrational modes, each of which can be modeled by a Lorentzian shaped peak, deconvolution of the spectra enables extracting individual peak parameters, which can be directly related to the vibrational properties of the material. Any changes in the material properties, will directly affect the vibrations, i.e. phonons of the material, which will then be evident in the changes of the Raman spectra. The vibrational signature of any crystalline material is directly defined by the crystal structure, and the number and type of atoms involved. The crystal structure, i.e. the symmetry of the lattice, determines the type of vibrations which can be found in a specific material, while the number of atoms in the unit cell will influence the number of phonons. Finally, the frequency or energy of a phonon is defined by the type of atoms, and thus by the chemical composition of the crystalline material. The later interconnection of the phonon energy with the chemical composition is more complex, as being produced through the interatomic bond length and the force constants related to the bond-stretching forces.

Analysis of the previously mentioned Raman peak parameters is also useful for determining suitable measurement conditions, which will not lead to damaging of the sample and false interpretations of the spectra. Taking into account increase in the popularity of micro Raman spectroscopy today, one of the critical measurement parameters became the applied excitation power density. This, being usually  $\sim 1$  mW, but concentrated on a micro spot of  $1\text{--}2$   $\mu\text{m}$  diameter, can reach a power density of  $\sim 100$   $\text{kW cm}^{-2}$ , and have a direct impact on the Raman spectra [27] (e.g. energy density of solar radiation  $\sim 10^{-4}$   $\text{kW cm}^{-2}$ ). Selection of suitable excitation power density strongly depends on excitation wavelength, materials absorption at this wavelength, and the sample morphology (nanosize, thin film, or bulk). In the case of semiconductor compounds, there is a considerable difference in the absorption below and above the band gap of the material. This distinct interaction between the excitation photons and the semiconductor material imposes different measuring conditions, in terms of the maximum excitation power that can be applied during the measurements without sample deterioration. Although the phonon frequency, and as a result the Raman peaks wavenumbers, are independent from the applied excitation wavelength, the difference in the interaction with excitation

**Table 2.** Irreducible representation for the zone-center ( $\Gamma$  point) phonon modes and mode classification in quaternary compounds crystallizing in different tetragonal crystal structures.

Crystal structure	Space group	Irreducible representation	Mode classification	
Kesterite	$I\bar{4}$ [32]	$3A_1 \oplus 7B_1 \oplus 7E$	Raman	$3A_1 \oplus 6B_1 \oplus 6E$
			IR	$6B_1 \oplus 6E$
			Acoustic	$B_1 \oplus E$
Stannite	$I\bar{4}2m$ [32, 33]	$2A_1 \oplus A_2 \oplus 2B_1 \oplus 5B_2 \oplus 7E$	Raman	$2A_1 \oplus 2B_1 \oplus 4B_2 \oplus 6E$
			IR	$4B_2 \oplus 6E$
			Acoustic	$B_2 \oplus E$
			Silent	$A_2$
PMCA	$P\bar{4}2m$ [34]	$2A_1 \oplus 2A_2 \oplus B_1 \oplus 5B_2 \oplus 7E$	Raman	$2A_1 \oplus B_1 \oplus 4B_2 \oplus 6E$
			IR	$4B_2 \oplus 6E$
			Acoustic	$B_2 \oplus E$
			Silent	$2A_2$
Disordered kesterite	$I\bar{4}2m$ [35]	$2A_1 \oplus A_2 \oplus 2B_1 \oplus 5B_2 \oplus 7E$	Raman	$2A_1 \oplus 2B_1 \oplus 4B_2 \oplus 6E$
			IR	$4B_2 \oplus 6E$
			Acoustic	$B_2 \oplus E$
			Silent	$A_2$
—	$P\bar{4}2c$ [34]	$3A_1 \oplus 5A_2 \oplus 5B_1 \oplus 7B_2 \oplus 14E$	Raman	$3A_1 \oplus 5B_1 \oplus 6B_2 \oplus 13E$
			IR	$6B_2 \oplus 13E$
			Acoustic	$B_2 \oplus E$
			Silent	$5A_2$
—	$P\bar{4}2_1^a$	$4A_1 \oplus 3A_2 \oplus 5B_1 \oplus 6B_2 \oplus 12E$	Raman	$4A_1 \oplus 5B_1 \oplus 5B_2 \oplus 11E$
			IR	$5B_2 \oplus 11E$
			Acoustic	$B_2 \oplus E$
			Silent	$3A_2$
—	$P\bar{4}$ [36]	$4A_1 \oplus 6B_1 \oplus 7E$	Raman	$3A_1 \oplus 6B_1 \oplus 6E$
			IR	$6B_1 \oplus 6E$
			Acoustic	$B_1 \oplus E$

<sup>a</sup> This work.

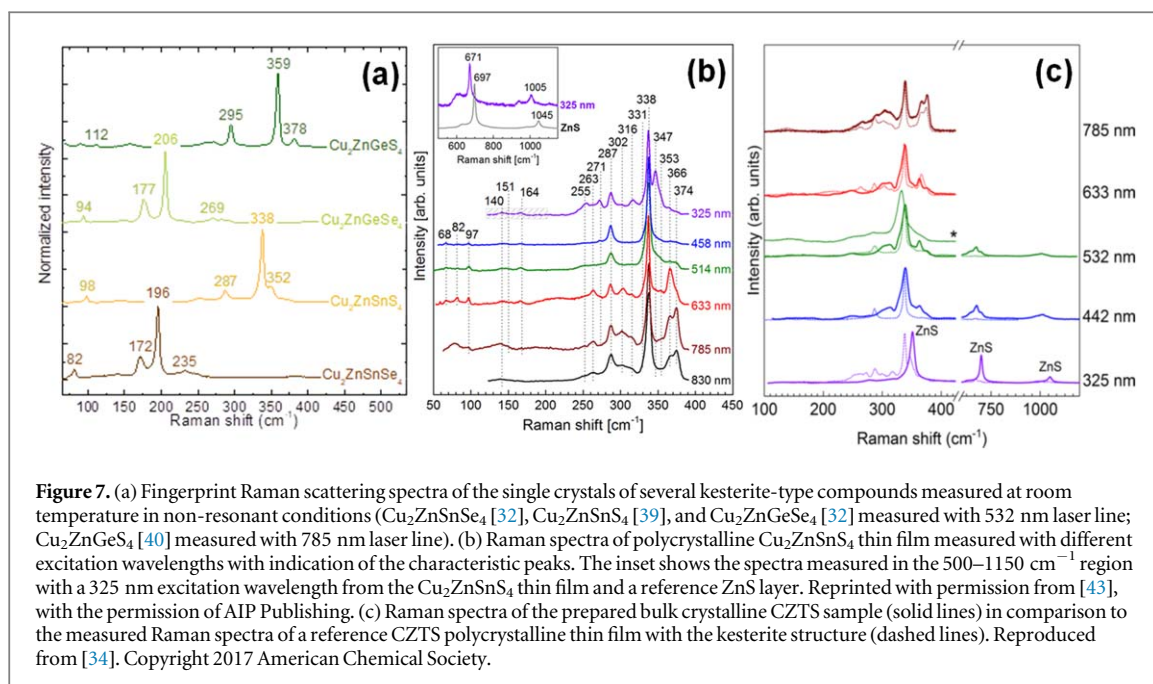
photons can lead to significant changes in the intensity of different peaks. This is mostly noticeable under the resonant Raman conditions, which are specified by the selection of the excitation wavelength coupled with the optical transitions in semiconductor compounds [22]. Such conditions lead to a significant increase in the probability of inelastic scattering, and as result, increase in the intensity of Raman peaks. Due to the specific selection rules of the vibrational spectroscopy [22] and possible different behavior of the modes in resonant conditions, the increase in the intensity of peaks is not equivalent, resulting in considerably different Raman spectra in resonant and off-resonant conditions [28]. Finally, after the proper selection of a suitable excitation power density, a fingerprint Raman spectra of the specific compound at the specific excitation wavelength can be obtained and used for the subsequent analysis of materials properties.

## 5. Raman scattering spectra of kesterite-type compounds

Nowadays the term 'kesterite compounds' is uniting a wide family of the quaternary compounds with the chemical formula  $A_2^I B^I C^I V X_4$ , where  $A^I = \text{Cu and Ag}$ ,  $B^I = \text{Mg, Ca, Cr, Mn, Fe, Co, Ni, Zn, Sr, Cd, Ba, and Hg}$ ,  $C^I V = \text{Si, Ge, and Sn}$ ,  $X = \text{S, Se, and Te}$  [29, 30]. Although these compounds belong to different crystal structure types, have different optical and electrical properties, and their Raman spectra are different, most of them were used or proposed as possible absorbers for thin film solar cells as pure compounds or as solid solutions, and similarities can be found through the entire family. This prompts us to cover in the present review not only the compounds with a strict kesterite-type structure, but to extend it to the all of mentioned compounds crystallizing in structures based on tetragonal Bravais lattices (i.e. the tetragonal primitive Bravais lattice and the tetragonal body centered Bravais lattice). Note that quaternary compounds from the mentioned family, which have different crystal structures, like orthorhombic, monoclinic, and cubic, have also been obtained by different researchers, but their analysis is outside of the scope of the present review.

### 5.1. Fingerprint Raman spectra

The main focus of researchers dealing with quaternary compounds so far has been devoted to those crystalized in a crystal structure based on tetragonal Bravais lattices. According to the type of crystal structure they can be divided into kesterite (space group  $I\bar{4}$ ), stannite (space group  $I\bar{4}2m$ ), primitive-mixed Cu-Au (PMCA, space



group  $P\bar{4}2m$ ), disordered kesterite (space group  $I\bar{4}2m$ ), and other nameless types of structures (space groups  $P\bar{4}2c$ ,  $P\bar{4}2_1$ , and  $P\bar{4}$ ) [31]. All these types of structures are differentiated by the position of Cu and Zn cations and have different irreducible representations. These are presented in table 2 together with the mode classification.

In the case of kesterite-type compounds their vibrational properties have been analyzed in single crystals, providing information not only about the frequency of most of the Raman modes, but also about the symmetry assignments of the modes [32, 37, 38–40]. The latter was obtained either by analysis of the angular dependence of the intensity of the Raman peaks measured with different laser polarization configurations [32, 38–40], or by analyzing the spectra from different crystal planes [37], which allows assigning the modes symmetry based on the selection rules and defining the type of structure. Analysis of the single crystal samples combined with the low temperature measurements allowed obtaining precise fingerprint Raman spectra [41]. However, the room temperature measurements are more common and we will discuss further the spectra obtained in these conditions.

Raman spectra of some kesterite-type compounds are presented in figure 7(a) with the indication of the position of the most intense characteristic Raman peaks. Here all the spectra were measured in non-resonant conditions and significant similarities in the spectral shapes can be observed. The difference in the spectra is due to the change in the types of cations, leading to the change in the atomic radius, interatomic bond length, and the force constants. This will directly influence the energy of the phonons, which will lead to a shift of Raman peaks while maintaining the overall spectrum pattern. Taking this into account, a typical Raman spectrum of any kesterite-type quaternary compound can be predicted [42]. On the other hand, using excitation wavelengths close to the resonant conditions can have a significant effect on the fingerprint of Raman spectra. This has been shown in studies where multiwavelength excitation conditions were used, and a comparison of spectra measured under different excitation energies in the same sample were presented [43–45]. As an example, the Raman spectra of CZTS thin films measured with six different wavelengths are presented in figure 7(b) [43]. The authors of [43] explained in detail the differences found in the spectra of CZTS kesterite measured in resonant and non-resonant conditions, and showed that resonance conditions can be reached not only in the case of coupling of the fundamental band gap with the laser energy (case of 830 nm  $\sim 1.49$  eV), but also in conditions when a high energy interband optical transitions are correlated with the excitation energy (case of 325 nm  $\sim 3.81$  eV) [43].

A pure stannite-type structure was found only in the case of quaternaries with certain compositions, such as  $\text{Cu}_2\text{FeSnS}_4$  [46] and  $\text{Cu}_2\text{CdSn}(\text{S},\text{Se})_4$  [47, 48]. Unfortunately, there are not many reports on the Raman spectra of quaternary compounds with a tetragonal lattice and other than kesterite-type structure, which is mostly due to difficulties in obtaining a pure phase. Raman spectra of a mixture of three structural polymorphs with the space groups  $I\bar{4}$ ,  $P\bar{4}2m$  and  $P\bar{4}2c$  were presented in [34] (see figure 7(c)). Here the authors observed new Raman peaks in the spectra of a bulk CZTS sample, and by comparing the data with the first principle calculations assigned all peaks to different structural polymorphs [34]. Details on the position of intense Raman peaks from

**Table 3.** Main Raman peaks of quaternary compounds crystallized in tetragonal Bravais lattices.

Compound	Solid state	Excitation (nm)	Raman shift <sup>a</sup> (cm <sup>-1</sup> )	References
Kesterite-type structure, space group $I\bar{4}$				
Cu <sub>2</sub> ZnSnS <sub>4</sub>	Single crystal	514.5	285, <b>334</b> , 352	[37]
	Single crystal	532	98, 287, <b>338</b> , 352	[39]
	Single crystal	785 <sup>b</sup>	287, 320, <b>338</b> , 366, 374	[39]
	Thin film	MW <sup>c</sup>	287, 302, <b>338</b> , 347, 366, 374	[43]
	Powder	532	288, <b>338</b> , 368	[47]
Cu <sub>2</sub> ZnGeS <sub>4</sub>	Polycrystal	532	98, 288, <b>338</b> , 347, 355, 365	[49]
	Single crystal	785	295, <b>359</b> , 378	[40]
Cu <sub>2</sub> ZnSnSe <sub>4</sub>	Single crystal	514.5 <sup>b</sup>	295, 317, <b>359</b> , 400	[40]
	Single crystal	532	82, 170, 174, <b>196</b> , 231	[32]
Cu <sub>2</sub> ZnGeSe <sub>4</sub>	Single crystal	532	79, 172, <b>196</b> , 230	[38]
	Single crystal	532	94, 176, 180, <b>206</b> , 269	[32]
Cu <sub>2</sub> MnSnS <sub>4</sub>	Thin film	532	277, <b>319</b>	[50]
Stannite-type structure, space group $I\bar{4}2m$				
Cu <sub>2</sub> MnSnS <sub>4</sub>	Powder	514.5	243, 283, <b>327</b> , 341	[33]
	Powder	514.5	92, 285, <b>327</b> , 348	[42]
Cu <sub>2</sub> FeSnS <sub>4</sub>	Powder	514.5	286, <b>318</b> , 350	[33]
	Powder	514.5	285, <b>318</b> , 352	[46]
Cu <sub>2</sub> ZnSnS <sub>4</sub>	Powder	514.5	285, <b>338</b> , 362	[33]
Cu <sub>2</sub> CdSnS <sub>4</sub>	Powder	514.5	279, <b>329</b> , 356	[33]
	Powder	532	282, <b>332</b> , 351	[47]
Cu <sub>2</sub> HgSnS <sub>4</sub>	Powder	514.5	283, <b>318</b>	[33]
Cu <sub>2</sub> FeGeS <sub>4</sub>	Powder	514.5	291, <b>341</b> , 377	[33]
	Powder	514.5	109, 294, <b>342</b> , 378	[42]
Cu <sub>2</sub> CoSiS <sub>4</sub>	Powder	514.5	300, <b>383</b>	[42]
Cu <sub>2</sub> MnSnSe <sub>4</sub>	Powder	514.5	115, 167, <b>188</b> , 231	[42]
Cu <sub>2</sub> FeSnSe <sub>4</sub>	Powder	514.5	105, 157, <b>175</b> , 220	[42]
Cu <sub>2</sub> CdSnSe <sub>4</sub>	Powder	514.5	116, 172, <b>192</b> , 228	[42]
	Powder	488	115, 172, <b>192</b> , 228	[48]
PMCA-type structure, space group $P\bar{4}2m$				
Cu <sub>2</sub> ZnSnS <sub>4</sub>	— <sup>d</sup>	—	304, <b>340</b>	[34]
Disordered kesterite-type structure, space group $I\bar{4}2m$				
Cu <sub>2</sub> ZnSnS <sub>4</sub>	Polycrystal	514.5	285, <b>331</b> , 350	[6]
Cu <sub>2</sub> ZnSiTe <sub>4</sub>	Polycrystal	785 <sup>b</sup>	81, 134, <b>151</b>	[35]
Space group $P\bar{4}2c$				
Cu <sub>2</sub> ZnSnS <sub>4</sub>	— <sup>d</sup>	—	289, <b>334</b> , 361	[34]
Space group $P\bar{4}$				
Cu <sub>2</sub> FeSnS <sub>4</sub>	Powder	514.5	218, 284, <b>321</b> , 400	[36]

<sup>a</sup> Only intense Raman peaks were selected. The most intense peaks are highlighted in bold.

<sup>b</sup> Resonant excitation wavelength.

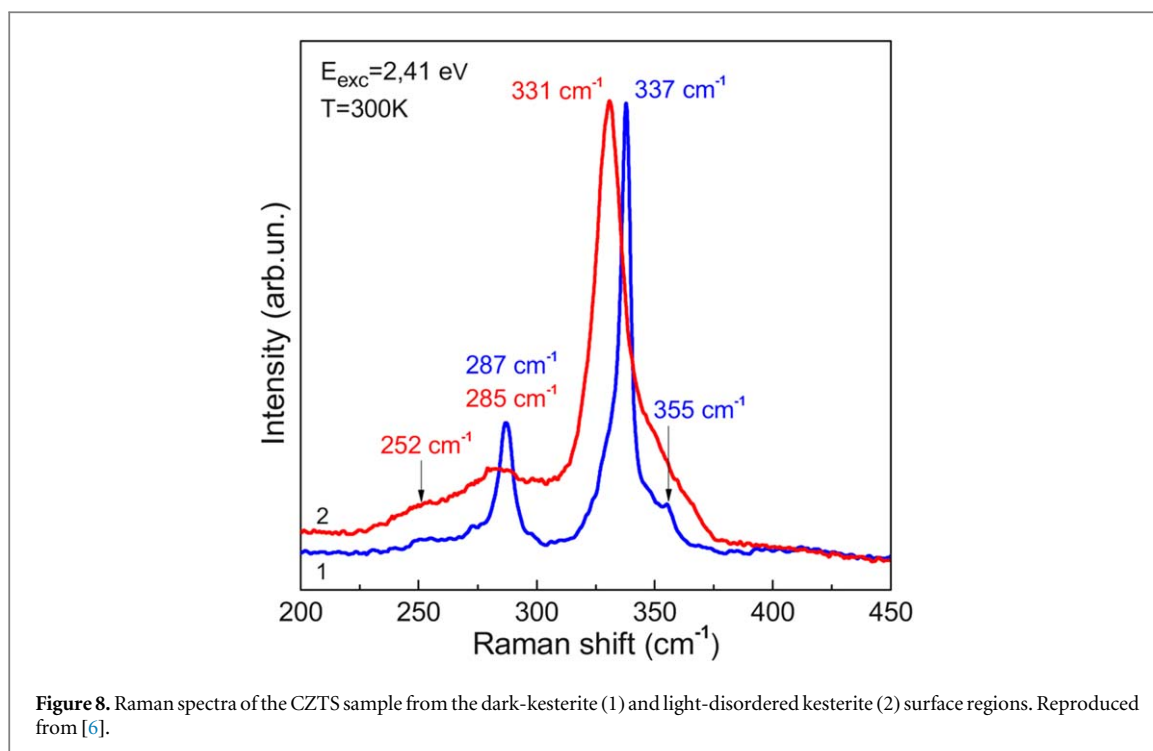
<sup>c</sup> Multiwavelength excitation. Here all intense peaks in the spectra measured under different excitation wavelength are indicated.

<sup>d</sup> Theoretically calculated data. No experimental spectra of pure phase were measured.

the spectra of various quaternary compounds with different crystal structures measured under different excitation wavelengths are shown in table 3.

Besides numerous experimental investigations of the vibrational properties in kesterite and stannite-type compounds, first principle calculations based on the density-functional theory have been conducted, enabling the determination of the phonon frequencies and eigenvectors in these materials [51–54]. Different approaches and calculation tools have been used to obtain the phonon density of states and make an in-depth comparison of the vibrational properties of different types of quaternary compound structures. In recent years, significant interest in the cation substitution in kesterite-type compounds, such as Cu<sub>2</sub>ZnGeS<sub>4</sub> [40, 41] and





$\text{Cu}_2\text{Zn}(\text{Sn}_{1-x}\text{Ge}_x)\text{S}_4$  [55] solid solutions, resulted in more detailed analysis of their vibrational spectra. In general, combined experimental and theoretical studies enable a much more detailed assignment of the experimentally observed Raman peaks to the vibrations of the specific atoms. This also allows for a better understanding of the nature of the changes found in Raman spectra which are measured on different samples.

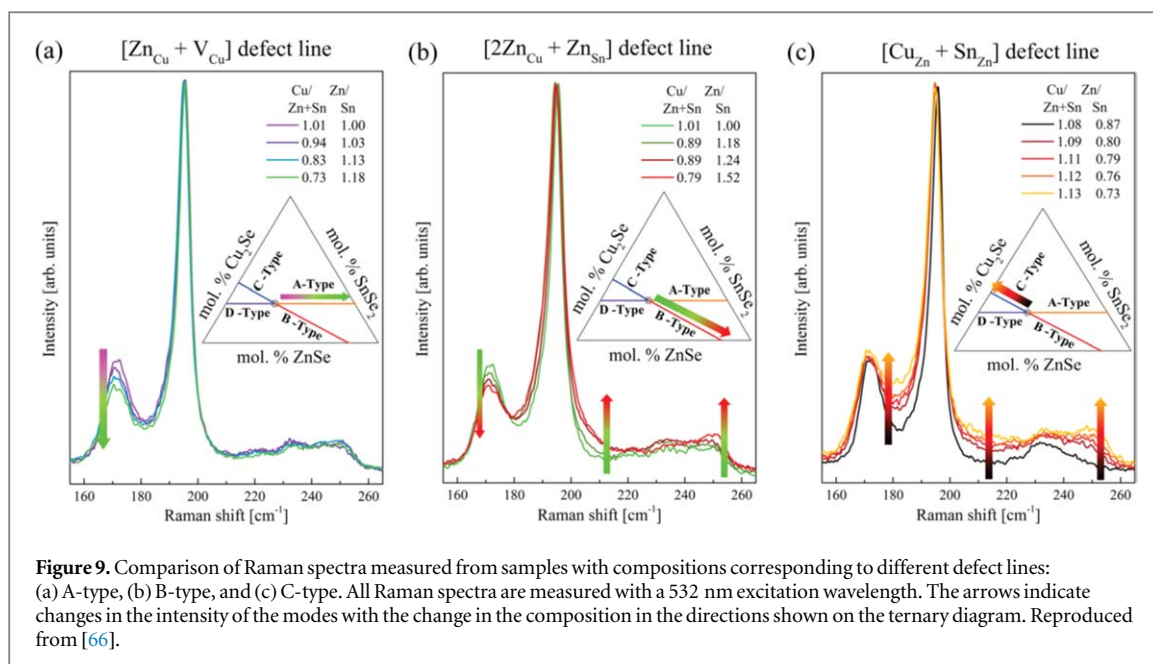
## 5.2. Influence of the quality of the crystal on the Raman spectra

In terms of the present review, the quality of the crystal of a material is defined as any kind of deviation in the symmetry of the crystal. This includes point defects (vacancies, anti-site defects, interstitial impurities, etc.), and one- and two-dimensional defects (dislocations, grain boundaries (GBs), etc.) [56]. The effect of the low density of defects in the Raman spectra is evidenced in the symmetrical peak broadening, which is related to the decrease in the phonon lifetime. The increase in the defect density leads to appearance of the peak shift together with asymmetrical broadening, which is caused by the activation of the phonon states outside of the zone-center  $\Gamma$ -point and a decrease in the phonon correlation length [57]. A further increase in the concentration of the defect leads to the appearance of Raman peaks with a Gaussian shape, in contrast to the Lorentzian shape of the peaks for the materials with good crystal quality. The Gaussian shaped Raman peaks indicate a certain random distribution of the bond length with a preferential value correlated to the position of the maximum intensity of the Raman peak. Typically Gaussian-like shaped Raman peaks are common in nanometric materials [58–60].

The phonon confinement model proposed by Nemanich *et al* [61] was applied by Dimitrievska *et al* [57] to the thin films of CZTS with different annealing times, resulting in an estimation of the phonon correlation lengths. The low frequency asymmetry of both A modes has been interpreted in terms of phonon confinement effects, while the observed peak shifts were found to result from a balance between the phonon confinement effects and lattice contraction due to the compressive strain effect [57].

The phonon confinement effect mentioned above is related to the random distribution of the defects, while together with this, a preferential defect position was detected in the kesterite-type compounds. Several reports have shown that there is an equal probability of the Cu and Zn cations to occupy  $2c$  and  $2d$  Wyckoff positions in certain growth conditions, leading to the appearance of the Cu-Zn disorder. An extreme case of this has led to the observation of a new disordered kesterite-type structure [35, 62]. The equal probability of Cu and Zn atoms of occupying two positions increases the symmetry of the structure, compared to standard ordered kesterites, and changes the space group to  $I\bar{4}2m$  [35, 62]. The first assumption of the possible influence of disorder to Raman spectra of kesterite compounds was made by Grossberg *et al* [49] based on evidence in the appearance of a shoulder close to the most intense peak. Later Valakh *et al* evaluated this assumption in [6, 63, 64] and a spectrum presented in figure 8 from [6] can be considered as a fingerprint Raman spectra of disordered kesterite-type structure. In this spectrum, a dominant peak appears at lower wavenumbers ( $331\text{ cm}^{-1}$ ) than in ordered





kesterite ( $338 \text{ cm}^{-1}$ ), and an impressive broadening is evident, which is related to the decrease of the phonons lifetime due to Cu-Zn disorder.

A less pronounced influence of the specific defects on the Raman spectra was analyzed in terms of different non-stoichiometry types of kesterites [65–68], which assumes the formation of various defect complexes [17]. Here the changes in the relative peak intensity of CZTSe were correlated to changes in the concentration of different defect complexes [65–68] (see figure 9), although only a qualitative analysis of the defect formation from Raman spectra can be performed using the proposed methodology.

A methodology based on the analysis of the relative intensity of specific Raman peaks has also been proposed [69] for the estimation of disorder value in kesterites, and was later quantified to calculate the disorder parameter [70]. However, the authors cautioned that the proposed quantification should not be used to determine disordered parameter values for samples which deviate substantially in composition or preparation method from those used by them [70].

### 5.3. Solid solutions of kesterites in Raman spectroscopy

Until now the highest efficiency of the solar cells based on kesterite-type compounds was achieved using solid solutions, with anion, cation, or both anion-cation substitutions. The theory of the Raman modes behavior in solid solutions is based on the modified random-element-isodisplacement model and has been proposed for the binary compounds [71]. In simple terms, the model correlates the molar masses of substituted elements with their reduced mass [71], which allows predicting for each peak the one or two-mode behavior in the solid solutions of most of binary compounds. Unfortunately, this becomes much more complex in the case of multinary compounds, and makes it rather difficult to predict the Raman peak behavior in the case of the substitution of one of the elements. In a more general way, the behavior of the Raman modes can be divided in three main types as depicted in the top panels in figure 10. The one-mode behavior is related to the random distribution of the substituted atoms in solid solutions and is characterized by the shift of the Raman peak in between two positions of the edge points of solid solutions. The two-mode behavior can be caused by formation of the separate clusters or supercells of substituted atoms leading to the appearance of two modes related to the vibrations of these clusters. The frequencies of the two modes tend to approach each other, but only one of them is seen in the edge members of the solid solution. The appearance of a new peak, or three-mode behavior, is a more complex version of the two-mode behavior, where together with the clusters of substituted atoms, a cluster or supercell of mixed atoms is also formed, the common vibration of which leads to the rise of a new peak in between the two peaks of the edge compositions.

In the solid solutions of kesterite-type compounds all types of Raman peaks behaviors were found. The one-mode behavior was observed for the most intense peak in the majority of kesterite-based solid solutions with the substitution of cations (e.g.  $\text{Cu}_2(\text{Mn}_x\text{Zn}_{1-x})\text{SnS}_4$  [50],  $\text{Cu}_2\text{Zn}(\text{Sn}_{1-x}\text{Ge}_x)\text{Se}_4$  [45, 72]). However, this was not a case for the less intense peaks as shown in [45], for which a two-mode behavior was observed (see panel (a) in figure 10). This can be explained by assignment of different modes to the vibrations of different atoms. The most intense peaks in the kesterite compounds were assigned to the fully symmetric A symmetry modes [32, 39, 40], which are related to

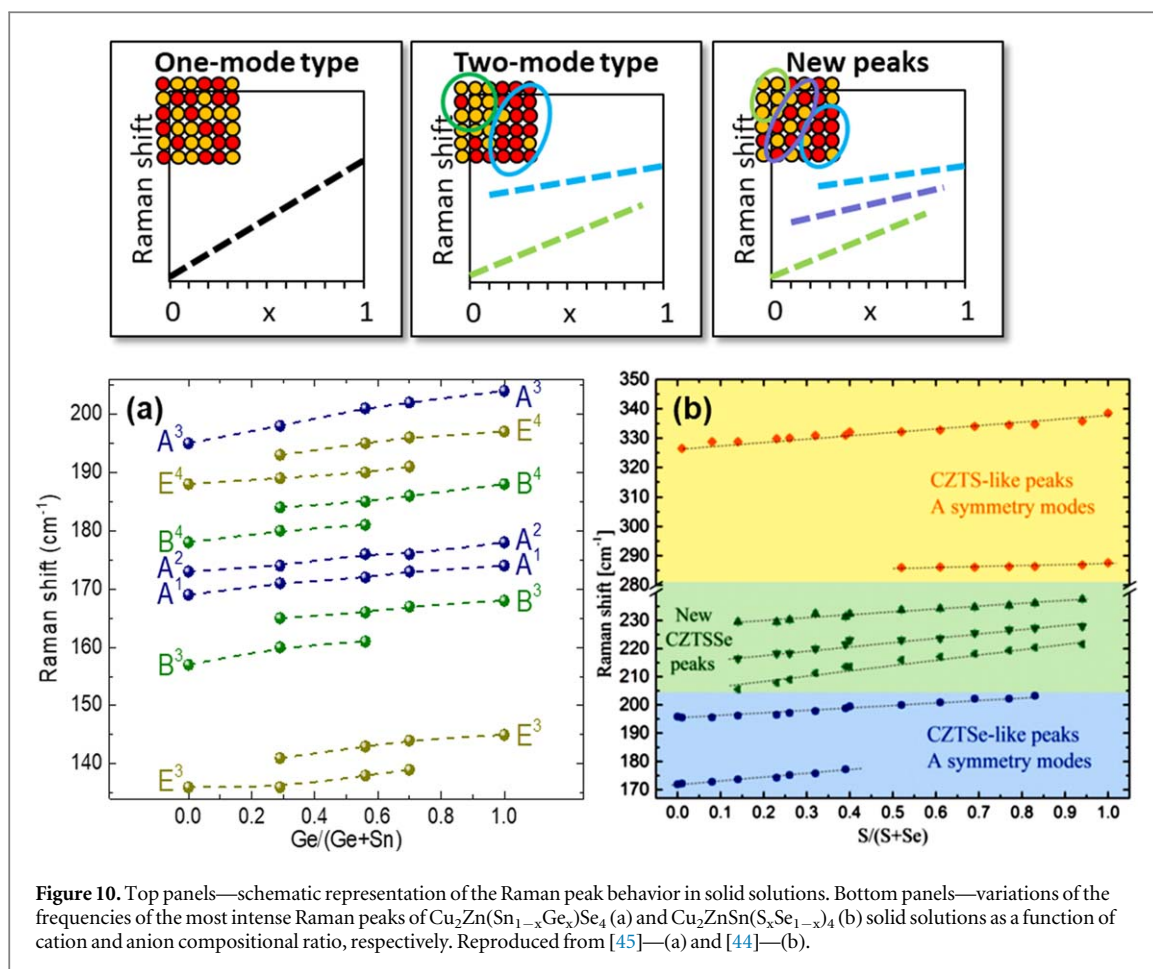


**Figure 10.** Top panels—schematic representation of the Raman peak behavior in solid solutions. Bottom panels—variations of the frequencies of the most intense Raman peaks of  $\text{Cu}_2\text{Zn}(\text{Sn}_{1-x}\text{Ge}_x)\text{Se}_4$  (a) and  $\text{Cu}_2\text{ZnSn}(\text{S}_x\text{Se}_{1-x})_4$  (b) solid solutions as a function of cation and anion compositional ratio, respectively. Reproduced from [45]—(a) and [44]—(b).

the pure anion vibrations [40, 51–54], while the less intense peaks were assigned to the polar B or E symmetry modes [32, 39, 40], which include the vibration of both cations and anions [40, 51–54]. Taking this into account, the one-mode behavior is expected with the cation substitution in kesterite solid solutions, while the shift of the A symmetry peaks is related to the change in the distance between anions. The less intense peaks, being directly related to the cation vibrations, then exhibit the two-mode behavior. Nevertheless, this logic was broken for the  $\text{Cu}_2\text{Zn}(\text{Sn}_{1-x}\text{Ge}_x)\text{S}_4$  solid solution, where the two-mode behavior was also observed for the A symmetry modes [45, 73]. The assumption about the difference in mode behaviors between S and Se containing solid solutions with Sn-Ge substitution was made in [45] and was based on a substantial difference in the masses of S and Se anions in comparison to Sn and Ge cations.

At first, the two-mode behavior of the most intense Raman peak was also proposed in the case of  $\text{Cu}_2\text{ZnSn}(\text{S}_x\text{Se}_{1-x})_4$  solid solutions [74]. However further, more detailed analysis of the Raman peaks allowed detecting the appearance of new peaks in the Raman spectra of this solid solution [44, 75]. The authors performed a detailed analysis of the Raman spectra measured with three different laser lines in numerous thin film polycrystalline samples, which allowed them to show the unambiguous presence of new peaks in the spectra of solid solutions (see panel (b) in figure 4 [44]).

Changes observed in the Raman spectra of kesterite solid solutions were used for the quantification of the ratio of concentrations of the substituted atoms. Until now, this has been performed for  $\text{Cu}_2\text{Zn}(\text{Sn}_{1-x}\text{Ge}_x)\text{Se}_4$  [45],  $\text{Cu}_2\text{Zn}(\text{Sn}_{1-x}\text{Ge}_x)\text{S}_4$  [45], and  $\text{Cu}_2\text{ZnSn}(\text{S}_x\text{Se}_{1-x})_4$  [75] solid solutions, and allows estimating the ratio of substituted elements within an error not exceeding 10%.

#### 5.4. Detection of secondary phases in kesterites

There is a higher probability of the formation of secondary phases in kesterite compounds during the synthesis process, due to its multinary composition. One of the first applications of Raman spectroscopy for the detection of secondary phases in kesterites was proposed by Fernandes *et al* [76, 77], and then developed by the authors by collecting the spectra of most of the possible secondary phases in [78]. A more detailed study on the detection of secondary phases yielded the necessity of multiwavelength excitation for the fine detection of secondary phases. This was first proposed by Fontané *et al* for the ZnS secondary phase in CZTS

**Table 4.** Secondary phases observed in kesterite-type quaternary compounds, their most intense Raman peaks and the optimum excitation wavelength for their detection.

Secondary phase	Raman shift ( $\text{cm}^{-1}$ )	$\lambda_{\text{exc}}$ <sup>a</sup> (nm)	References <sup>b</sup>
$\text{Cu}_2\text{ZnSnS}_4$			
ZnS	350	325	[79, 80]
$\text{Cu}_2\text{SnS}_3$ <sup>c</sup>	354, 292 <sup>d</sup>	532	[80]
$\text{Cu}_3\text{SnS}_4$	317	532	[79]
$\text{Cu}_x\text{S}$	475	532	[76]
$\text{SnS}_2$	314	532	[80]
$\text{Sn}_2\text{S}_3$	308	532	[76]
$\text{SnS}$ <sup>c</sup>	220, 192, 163	785	[80]
$\text{MoS}_2$ <sup>e</sup>	408	532	[79, 80]
$\text{Cu}_2\text{ZnSnSe}_4$			
ZnSe	250	442	[83]
$\text{Cu}_2\text{SnSe}_3$	180	785	[85]
$\text{Cu}_x\text{Se}$	260	532	[77]
$\text{SnSe}_2$	314	785	[73]
$\text{SnSe}$	151, 130	785	[73]
$\text{MoSe}_2$ <sup>e</sup>	240	532	[86]

<sup>a</sup> Excitation wavelengths in the vicinity to the indicated ones also can be used for optimal phase detection, like 457.9 nm instead of 442 nm, or 514.5 nm instead of 532 nm.

<sup>b</sup> Some of the references where the specific secondary phase was detected in quaternary kesterites.

<sup>c</sup> Only stable monoclinic and orthorhombic polymorphs of  $\text{Cu}_2\text{SnS}_3$  and  $\text{SnS}$ , respectively, were detected until now.

<sup>d</sup> In the case of the indication of multiple peaks all of them have comparable intensities.

<sup>e</sup> Formation of  $\text{MoS}_2$  and  $\text{MoSe}_2$  have been observed on the interface of the CZTS and CZTSe thin film, respectively, with the back contact after the lift-off, through the substrate with the transparent back contacts or in thin films with poor compactness of the grains.

\*Note that specific secondary phases of kesterite compounds containing Ge have not been observed as of yet.

kesterites by using a 325 nm excitation wavelength [79]. This idea was further developed and was shown that extremely low quantities of ZnS secondary phases can be detected under UV excitation (325 nm), while the more conventional green excitation (514.5 or 532 nm) did not allow for clear detection even of the major ZnS phase in minor CZTS [80, 81]. On the other hand, the green excitation was found to be sensitive enough for detection of the  $\text{Cu}_2\text{SnS}_3$  secondary phase [80], as well as other binary phases, such as  $\text{Cu}_x\text{S}$  and  $\text{SnS}_2$ . This difference in the detection of the secondary phases is strongly related to the so-called Raman efficiency, which is dependent on the used excitation wavelength. In this framework, the high band gap ZnS being close to resonant conditions under UV excitation [82] has a much stronger Raman signal than in the case of the green excitation wavelength, for which a small scattering of the light is expected. In contrast,  $\text{Cu}_2\text{SnS}_3$  or binary  $\text{Cu}_x\text{S}$  secondary phases, with a band gap lower than the energy of a green laser, exhibit enough strong scattering of this light, making it possible to assess even a small amount of the phase.

In the case of the CZTSe compound special attention was paid to the detection of a ZnSe secondary phase, which has a band gap close to the blue region of the spectra [83]. Following this, the blue excitation wavelengths (442 or 457.9 nm) were proposed as optimum for the evaluation of ZnSe secondary phase in CZTSe [83]. The other secondary phases, like  $\text{Cu}_2\text{SnSe}_3$  and  $\text{SnSe}$ , were found to be detectable under NIR excitation (785 nm) [83, 84]. Finally, based on previously published studies and experimental experience the secondary phases of quaternary kesterite-type compounds with their most intense Raman peaks and most appropriate excitation wavelengths are listed in the table 4.

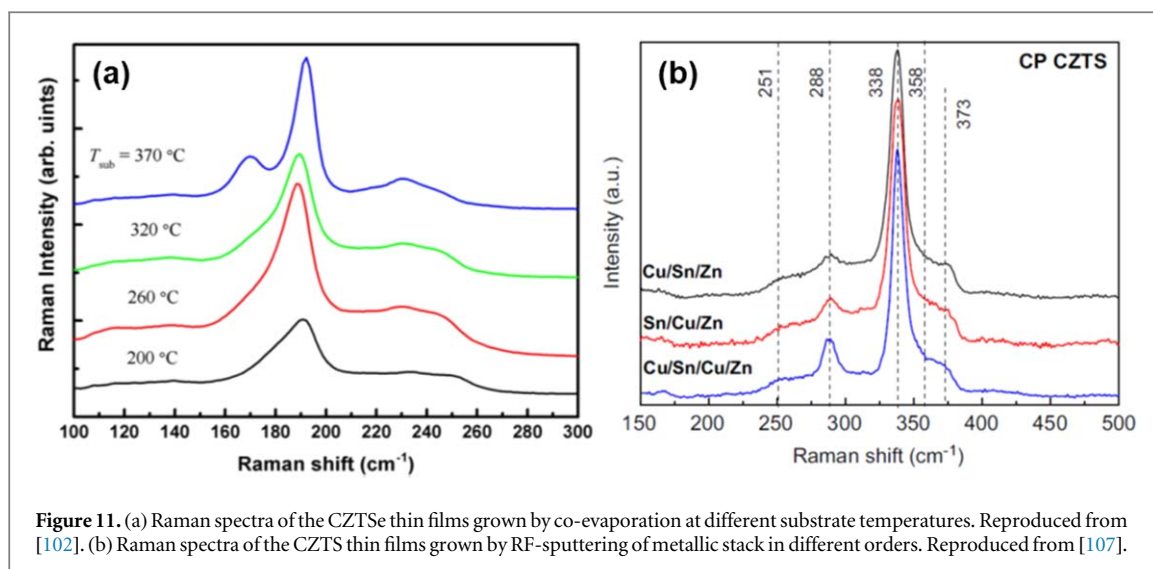


**Figure 11.** (a) Raman spectra of the CZTSe thin films grown by co-evaporation at different substrate temperatures. Reproduced from [102]. (b) Raman spectra of the CZTS thin films grown by RF-sputtering of metallic stack in different orders. Reproduced from [107].

## 6. Assessment of kesterite properties and solar cell performance by Raman spectroscopy

Recently, Raman spectroscopy has become a widely used technique for the confirmation of quaternary phase formation, as in the case of its application in solar cell devices [84–92], as well as for further fundamental material analysis [93–100]. The increased popularity of Raman spectroscopy for the assessment of kesterite-type quaternary compounds, as well as of other inorganic materials, is mostly due to the strong increase in the usability and versatility of Raman systems and low qualification requirements for the general spectra analysis. The latter includes the possibility of fast and non-destructive assessment of the required phase formation, crystalline quality, and secondary phase appearance. However, a more complex correlation of the Raman spectra with other properties of the obtained samples still requires a deep knowledge and understanding of this specific scattering process.

In the case of kesterite-type compounds a more detailed analysis was performed in previously described works about Raman polarization measurements on single crystals, assessment of the influence of defects and phonon confinement, and quantification of the ratio of elements in solid solutions. The possibilities of Raman spectroscopy were then used for a more complex understanding of the properties of kesterites and formation mechanisms. For instance, Raman spectroscopy allowed revealing the intermediate formation steps and the optimal formation temperatures of kesterite compounds [83, 85, 101–106]. Here the authors showed how the kesterites are formed by starting from different precursors [101, 102, 104], or the influence of Ge on the formation steps [85], or how the deposition temperature conditions or thermal treatment could improve the quality of the kesterite phase [83, 102, 106] (e.g. see figure 11(a)). In parallel the optimum stack order for sputtered thin films was also analyzed comparing the Raman spectra of different samples [107–109], which allowed identification of the order leading to the highest crystal quality (see figure 11(b)) or preventing the formation of secondary phases, as shown in [109].

The combination of Raman spectroscopy with other characterization techniques, like sputtering the sample with an Ar<sup>+</sup> beam from a Auger electron spectroscopy system [79] or mechanical polishing by using a dimple grinder [110], resulted in the in-depth analysis of the thin films' homogeneity. Measurements of Raman spectra at different depths after the mechanical polishing (see the schematic of the performed measurements in figure 12) allowed the authors to evaluate the secondary phase distributions within the thin film and the phase formation at the back contact interface [110].

Valuable results about the kesterite thin film surfaces were obtained by using micro [81, 110–113] and macro [114, 115] Raman mappings (e.g. see figure 13). This allowed understanding the distribution of secondary phases on the sample surface or in-depth, to propose the best cations ratio, and to detect the changes in the materials after the specific local post-deposition treatment [113–115].

Finally, the correlation of the results from Raman spectroscopy with the optoelectronic properties of kesterite-based solar cells allowed analyzing the factors limiting the performance of the devices [68, 92, 110, 116]. The assessment of the defects by means of Raman spectroscopy resulted in experimental evidence of the effect of the Cu-substitutional defects on the optoelectronic properties, especially on open circuit voltage [116]. Along this line, interesting results have also been obtained using Raman non-band gap resonant conditions with

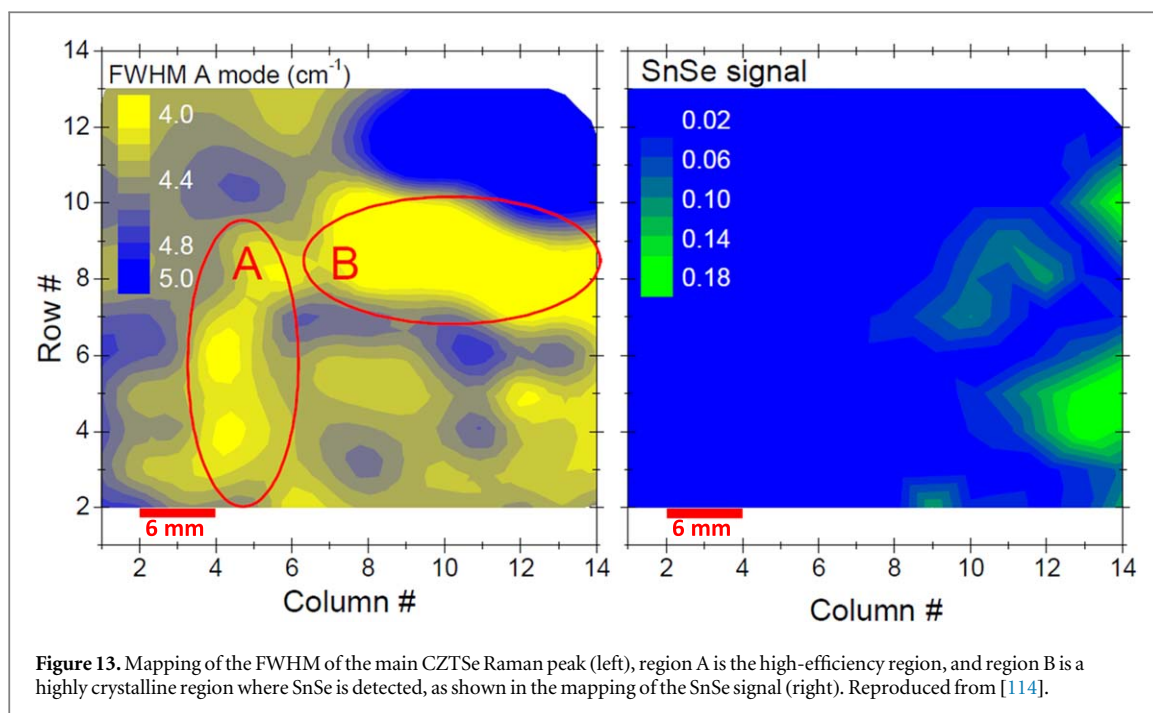




325 nm excitation for the assessment of CZTS thin films [67, 106]. Under this specific excitation wavelength the authors showed a clear modification of the relative intensity of different Raman peaks with crystallization time. This has been attributed to changes in the  $V_{Cu}$  and  $Zn_{Sn}$  point defect concentrations in the absorber surface (<20 nm), which have a strong impact on the final optoelectronic properties of solar cell devices [106]. On the other hand, the correlation of Raman spectra changes with the optoelectronic properties also yielded an understanding of the effect of small Cu cations substitution by Mg in CZTSe-based solar cells [92].

## 7. Conclusion

In conclusion, Raman spectroscopy has become an impressively powerful tool for the assessment of kesterite-type compounds, either for a low or high level of analysis. The former includes the possibility of obtaining fast qualitative results on the quaternary and secondary phase formation, crystal quality, and crystal structure of the main phase, as well as information on the composition of the solid solution of kesterites. A deeper, high level analysis requires more detailed understanding of this scattering mechanism. This would allow analysis of the Raman spectra at different production stages, yielding information about the formation mechanism of the compounds and the optimum deposition conditions and post-deposition treatment. An in-depth analysis can provide information on the defects occurring in the kesterite-type compounds, while the micro and macro



mappings yield information on the homogeneity of all the mentioned parameters in the surface or in-depth profile of the obtained layer.

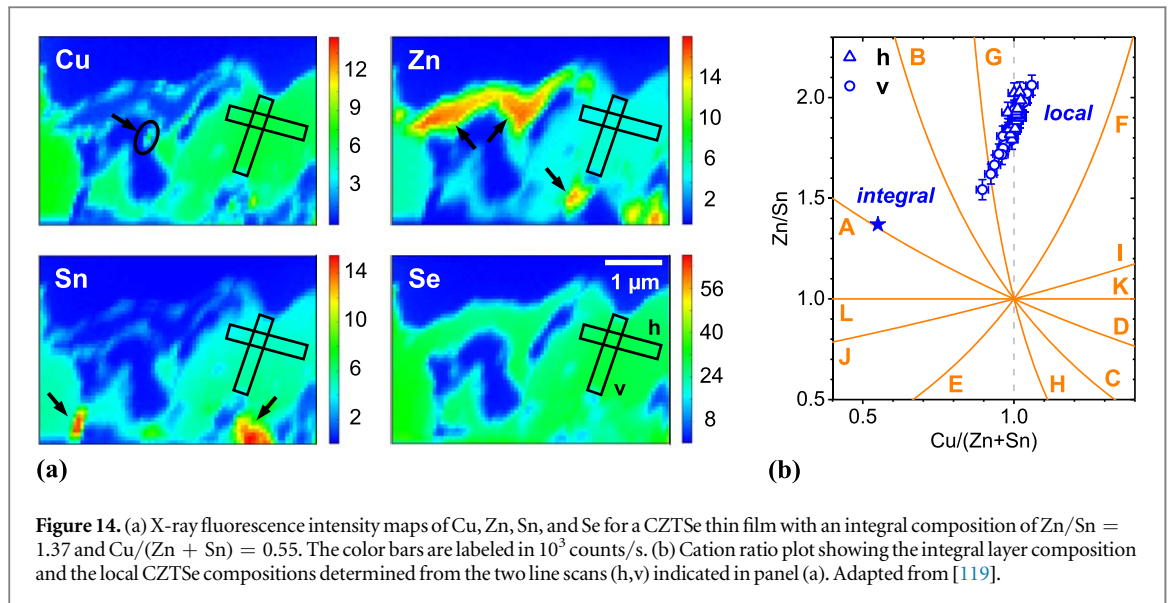
### C. Homogeneity of kesterites studied using synchrotron-based techniques

#### 8. Introduction

Kesterite materials often contain the segregation of related binary and ternary phases, including ZnSe,  $\text{Cu}_x\text{Se}$ ,  $\text{SnSe}_x$ , and  $\text{Cu}_2\text{SnSe}_3$  or the corresponding sulfides, as discussed already in section 5. Furthermore, it was clearly shown in section 2 that the kesterites themselves can tolerate significant deviations from the ideal stoichiometry, thus enabling pronounced compositional variations even for single-phase samples. Both features clearly affect the electrical and optical properties and may severely limit the solar cell performance. Therefore, secondary phases and compositional fluctuations need to be identified and quantified precisely in order to investigate their impact on the material properties and to find optimized preparation routes that avoid detrimental inhomogeneity. However, the analysis based on one technique alone can often be ambiguous, and hence, different complementary methods are required to obtain a comprehensive picture. Synchrotron-based techniques such as high-resolution x-ray fluorescence analysis and x-ray absorption spectroscopy present powerful methods to study the composition and phase content of a material. They provide both spatially resolved and integral information and beneficially complement other techniques such as x-ray and neutron diffraction, Raman spectroscopy, or electron microscopy.

#### 9. Compositional homogeneity on the nano- to micrometer scale

Compositional homogeneity on the nano- to micrometer scale can be investigated by preparing thin cross-section lamellas and applying high-resolution x-ray fluorescence spectroscopy with a synchrotron nanobeam (nanoXRF). In principle, the technique is similar to energy dispersive x-ray analysis (EDX) using a scanning or transmission electron microscope (SEM, TEM). While the spatial resolution is somewhat lower than for EDX, nanoXRF provides excellent compositional resolution such that subtle fluctuations in the bulk composition and even compositional variations at GBs and interfaces can be clearly resolved [117, 118]. To investigate an extreme case of non-stoichiometry, a CZTSe thin film with an integral layer composition of  $\text{Zn}/\text{Sn} = 1.37$  and  $\text{Cu}/(\text{Zn} + \text{Sn}) = 0.55$  was grown by two-stage selenization of a sputtered metallic Cu-Zn-Sn precursor [119]. A thin cross-section lamella of approximately 270 nm thickness was prepared from the sample using a focused ion



beam. The nanoXRF measurements were performed at station ID16B of the European Synchrotron - ESRF [120] with a beam spot size of approximately 50 nm and an x-ray energy of 29.34 keV. The latter enables the excitation of the fluorescence K lines of all elements of interest, including Sn. The lamella was moved stepwise through the beam and a full XRF spectrum was recorded at every spot.

Plotting the intensity of the different K lines as a function of the beam position yields the elemental distribution maps of Cu, Zn, Sn, and Se shown in figure 14(a) [119]. The Se exhibits a homogeneous intensity distribution except for some rather large voids within the layer. In contrast, strong intensity variations are apparent for Cu, Zn, and Sn, where the accumulation of one cation species spatially corresponds to a nearly complete absence of the other two cation species. The co-localization with Se indicates the formation of binary compounds, namely ZnSe, SnSe<sub>x</sub>, and even Cu<sub>x</sub>Se as marked by the black arrows in figure 14(a). Consequently, all three binary phases are present in the layer and coexist within an area of only a few micrometers in size [119]. Nano- to micrometer-sized secondary phases, in particular ZnSe segregations, were also observed by TEM-EDX and atom probe tomography (APT) for CZTSe thin films with an overall Zn-rich composition formed by selenization of co-evaporated Cu-Zn-Sn-Se precursors [121, 122] and for CZTSSe thin films prepared in a sequential solution-based process [123]. Secondary phase segregations are thus a common feature of non-stoichiometric kesterite thin films and may occur for a large range of integral layer compositions and growth techniques.

Apart from its direct impact on the device functionality, the presence of secondary phases further entails that the composition of the actual kesterite phase deviates from the integral layer composition and that the material may be characterized by structural and electronic defects different than expected. As shown in figure 14(b), the integral layer composition corresponds to the A-type material with Cu vacancies  $V_{Cu}$  and Zn<sub>Cu</sub> anti-sites. The local composition of the CZTSe domains was determined by fitting the individual XRF spectra and calculating the cation ratios from the atomic concentrations thus obtained [119]. The results for two line scans, one horizontally (h) and one vertically (v) as indicated in figure 14(a), are plotted in figure 14(b). Clearly, the local CZTSe compositions are markedly different from the integral layer composition and mostly correspond to a mixture of G- and F-type material with Zn<sub>Sn</sub> and Cu<sub>Sn</sub> anti-sites and Zn<sub>i</sub> and Cu<sub>i</sub> interstitials. While  $V_{Cu}$  and Zn<sub>Cu</sub> associated with A-type material form shallow acceptor and donor levels, the point defects associated with G- and F-type material are predicted to form deep donor and acceptor levels instead [13]. The integral layer composition may thus not be a reliable measure for anticipating the electronic properties of the actual kesterite material. Furthermore, figure 14(b) demonstrates a significant spread of the local CZTSe compositions on a submicrometer scale [119]. Variations of the cation ratios on a nano- to micrometer scale were also observed by TEM-EDX for solution-grown CZTS single crystals [124] and by APT for CZTSe thin films formed by selenization of co-evaporated Cu-Zn-Sn-Se precursors [121]. In conclusion, non-stoichiometric CZTSe and CZTS thin films frequently exhibit secondary phase segregations, a notable difference between integral layer composition and actual kesterite composition, and a significant variation of the local CZTSe or CZTS composition on a nano- to micrometer scale.



## 10. Identification and quantification of secondary phases

Secondary phases can further be identified and quantified using x-ray absorption spectroscopy. To this end, the x-ray absorption coefficient is measured as a function of the x-ray energy around the absorption edge of a particular element [125]. The so-called x-ray absorption near edge structure (XANES) depends on the chemical bonding of the absorbing atoms and on the symmetry of their structural environment. Sulfur anions in  $\text{Cu}_2\text{ZnSnS}_4$  are bound to two Cu, one Zn, and one Sn cation in a tetrahedral configuration. In contrast, S anions in ZnS are bound to four Zn cations in a tetrahedral configuration and S anions in  $\text{Cu}_x\text{S}$  or  $\text{SnS}_x$  are bound solely to Cu or Sn cations, respectively, mostly in a tetrahedral or octahedral configuration. Consequently, the XANES measured at the S K-edge is distinctly different for  $\text{Cu}_2\text{ZnSnS}_4$ , ZnS,  $\text{Cu}_x\text{S}$ , and  $\text{SnS}_x$  and can be used to determine the fraction of each phase in an unknown sample by linear combination analysis of the measured spectra [125].

Studies were performed for CZTS thin films with integral cation ratios of  $1.0 \leq \text{Zn/Sn} \leq 3.0$  and  $1.9 \leq \text{Cu/Sn} \leq 3.0$  deposited in a single-step co-evaporation process [126–128] and with integral cation ratios of  $0.8 \leq \text{Zn/Sn} \leq 1.6$  and  $1.7 \leq \text{Cu/Sn} \leq 1.8$  formed by sulfurization of evaporated metallic precursors [129]. For all co-evaporated thin films, the presence of ZnS segregations was observed in Zn-rich material [126–128]. Furthermore, Just *et al* report that the Zn/Sn ratio of the actual kesterite phase never exceeded 1 and that all excess Zn formed ZnS [127]. In contrast, Siah *et al* found that the kesterite phase remained significantly Zn-rich in addition to the presence of ZnS segregations [128]. Zn-rich, Cu-poor films prepared in the sequential process featured both ZnS and SnS secondary phases and their amount increased with increasing deviation from stoichiometry [129]. In contrast, co-evaporated thin films with  $\text{Cu/Sn} > 2$  contained  $\text{Cu}_x\text{S}$  segregations, which hosted all excess Cu such that the Cu/Sn ratio of the actual kesterite phase was equal to the stoichiometric value of 2 [127]. Depth-resolved studies applying XANES measurements with a varying angle of incidence revealed that ZnS formed preferably at the top and bottom of co-evaporated CZTS layers while  $\text{Cu}_x\text{S}$  segregations were only observed at the top surface [130]. Interestingly, a CZTS layer grown in a sequential process featured homogeneously distributed ZnS segregations [130], indicating that the presence and distribution of secondary phases depends on both the integral sample composition and the deposition process. The sensitivity of XANES to the presence of secondary phases was also used to exclude the occurrence of binary segregations and thus to confirm the single-phase nature of different CZTS thin films [131], nanocrystals [132], and powder [133].

Regarding selenide kesterites, the XANES features of the Se K-edge are less pronounced than those of the S K-edge due to a lower intrinsic and experimental energy resolution at the Se K-edge [127]. Therefore, the sensitivity for identifying secondary phases is somewhat reduced compared to sulfide kesterites. Nevertheless, the amount of ZnSe segregation was successfully quantified by Just *et al* for CZTSe thin films with integral Zn/Sn ratios between 1.0 and 4.0 prepared in a sequential solution-based process [127]. Similar to the results reported by the same authors for sulfides, all excess Zn in the CZTSe thin films was found to form ZnSe, and the Zn/Sn ratio of the actual kesterite phase never significantly exceeded 1.

## 11. Conclusions

Secondary phase segregations and pronounced compositional variations are typical features of non-stoichiometric kesterite materials. Their nature, quantity, and spatial distribution depend on the integral sample composition as well as the preparation conditions. The lack of compositional and structural homogeneity may severely alter the electrical and optical properties and therefore needs to be investigated on a macroscopic and microscopic scale. Synchrotron-based high-resolution x-ray fluorescence analysis and x-ray absorption spectroscopy provide powerful and unique contributions in addressing this challenge. As common to all synchrotron-based methods, the access is slower and less simple than for laboratory-based techniques like EDX, Raman spectroscopy, or XRD. However, the following advantages justify the use of nanoXRF and XANES as complementary techniques of analysis. (i) Although the spatial resolution of nanoXRF is lower than that of related electron microscopy methods (SEM-EDX, TEM-EDX, or wavelength dispersive x-ray analysis), it provides excellent compositional resolution. Furthermore, it enables the excitation of fluorescence K lines even for heavier elements such as Sn, which benefits the data analysis since it reduces the overlap of fluorescence lines from different elements. The same is possible for most TEM applications but it is usually more difficult for SEM setups. In contrast, detection of very light elements may be precluded with nanoXRF if the sample and detector are set up in air rather than in a vacuum chamber. (ii) Since the investigated length scale amounts to several micrometers, the whole solar cell layer stack including all interfaces and multiple grains can be analyzed in one single measurement different to TEM-EDX or APT. (iii) In comparison to Raman spectroscopy, nanoXRF allows the direct observation of the spatial distribution of the different elements, thus revealing the number, size, morphology, and localization of secondary phase

segregation. Moreover, compositional fluctuations or gradients can be studied with submicrometer spatial resolution. As for any technique with high spatial resolution, this is achieved by a trade-off with statistics and the results typically are of an exemplary nature. Therefore, additional methods such as XANES are required, which do not feature spatial resolution but provide integral properties characterizing a large sample volume. (iv) Using XANES, the integral secondary phase content of the material can not only be identified but also quantified with a sensitivity and accuracy down to a few percent [126, 127, 129], which is difficult to achieve with other techniques. (v) Based on the extremely local nature of the underlying physical processes, XANES does not require crystallinity and is sensitive even to nanometer-sized segregations. It can therefore provide information complementary to that obtained with diffraction or Raman spectroscopy. In conclusion, synchrotron-based techniques such as nanoXRF and XANES yield valuable contributions to the identification and quantification of secondary phases and compositional fluctuations in non-stoichiometric kesterite materials on the macroscopic, microscopic, and nanoscopic scale.

## D. Homogeneity of kesterites investigated by KPFM

### 12. Introduction to KPFM

#### 12.1. Nano-scale morphology and surface potential (SP)

Homogeneity of absorbers is a significantly important factor to acquire uniform operation of solar cells and modules. Kesterite, especially, is a complex material that is susceptible to defects and unexpected phases. Moreover, the various growth conditions of the precursors have significant impacts on the homogeneity of the absorbers. Electron beam microscopy and optical tools are adapted to investigate the nature of the inhomogeneities of the materials but they have drawbacks with super nano-scale length scale and little sensitivity of the surface. For instance, XRD and Raman scattering spectroscopy can be generally used to characterize the thin-film homogeneity. However, since CZTSe, ZnSe, and CTSe have a similar crystal structure, it would be difficult to distinguish each phase from the others by XRD. The penetration depth of a laser light can also decrease the surface sensitivity of the Raman scattering method. In addition, it is not clearly addressed how the spatial fluctuations of atomic elements, point defects, and microstructural imperfections are critical in terms of length scale. Hence, KPFM can be employed to characterize the homogeneity of the very surface of the absorber thin films including silicon, chalcopyrite, kesterite, and very recently hybrid perovskites.

#### 12.2. KPFM for material characterization

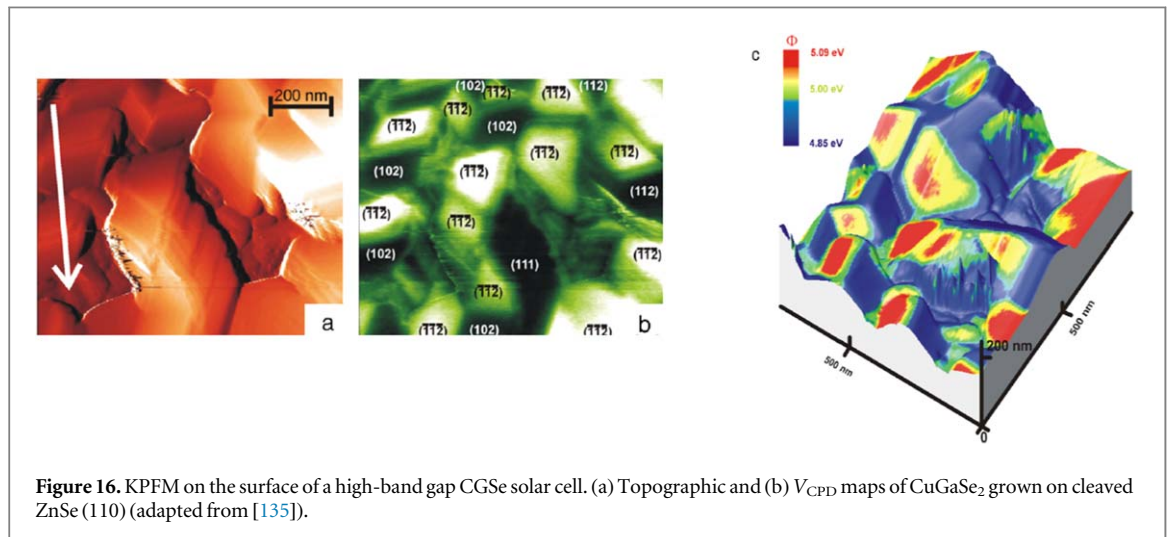
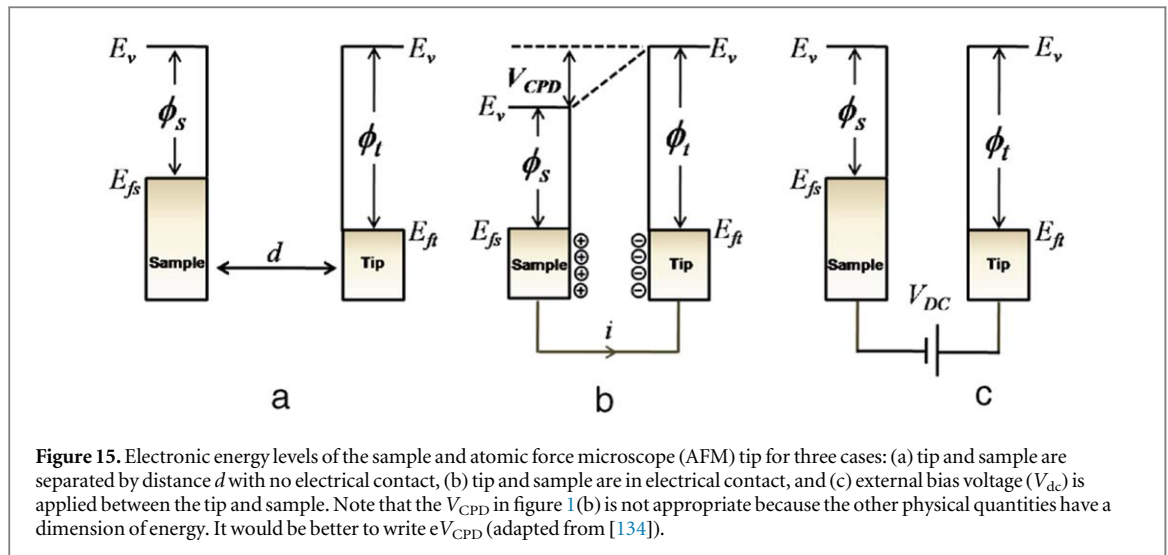
KPFM measures contact potential difference (CPD) between a conductive tip and a sample. When the tip is brought close to the sample surface, an electrical force is generated between the tip and sample surface, due to the differences in their Fermi energy levels. Figure 15 shows the energy level diagram of the tip and sample surface when  $\varphi_s$  and  $\varphi_t$  are different [134]. The amount of applied external bias ( $V_{dc}$ ) that nullifies the electrical force due to the  $V_{CPD}$  is equal to the work function difference between the tip and sample; therefore, the work function of the sample like kesterites can be calculated when the tip work function is known.

As one of the pioneering works using KPFM for solar cells studies, Sadewasser *et al* studied CGSe thin films on ZnSe(110) and CGSe on Mo/glass substrates [135]. KPFM was employed to show that the work function of a thin film is correlated with the crystal growth plane as seen in figure 16. The work function difference between the crystal faces is caused by surface dipoles. The crystal orientation of the films is critical to proper band alignment between the CGSe film and the contacts to maximize efficiency.

### 13. Homogeneity and defects

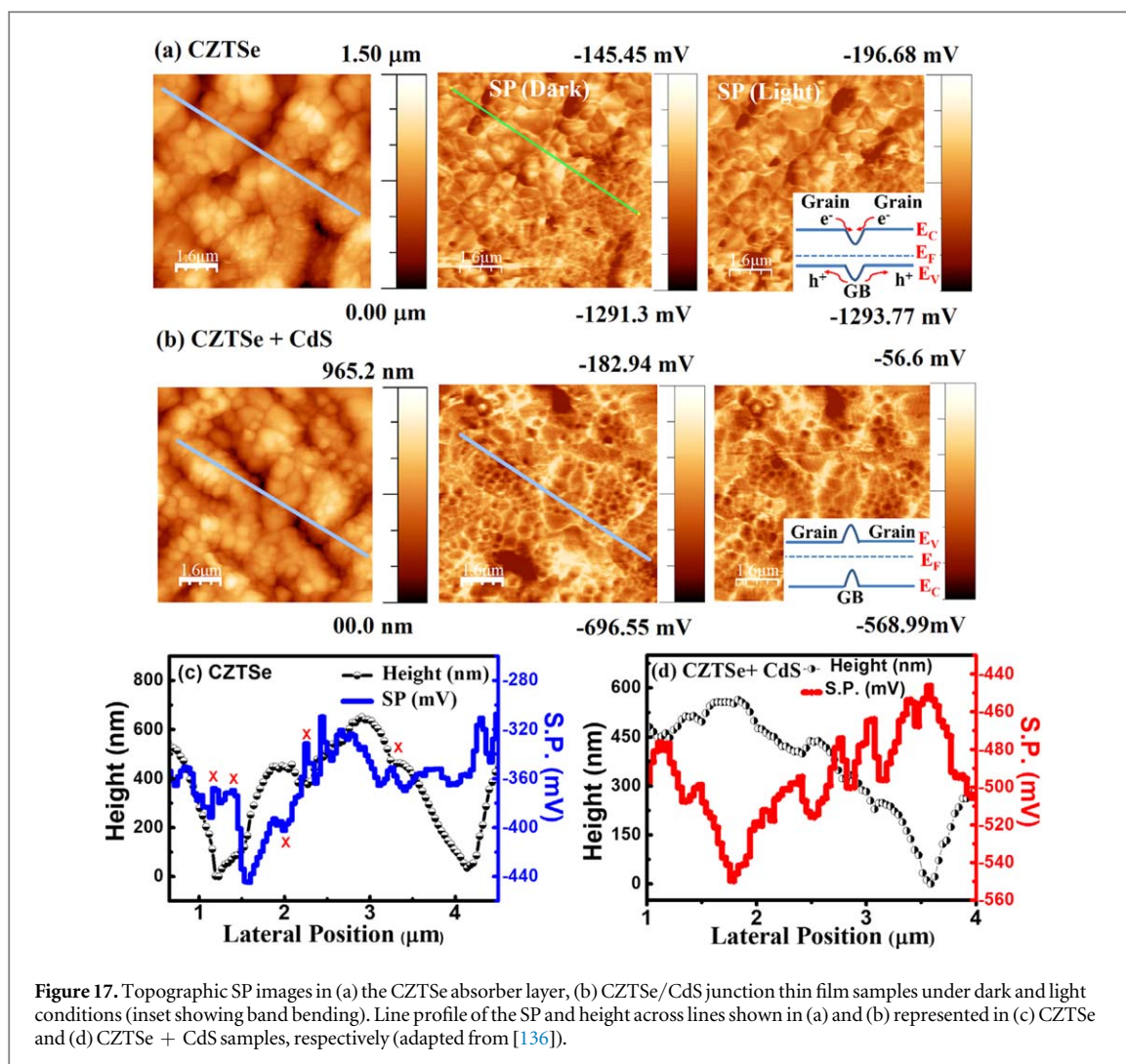
#### 13.1. GBs

In recent years, GBs have become one of the main issues in thin-film polycrystalline solar cells. Unlike chalcopyrite thin films, GBs in high-efficiency kesterite thin films have recently shown downward SP bending [137, 138]. Vishwakarma *et al* reported dark and illuminated surface potentials on the grain boundaries of a CdS/CZTSe photovoltaic device [136]. Figure 17 shows the SP image for CZTSe recorded under dark and light conditions reveals an average SP value of  $-367$  and  $-362$  mV, respectively. A higher SP at some of the granular regions as compared to the GB regions may be due to the presence of defects or secondary phases. The regions in the line profile showing higher SP at GB (upward band bending at GB) may have acceptor-type defects (Cu-Zn anti-sites) or compensated defects, which can be formed at very low energy due to the narrow phase stability



region of the kesterite phase. The phase inhomogeneity because of defects and secondary phases in absorber layer, creates band gap fluctuations across the absorber layer, and has been reported to affect the open circuit voltage or photovoltage of photovoltaic devices. The SP variation in the CZTS (or Se) layer shows downward band bending at the GBs. Downward band bending has been used to explain the increase in  $V_{OC}$  enhancement at the GB with respect to grains. A higher photovoltage at the GB with respect to the grains is observed in general in all the cells. It is well established and has been reported that CZTSe has properties similar to those of the GBs of CZTSSe. Synthesis conditions can affect the SP variations.

Figure 18 shows the scanning capacitance microscopic data of a  $ZnO/CZTS$  sample [139]. This technique is a protocol used to measure the change in the capacitance between the surface and the tip and is similar to that of KPFM. Figure 18(a) shows the topography of the surface featuring different sized grains and figure 18(b) shows the  $dC/dV$  phase image. The presence of two different phases in the line profile analysis indicates the presence of different charge species across the GBs and the charge separation along them. One can find regions of opposite contrast along the GBs as indicated by the highlighted areas corresponding to the topography in figure 4(a). This abrupt change in the phase is observed along the GBs and is at the interface of the grain and GB. This implies that two different charge species are present across the GB. As  $ZnO$  covers the  $CZTS$ , the positive phase features in the  $dC/dV$  phase image represent minority charge carrier species in the  $CZTS$  i.e., electrons, whereas the regions along the GBs which represent the negative phase are hole abundant. Figure 4(c) shows the line profile analysis for the distribution of charge species across the GB as indicated by the line E-F in figure 18(b). The negative phase represented by the blue region corresponds to the majority of charge carriers whereas the minority charge carriers are represented by the positive phase represented by the red region. The presence of the majority of charge carriers, i.e. holes, is not noticed along all the GBs but specifically at the interface of the grain and GB. By



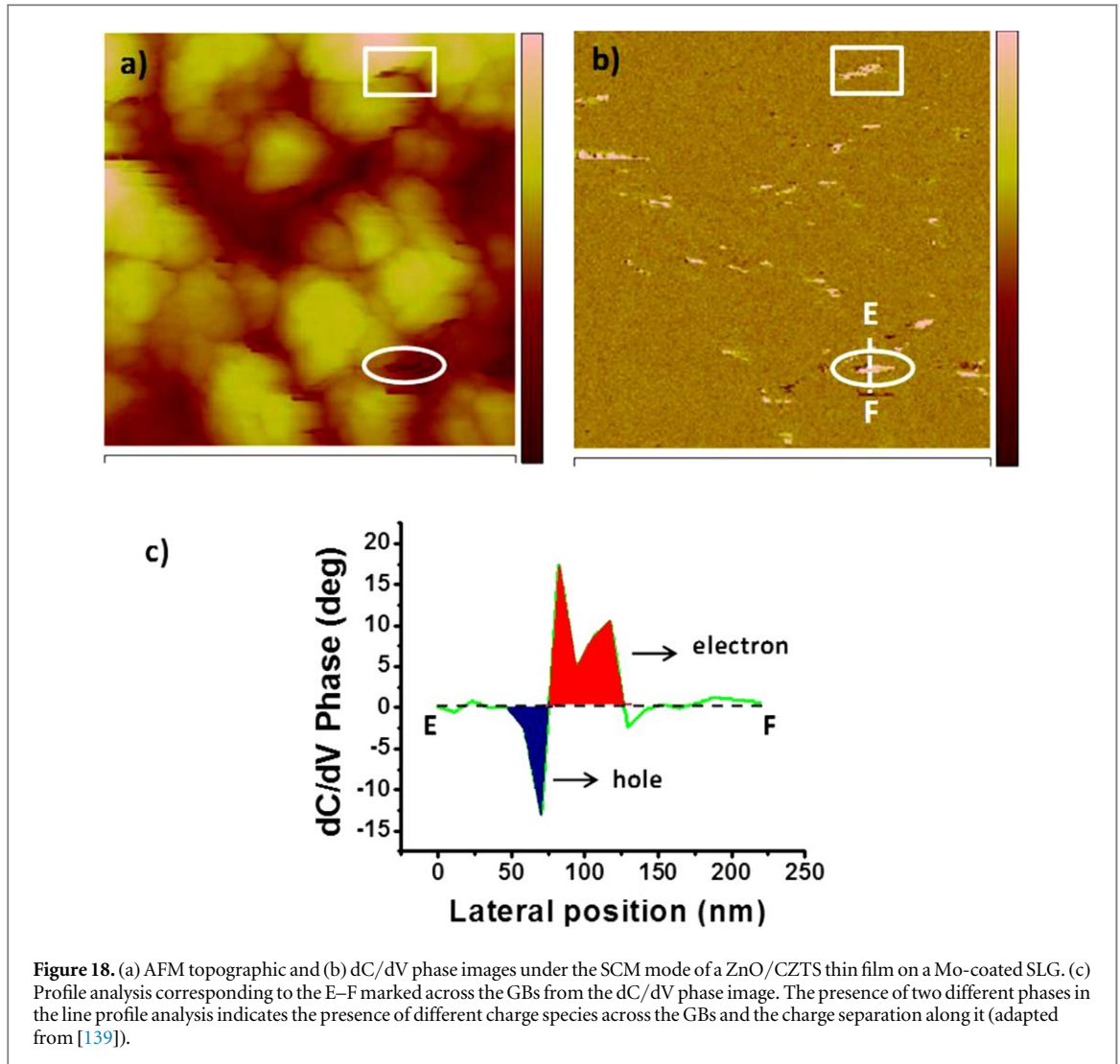
controlling the conditions of the deposition and looking at the SCM phase image one could improve the charge separation, thereby increasing the efficiency of solar cells based on these materials.

Kim *et al* reported current distribution along the GBs of kesterites prepared by compound and metal precursors [140]. Figures 19(a) and (d) show the surface topography of the CZTSSe thin films by compound and metal-precursor, respectively. Figures 19(b) and (e) show surface current maps of them with an external bias of 1.5 V. The technique is referred to as conductive AFM in order to measure current from the materials. When the Pt/Ir-coated tip was in direct contact with the sample surface, the energy bands would bend by matching the Fermi levels of each other. Regarding the barrier potential, the external bias was chosen to be 1.5 V. The line profiles in figures 19(c) and (f) offer exact values on a lateral scale. According to the topography, the red-dotted line indicates the GBs on the surface. For the CZTSSe thin film by compound precursor, the surface current was developed along the GBs. However, the thin film by metal-precursor has less current at the GB while the current flows in the grains. Due to the SP differences between the GB and intergrain (IG) regions, a scarce current development at the GBs is evident. Owing to the electrons that flowed into the IGs and the holes that are held in the GBs, more of the current flows into the IGs. These results are quite opposite to those of the authors' previous studies, where the current is dominantly formed at the GBs.

### 13.2. Alkali effects

Yang *et al* reported beneficial effects of GBs which have an out-of-phase relation between the valleys of the topography and the SP in various stacks of kesterites [141]. Xin *et al* also reported a very interesting result with Li-doping into CZTSSe thin films with dark and illuminated KPFM experiments and enlarged the view of band over the GBs [142]. It is still an open question as to whether sodium and other alkali elements can play a certain role in kesterites in terms of the addition of carrier concentration and passivation of point defects like Cu vacancies or other point defects. Figure 20 depicts the precursor structures of the experiments, and figure 21 describes the surface morphology and SP images of the samples.





### 13.3. Parasitic phases

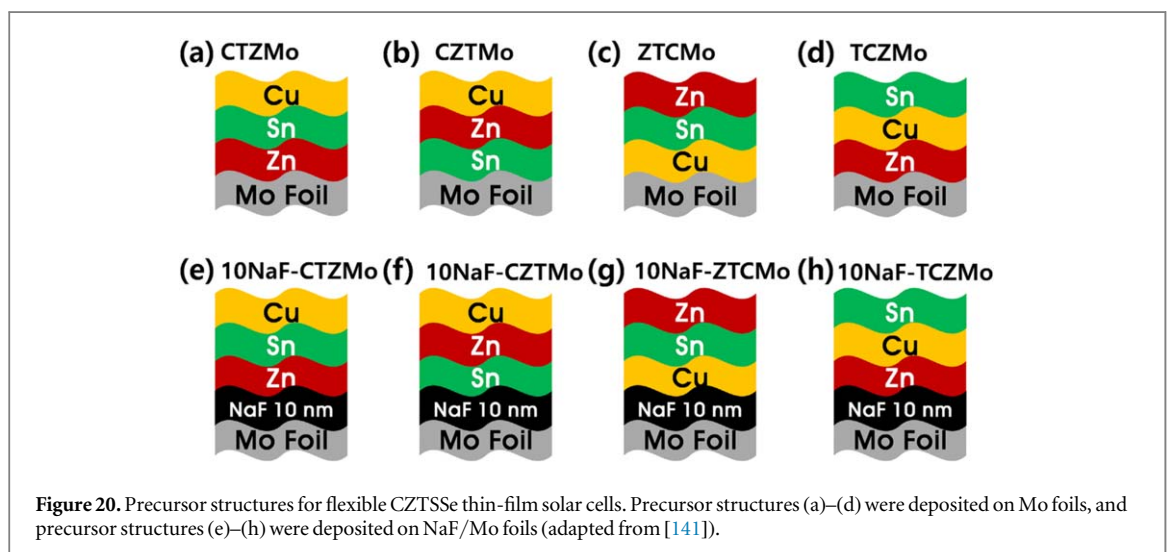
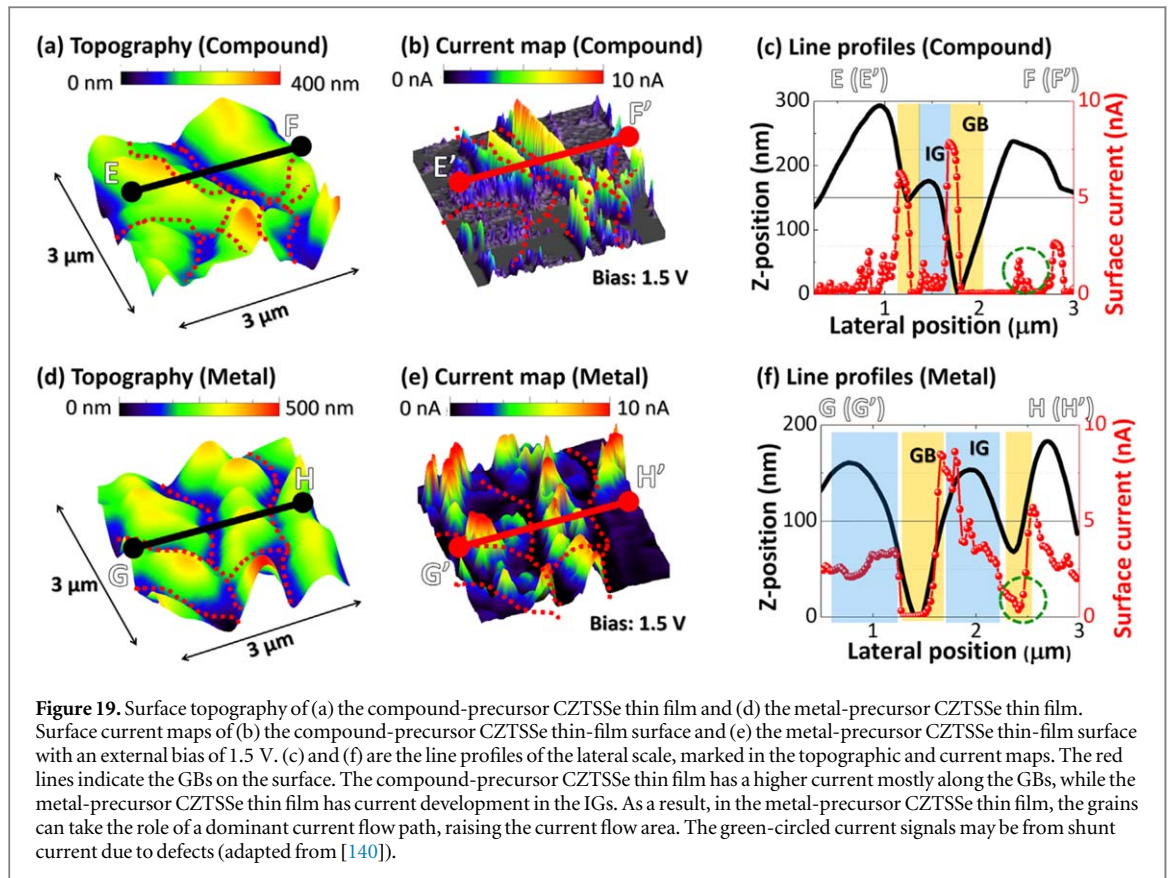
Kim *et al* reported an interesting cross-sectional analysis of kesterite solar cells with different thicknesses of ZnS precursor layers [143]. The top spot of the CZTSSe surface, middle spot of CZTSSe, and the bottom spot of the Mo back contact are shown by a dimpling method. Different work function distributions are shown according to the thickness of the ZnS (in figure 22). The highest efficiency is achieved by the 337 nm film in terms of the uniform work function peak in the top spot. The 337 nm thick ZnS in the CZTSSe film results in a uniform work function peak at the top depth (pure CZTSSe work function  $\sim 4.7$  eV). We obtained a work function for the secondary phases of the ZnSe and MoSe<sub>2</sub> at the middle depths. The unidentified work function peaks can be expected to have been formed from secondary phase peaks that mixed with CZTSSe and with the secondary phases.

Inserting Si or Ge into Sn sites is a way to achieve wide band gap CZTSSe solar cells. Mehta's group reported the results of Cu<sub>2</sub>ZnSiS<sub>4</sub> thin films [144]. Figures 23(a) and (b) show the surface topography and SP images of the thin film samples. The SP distribution is shown in figure 23(c) as a histogram, which clearly shows two distinct peaks. Peak fitting of the above allows deconvolution of the distribution into two peaks, located at  $-572.9$  meV (GBs) and  $-585.7$  meV (IGs), respectively. In the present case the bias during the KPFM measurement is applied to the sample, and therefore,

$$\Phi_s = \Phi_t(5.5 \text{ eV}) + eV_{SP}, \quad (2)$$

where  $\Phi_s$ ,  $\Phi_t$ ,  $e$ , and  $V_{SP}$  are the work function of the sample, the work function of the tip, the electronic charge, and SP, respectively.

The above relation has been used to calculate the work function of IGs and GBs, which are found to be 4.91 and 4.93 eV, respectively. The higher work function at the GBs than at the IGs indicate upward band bending at the GBs in comparison to the IGs. This is opposite to the reported result on Sn-based CZTS material which shows downward band bending at GBs. To study the change in the SP a line profile is drawn across the grains which provides vital information regarding variations in the SP with the change in the Z-position (depth



at GB as the lateral position (X-position) shifts as shown in figure 23(d). The difference in the SP between the GB and the IG is observed in the  $\text{Cu}_2\text{ZnSiS}_4$  thin film. The line profile shows an equivalent SP of  $\sim (-593 \text{ mV})$  at the IGs, with a height of  $0.1 \mu\text{m}$  and a  $0.54 \mu\text{m}$  lateral position and a higher SP of  $\sim (-562 \text{ mV})$  at the GB. Various studies have identified the GB as the accelerator for photovoltaic performance in polycrystalline CIGS, CZTS, and CdTe solar cells.

#### 13.4. Device characteristics

To ensure that the topographic features are not affecting the KPFM images, line profiles were taken across the same pixels on the topographic and SP (in the dark) images of the nanorod and overlaid as shown in figure 24. Clearly, it can be seen that the topography across the entire length is quite uniform. However, the SP data

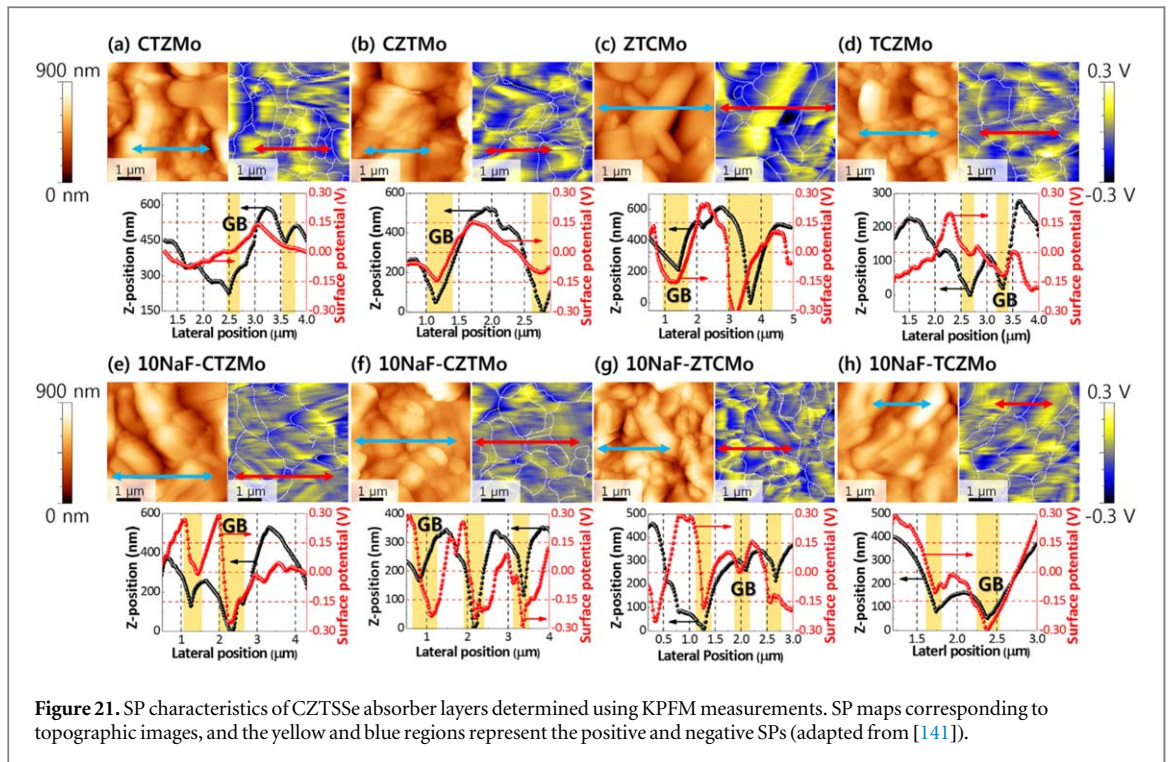


Figure 21. SP characteristics of CZTSSe absorber layers determined using KPFM measurements. SP maps corresponding to topographic images, and the yellow and blue regions represent the positive and negative SPs (adapted from [141]).

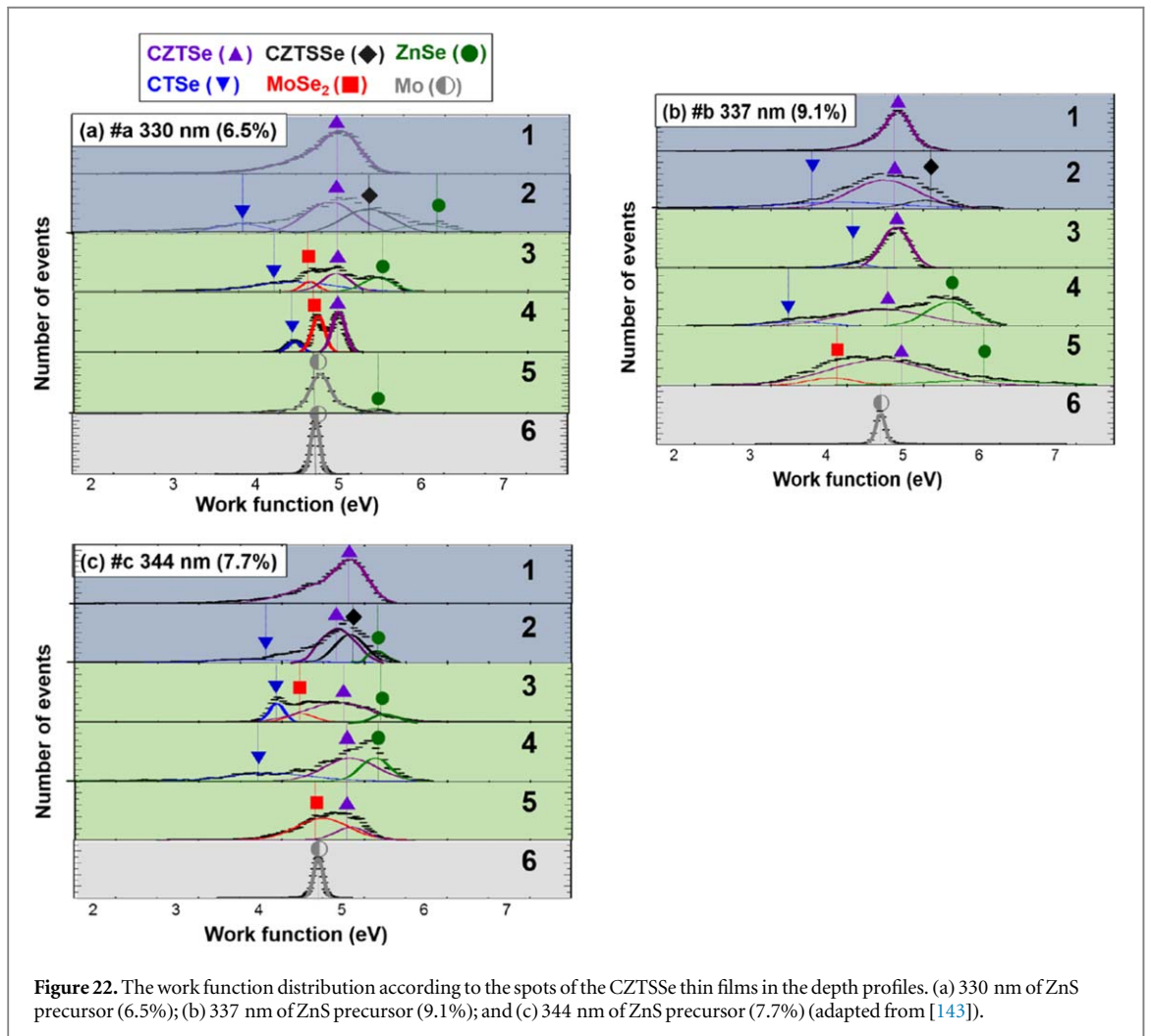
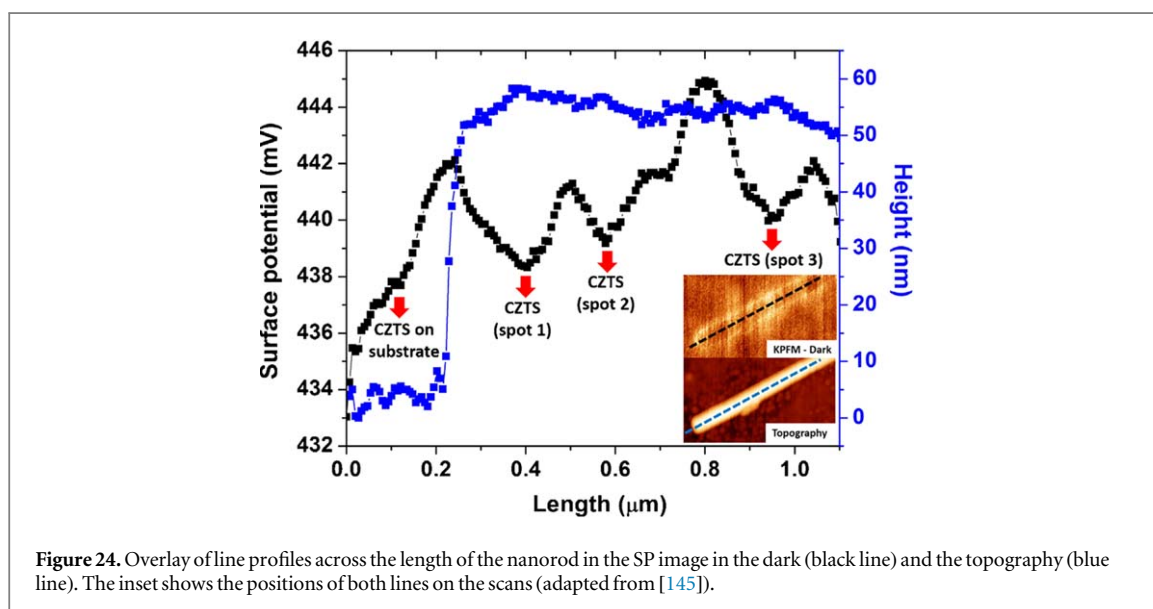
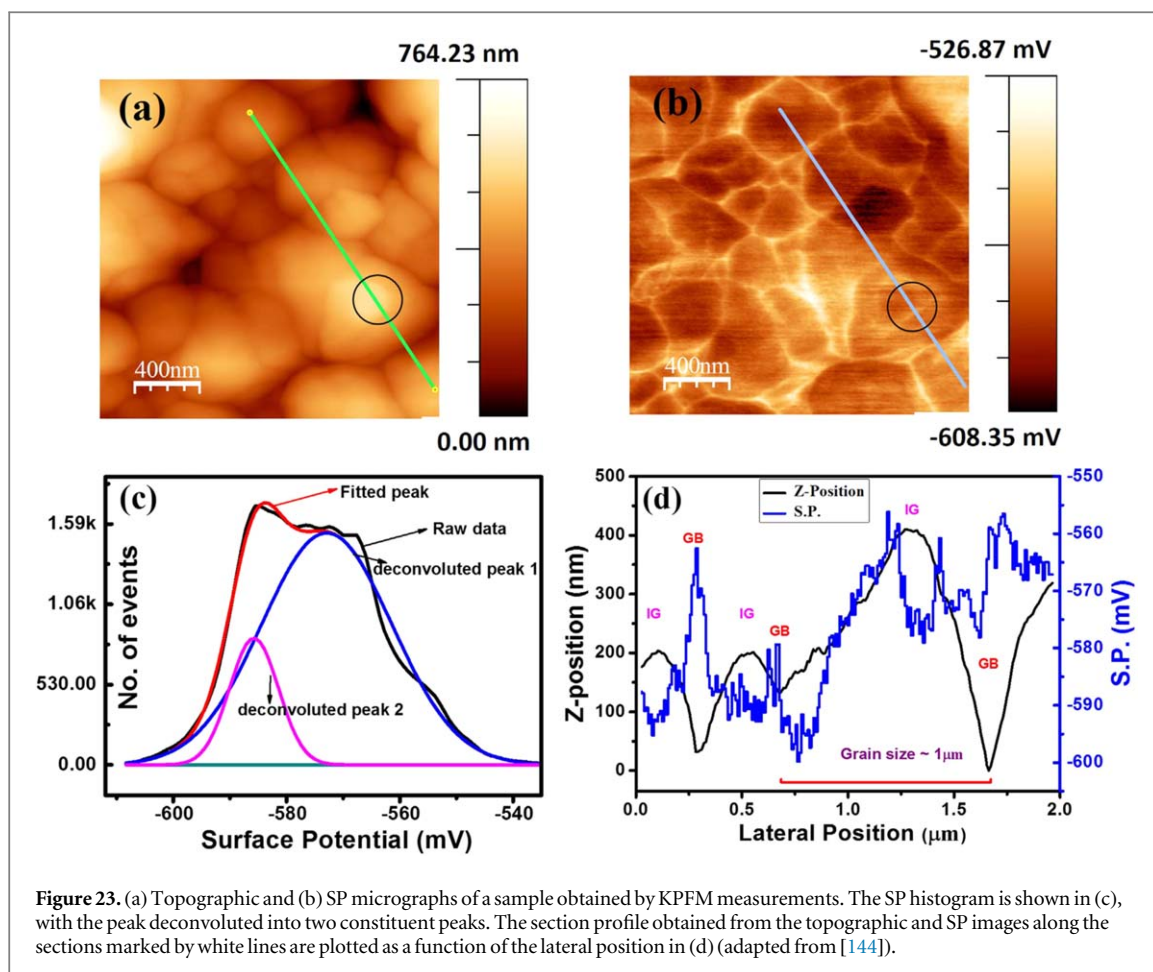


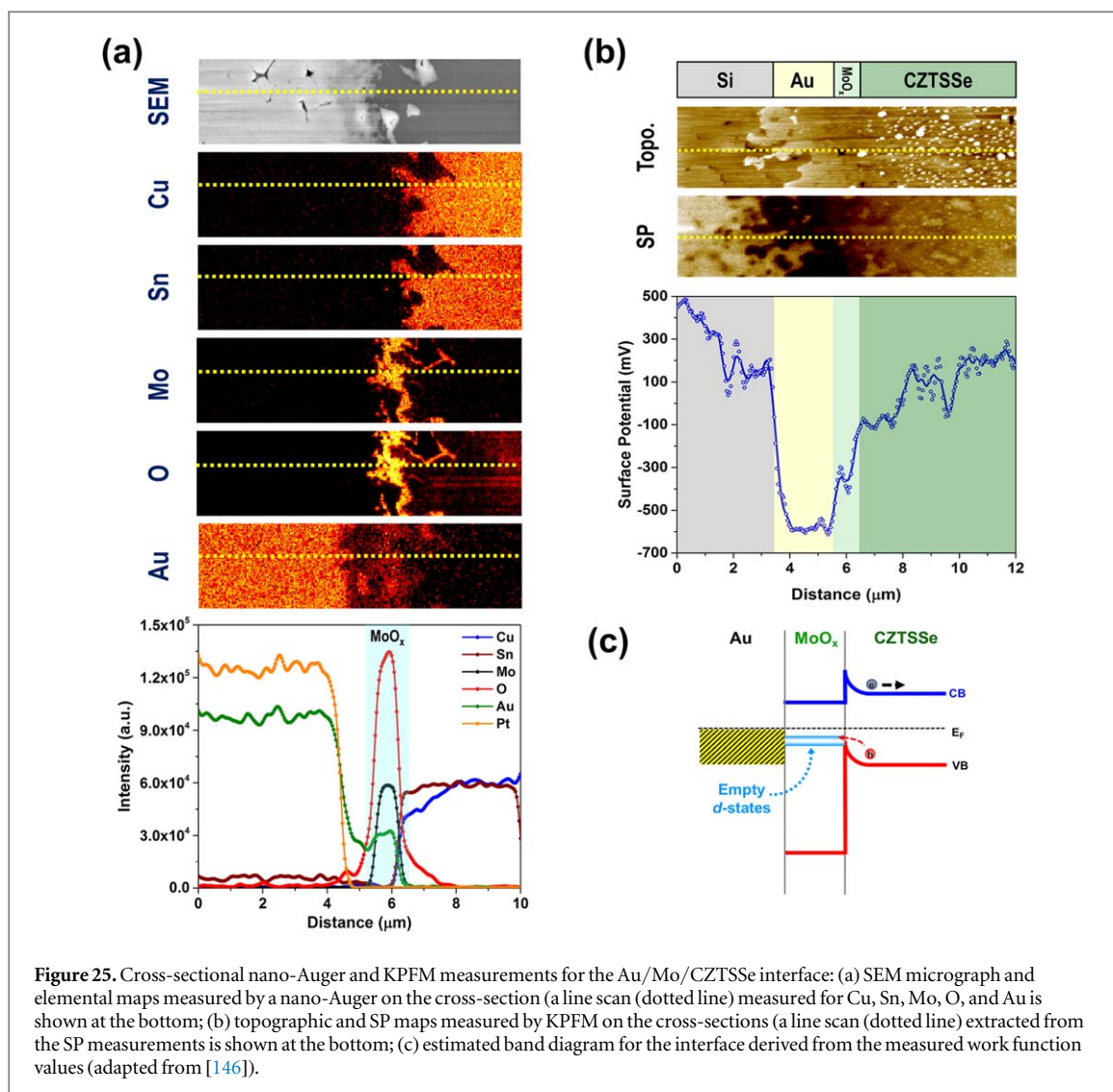
Figure 22. The work function distribution according to the spots of the CZTSSe thin films in the depth profiles. (a) 330 nm of ZnS precursor (6.5%); (b) 337 nm of ZnS precursor (9.1%); and (c) 344 nm of ZnS precursor (7.7%) (adapted from [143]).





distinctively changes across the nanorod depending on whether the point lies on the CdS ( $\sim 443$  mV) or the CZTS ( $\sim 437$  mV). The process of assigning these SPs to the two materials is explained in detail below.

Figure 25 shows an interesting analysis of the device structures with  $\text{MoO}_x$  layers. The topographic and SP maps as well as an SP line scan along the dotted line measured by cross-sectional KPFM on Au/ $\text{MoO}_3$ /CZTS interfaces are displayed in figure 11 (b). For this sample, a Pt/Si/Ti blanket was sputtered prior to cryo-focused ion beam cross-sectioning. A closer look at the line scan reveals that the  $\text{MoO}_x$  layer's work function is about 230 meV smaller than the Au work function. This is in contrast to previous reports that estimated the  $\text{MoO}_3$  work function to be at least 1 eV larger than that of Au. Besides the substoichiometric nature of this oxide



(O/Mo < 3) and air exposure between the evaporation steps, such low work function levels for the MoO<sub>x</sub> could be in part due to the significant amount of Au incorporation. According to the measured work functions and band edge positions, which were measured by femtosecond ultraviolet photoelectron spectroscopy (femtosecond ultraviolet photoemission spectroscopy) as shown in figure 25(c).

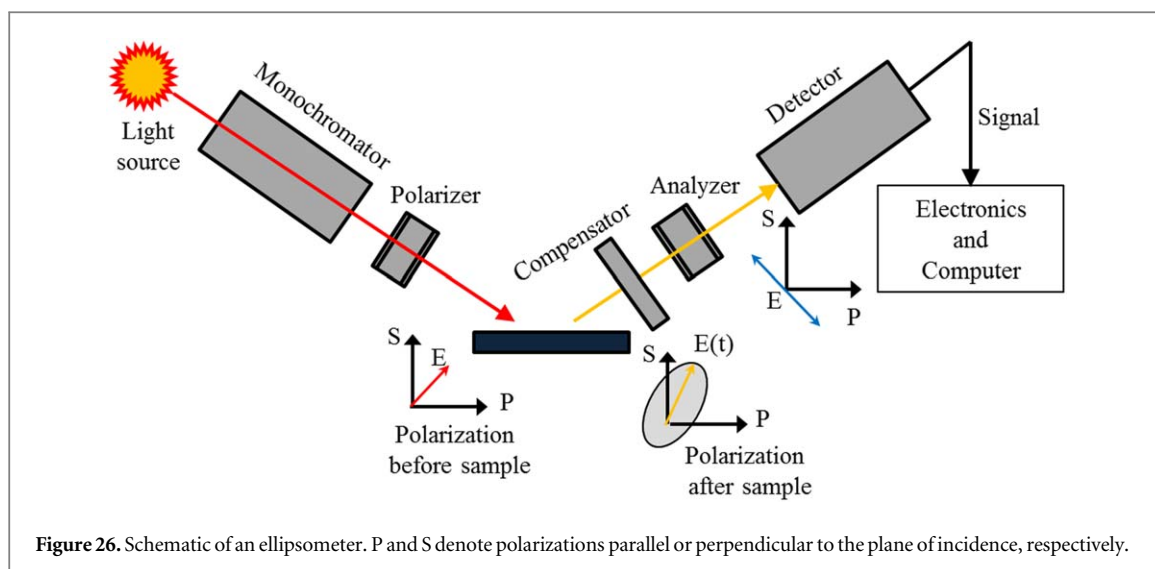
## 14. Conclusions

In summary, KPFM has provided us with significant information on the homogeneity of kesterite thin films with nano-scale length resolution and intrinsic/extrinsic electronic characteristics. By measuring the CPD, we are also able to figure out the work function in addition to the distribution of varied phases. In reality, the CPD is possibly indicative of Fermi levels due to doping concentration but it is also sensitive to the phases in kesterites and related parasitic phases. Moreover, the local fluctuations of the SP measured by KPFM are signs of band bending near SPs or GBs. Thus, KPFM is a very useful tool to elucidate carrier transport in kesterites and other photovoltaic materials.

## E. Ellipsometry and band structure of kesterites

## 15. Introduction

Spectral ellipsometry has been widely used for the experimental characterization of the main energy transitions in Cu<sub>2</sub>Zn(Ge,Sn)(S,Se)<sub>4</sub> compounds, and different approaches have been employed to calculate their electronic



band structure. Many experimental works have paid considerable attention to the identification of the observed transitions based on the existing calculations when possible, so it may be worth gathering the results and conclusions on this topic to identify some open questions that could require further research to achieve clarification.

The spectral ellipsometry (SE) technique analyzes the elliptical polarization of a linearly polarized light after being reflected by a surface (figure 26). The light source can be either a laser or a broad-band source, the latter requiring a monochromator to select a narrow band of frequencies. The light leaving the monochromator is passed through a linear polarizer. After reflection from the sample surface, the light experiences a relative phase shift  $\theta$  between its *s* and *p* polarization components (vertical and horizontal components, respectively) and becomes elliptically polarized. After analysis of these components, the real and imaginary parts of the dielectric function can be obtained, and then the refractive index can be computed.

There are several variations in the method used to detect the ellipticity of the reflected light. In figure 26 a compensator introduces another relative phase shift  $-\theta$  which exactly cancels the ellipticity induced by the reflection, and the light becomes linearly polarized again. This null condition can be easily detected by passing the light through an analyzer, which consists of another linear polarizer oriented to block out the light after the compensator.

## 16. SE and band structure calculations in kesterites

Most of the band structure calculations in the  $\text{Cu}_2\text{Zn}(\text{Ge},\text{Sn})(\text{S},\text{Se})_4$  compounds, along the Brillouin zone, have been performed based on the density-functional theory formalism in combination either with the local density or generalized gradient approximations [147–153], while others are based on a restricted self-consistent GW scheme [154]. It is a common result that the maximum of the valence band (MVB) is mainly formed by the antibonding orbitals from the hybridization of the Cu-d and (S,Se)-p states, while the minimum of the conduction band (MCB) is mainly formed by the antibonding orbitals from the hybridization of the (Ge,Sn)-s and (S,Se)-sp states. The main energy transitions derived from the calculations for several quaternary compounds are summarized in table 5. These values correspond to transitions at high symmetry points in the Brillouin zone from the valence band to the conduction band:  $E_g$  corresponds to the transition between MVB and MCB at the  $\Gamma(\text{G}): (0\ 0\ 0)$  point,  $E_{1A}$  corresponds to the transition at the  $\text{N}(\text{A}): 2\pi/a(\frac{1}{2}\ \frac{1}{2}\ \frac{1}{2})$  point, and  $E_{1B}$  to the transition at the  $\text{T}(\text{Z}): 2\pi/a(0\ 0\ \frac{1}{2})$  point. Other possible transitions have been interpreted by Ozaki *et al* [150], Choi *et al* [151], and Li *et al* [152].

Several features can be observed after these calculations. Some authors [147, 148, 153, 154] have considered different crystallographic structures in their calculations: kesterite [S.G.: $I\bar{4}$ ], stannite [S.G.: $I\bar{4}2m$ ], and primitive-mixed Cu-Au phases (PMCA) [S.G.: $P\bar{4}2m$ ], and even a partially disordered kesterite structure (PD-KS) after Schorr *et al* [164]. Their calculations show that kesterite and stannite

**Table 5.** Theoretically calculated and experimentally obtained by SE energy transition values for  $\text{Cu}_2\text{Zn}(\text{Ge},\text{Sn})(\text{S},\text{Se})_4$  compounds (superscripts correspond to cited references).

Energy transition (eV)	$\text{Cu}_2\text{ZnSnS}_4$			$\text{Cu}_2\text{ZnSnSe}_4$		
	Kesterite (calc.)	Stannite (calc.)	Tetragonal (exp.)	Kesterite (calc.)	Stannite (calc.)	Tetragonal (exp.)
$E_g$	1.50 [147] 1.64 [157]	1.38 [147] 1.27 [157]	1.43–1.50 [155] 1.52–1.58 [158] 1.53–1.67 [100]	0.96 [147] 1.02 [150, 157]	0.82 [147] 0.75 [157]	1.15 [156] 0.93–0.95 [96]
$E_{1A}$	—	—	2.86–2.97 [100]	2.2 [150]	—	2.598 [156] 2.29–2.31 [96]
$E_{1B}$	—	—	4.93–5.02 [100]	2.8 [150]	—	3.566 [156] 3.73–3.92 [96]
Energy transition (eV)	$\text{Cu}_2\text{ZnGeS}_4$			$\text{Cu}_2\text{ZnGeSe}_4$		
	Kesterite (calc.)	Stannite (calc.)	Tetragonal (exp.)	Kesterite (calc.)	Stannite (calc.)	Tetragonal (exp.)
$E_g$	2.43 [153]	2.14 [153]	2.13–2.28 [159] <sup>a</sup>	1.60 [153] 1.18 [154]	1.32 [153] 0.96 [154]	1.41 [154, 160]
$E_{1A}$	2.99 [153]	2.66 [153]	2.85–2.88 [159] <sup>a</sup>	2.35 [153]	1.84 [153]	2.46 [154, 160]
$E_{1B}$	4.10 [153]	3.83 [153]	4.03–4.34 [159] <sup>a</sup>	3.58 [153]	3.17 [153]	3.67 [154, 160]
Energy transition (eV)	$\text{Cu}_2\text{Zn}(\text{Ge}_x\text{Sn}_{1-x})\text{S}_4$ [161, 162] ( $x = 0, 0.1, 0.3, 0.5, 0.7, 0.9, 1$ )			$\text{Cu}_2\text{ZnGe}(\text{S},\text{Se})_4$ [163] $0.8 < \text{S}/(\text{S} + \text{Se}) < 0.87$		
	Tetragonal (exp.)			Tetragonal (exp.)		
$E_g$	1.51–2.25			1.35–1.70		
$E_{1A}$	2.69–3.04			—		
$E_{1B}$	4.01–4.24			—		

<sup>a</sup> Tetragonal structure corresponding to stannite after the authors.

structures exhibit a direct band gap while an indirect transition should appear in the PMCA structure [154]. In addition, apart from the fact that the kesterite structure possesses the lowest formation energy although not significantly smaller than the stannite and PMCA structures, and the PD-KS one results in the highest among the four [147], the band gap value is higher for the kesterite structure [148]. An interesting reason for that has been given by Chen *et al* [153] and Botti *et al* [157]: after their calculations, the band gap energy value is strongly dependent on the anion position in the lattice, which can be considered an indication of the degree of hybridization between the Cu-d and (S,Se)-p states. The higher the anion displacement in the lattice, the larger the bond distance, the weaker the hybridization, the lower the MVB, and thus the higher the gap. The same interesting fact can also be observed when considering the other two  $E_{1A}$  and  $E_{1B}$  transitions: they show higher values for the kesterite structure than for the others.

Considering different anions, S, Se, and Te, Chen *et al* [153] also observed that heavier atoms result in higher MVB states because of the shallower atomic levels of the heavy anions, and the MCB shifts to lower energies with heavier anions due to a higher hybridization of the Ge-s and anion-p states, thereby decreasing the gap. Higher levels in the conduction band can be interpreted from the contribution of (Ge,Sn)-s, Zn-s, and (Ge,Sn)-p states [165]. It is also worth mentioning that Choi *et al* [154] have observed in  $\text{Cu}_2\text{ZnGeSe}_4$  calculations the possibility of multiple transitions at energies around 2.5 eV in the kesterite structure compared to the stannite and PMCA ones.

Regarding the effect of compositional deviations from the stoichiometry, although Chen *et al* [147] have indicated that in  $\text{Cu}_2\text{ZnSnS}_4$  and  $\text{Cu}_2\text{ZnSnSe}_4$  there is a weak dependence of the band structure on the Cu and Zn distributions in the lattice, the same authors [149] have observed in ulterior  $\text{Cu}_2\text{ZnSnS}_4$  calculations that the  $\text{Cu}_{\text{Zn}}$  acceptor defect, dominant in Cu-rich compounds, may affect the MVB, while the  $\text{Zn}_{\text{Cu}}$  donor defect, with  $\text{V}_{\text{Cu}}$  dominant in Cu-poor compounds, may influence the MCB, because of their low defect formation energies. A similar effect has been also pointed out by Hirate *et al* [156] in  $\text{Cu}_2\text{ZnSnSe}_4$  about the  $\text{Cu}_{\text{Zn}}$  acceptor defect, which pushes the MVB up, while the  $\text{Sn}_{\text{Zn}}$  donor defect decreases the MCB.



Complementarily, the energy interband transitions in  $\text{Cu}_2\text{ZnSnS}_4$  [100, 155, 158, 166–168],  $\text{Cu}_2\text{ZnSnSe}_4$  [100, 155],  $\text{Cu}_2\text{ZnGeS}_4$  [159] and  $\text{Cu}_2\text{ZnGeSe}_4$  [160] compounds, as well as their intermediate pseudoquaternary ones,  $\text{Cu}_2\text{Zn}(\text{Ge}, \text{Sn})\text{S}_4$  [161, 162] and  $\text{Cu}_2\text{ZnSn}(\text{S}, \text{Se})_4$  [163] have been characterized by means of SE, in either single crystal, polycrystalline, or thin film forms, from the imaginary part of the dielectric constant. It is interesting to note here that significant efforts are being focused on the analysis of thin films through the modeling of surface roughness, secondary phases, and intermediate layers, with SE emerging as a potential characterization technique for the confirmation of their presence in the growth process [158, 163, 167, 168]. The experimentally obtained energy values are presented in table 5. The agreement between the theoretical predictions and the experimental values is rather satisfactory in most of the cases, given that the energy transitions consistently identified with the interband ones after the theoretical calculations for  $E_g$ ,  $E_{1A}$ , and  $E_{1B}$ . Only Levchenko *et al* [100] have indicated the possibility of  $E_{1A}$  also corresponding to a second conduction band transition at the  $\Gamma(\text{G}):(0\ 0\ 0)$  point.

In many of these works slight variations in the band gap value have been observed depending on the deviations from stoichiometry: in  $\text{Cu}_2\text{ZnSnS}_4$  and  $\text{Cu}_2\text{ZnSnSe}_4$  compounds in thin film form, an increase in the band gap with the  $\text{Cu}/(\text{Zn} + \text{Sn})$  ratio was observed [155], including the intermediate  $\text{Cu}_2\text{ZnSn}(\text{S}, \text{Se})_4$  compounds [163], probably due to a decrease in the MVB level because of a lower degree of hybridization between the Cu-d and (S, Se)-p states, consistent with the theoretical predictions. However, the opposite effect was pointed out by Levchenko *et al* [100] in  $\text{Cu}_2\text{ZnSnS}_4$  polycrystals. The same authors [159] observed a decrease in the  $E_g$  value (and  $E_{1A}$  and  $E_{1B}$  ones) when the Ge/Zn ratio is increased in  $\text{Cu}_2\text{ZnGeS}_4$ , because of a lowering of the MCB, which is also consistent with the band structure calculations.

Considering the intermediate compounds, Garcia-Llamas *et al* [161] observed an increase in the band gap energy with the Ge/Sn ratio, because of the partial substitution of Sn by Ge, and also with the Cu content, due to a decrease in the MVB, cases following the Vegard law for quaternary compounds. Sengar *et al* [163] identified the same increase in the  $E_g$  value with the S/(S + Se) ratio, which is also expected considering the quaternary end compounds.

## 17. Conclusions

In summary, SE has proved to be a powerful characterization technique to identify and confirm to a reasonable degree the interband energy transitions predicted by theoretical calculations of the electronic band structure even in complicated compounds as those known as kesterites. SE has the disadvantage of needing strong support from theoretical calculations to fully interpret the origin of the observed critical points. Further studies on the possible influence of the Zn, Sn and/or Ge cations in the variations of the transition energies, in particular, those transitions above the fundamental one, might be useful to help in the comprehension of their more specific roles and effects, both experimentally and theoretically, as the optical properties of the absorber materials play a very important role in determining the efficiency of photovoltaic devices.

## Discussion

Typical features of kesterite-type materials are a pronounced off-stoichiometric composition and associated formation of secondary phases. The correlation between stoichiometry deviations, which can be expressed by the cation ratios and intrinsic point defects has been established by the off-stoichiometry model. Besides the off-stoichiometry related point defect Cu/Zn disorder ( $\text{Zn}_{\text{Cu}}$  and  $\text{Cu}_{\text{Zn}}$  anti-sites) is always present in kesterite-type compounds. This lack of compositional and structural homogeneity may severely alter the electrical and optical properties of the kesterite-type material. Therefore it must also be noted that an integral thin film composition is not a reliable measure for the characterization of highly non-stoichiometric kesterites.

Several analytical methods have been applied to study structural (point defects and Cu/Zn disorder) and compositional homogeneity (off-stoichiometry and secondary phases) on a macroscopic and microscopic scale and even on the nano-scale. Diffraction methods (x-ray and neutron diffraction) have revealed in detail the structural origin of point defects in off-stoichiometric kesterites. Synchrotron-based high-resolution x-ray fluorescence analysis and x-ray absorption spectroscopy provide unique contributions to the identification and quantification of secondary phases and compositional fluctuations in non-stoichiometric kesterite materials. Fast qualitative results about quaternary and secondary phase formation, crystal quality, and the crystal structure of the main phase can be obtained by Raman spectroscopy. With a deeper higher level analysis of Raman spectra at different stages of the thin film growth process, information can be gained about the formation mechanism of the phases, the optimum deposition conditions, and post-deposition treatment. Micro and macro Raman mappings yield information about the homogeneity of all the mentioned parameters at the surface or in a depth profile of the obtained polycrystalline absorber layer. Also KPFM provides significant information on the homogeneity of absorber thin films with

nano-scale length resolution and intrinsic/extrinsic electronic characteristics. Local fluctuations of the SP measured by KPFM are signs of band bending near the surface or the GBs. Additionally KPFM is a very useful tool to elucidate carrier transport in kesterite-type and other photovoltaic materials. Interband energy transitions in kesterites, predicted by theoretical calculations of the electronic band structure even in such complex quaternary compounds can be identified by spectroscopic ellipsometry.

Further progress in kesterite-based thin film devices could be inspired by the discussed structure-property relationships opening possibilities for optimized thin film processing.

## Current challenges and future prospects

The kesterite-type compound semiconductor CZTSSe may be the counterpart of Cu(In,Ga)Se<sub>4</sub> absorber layers in thin film solar cells and the efficiency may be increased up to 32.2% as theoretically predicted by the Shockley–Queisser limit. But there are a number of challenges connected to the structural properties and the chemical homogeneity of this material which have been in the focus of this paper.

- (i) A variety of secondary phases are easily and frequently formed throughout the absorber layer. Standard preparation conditions have to be found that avoid secondary phases, ideally for many different types of growth processes (sputtered, co-evaporated, solution-based, etc.).
- (ii) The local composition of the kesterite-type phase(s) differs from the integral sample composition. Thus the local composition needs to be measured routinely, which is experimentally demanding and time-consuming.
- (iii) The kesterite-type crystal structure can accommodate large deviations from stoichiometry, which is necessarily accompanied by a large number of different intrinsic point defects. It must be determined unambiguously which of these point defects are detrimental, benign, or even beneficial. Furthermore, thin film preparation conditions need to be identified, which allow the growth of a thin film with a certain chemical composition to avoid dangerous compositional regions reliably.

Finally the challenges that need to be addressed in order to reach competitive performance levels are the improvement of the homogeneity of the material in the polycrystalline absorber layer as well as a precise control of the (local and integral) composition of the kesterite phase.

## Acknowledgments

This research was supported by the H2020 Programme under the project INFINITE-CELL (H2020-MSCA-RISE-2017-777968). The authors from IREC and Universidad Autónoma de Madrid acknowledge funding from the Spanish Ministry of Science, Innovation and Universities by WINCOST (ENE2016-80788-C5-1-R), and by the European Regional Development Funds (ERDF; FEDER Programa Competitivitat de Catalunya 2007–2013). The authors from IREC and the University of Barcelona belong to the SEMS (Solar Energy Materials and Systems) Consolidated Research Group of the ‘Generalitat de Catalunya’ (Ref. 2017 SGR 862). M D gratefully acknowledges support from the Hydrogen Materials—Advanced Research Consortium (HyMARC), established as part of the Energy Materials Network under the US Department of Energy, Office of Energy Efficiency and Renewable Energy (DOE EERE), Fuel Cell Technologies Office, under Contract No. DE-AC36-08GO28308.

## ORCID iDs

Susan Schorr  <https://orcid.org/0000-0002-6687-614X>  
Galina Gurieva  <https://orcid.org/0000-0001-8609-1043>  
Maxim Guc  <https://orcid.org/0000-0002-2072-9566>  
Claudia S Schnohr  <https://orcid.org/0000-0002-3688-7104>  
William Jo  <https://orcid.org/0000-0002-9917-7222>  
José Manuel Merino  <https://orcid.org/0000-0003-0060-4843>

## References

- [1] Schorr S, Höbner H-J and Tovar M 2007 A neutron diffraction study of the stannite-kesterite solid solution series *Eur. J. Mineral.* **19** 65
- [2] Schorr S 2011 The crystal structure of kesterite type compounds: a neutron and x-ray diffraction study *Sol. Energy Mater. Sol. Cells* **95** 1482

- [3] Gurieva G, Dimitrievska M, Zander S, Pérez-Rodríguez A, Izquierdo-Roca V and Schorr S 2015 Structural characterisation of  $\text{Cu}_{2.04}\text{Zn}_{0.91}\text{Sn}_{1.05}\text{S}_{2.08}\text{Se}_{1.92}$  *Phys. Stat. Sol. C* **12** 588
- [4] Gunder R, Marquez-Prieto J A, Gurieva G, Unold T and Schorr S 2018 Structural characterization of off-stoichiometric kesterite-type  $\text{Cu}_2\text{ZnGeSe}_4$  compound semiconductors: from cation distribution to intrinsic point defect density *Cryst. Eng. Comm.* **20** 1491
- [5] Hall S R, Szymanski J T and Stewart J M 1978 Kesterite,  $\text{Cu}_2(\text{Zn,Fe})\text{SnS}_4$ , and stannite,  $\text{Cu}_2(\text{Fe,Zn})\text{SnS}_4$ , structurally similar but distinct minerals *Can. Mineral.* **16** 131
- [6] Valakh M Y et al 2013 Raman scattering and disorder effect in  $\text{Cu}_2\text{ZnSnS}_4$  *Phys. Status Solidi RRL* **7** 258
- [7] Ericson T, Scragg J, Kubart T, Törndahl T and Platzer-Björkman C 2013 Annealing behaviour of reactively sputtered precursor films for  $\text{Cu}_2\text{ZnSnS}_4$  solar cells *Thin Solid Films* **535** 22
- [8] Schorr S and Gonzalez-Aviles G 2009 *In-situ* investigation of the structural phase transition in kesterite *Phys. Status Solidi A* **206** 1054
- [9] Scragg J J S, Choubrac L, Lafond A, Ericson T and Platzer-Björkman C 2014 A low-temperature order-disorder transition in  $\text{Cu}_2\text{ZnSnS}_4$  thin films *Appl. Phys. Lett.* **104** 041911
- [10] Rey G, Redinger A, Sendler J, Weiss T P, Thevenin M, Guennou M, El Adib B and Siebentritt S 2014 The band gap of  $\text{Cu}_2\text{ZnSnSe}_4$ : Effect of order-disorder *Appl. Phys. Lett.* **105** 112106
- [11] Toebbens D M, Gurieva G, Levchenko S, Unold T and Schorr S 2016 Thermal dependency of Cu/Zn ordering in CZTSe kesterites determined by anomalous diffraction *Phys. Status Solidi B* **253** 1890
- [12] Wang W, Winkler M T, Gunawan O, Gokmen T, Todorov T K, Zhu Y and Mitzi D B 2014 Device characteristics of CZTSSe thin-film solar cells with 12.6% efficiency *Adv. Energy Mater.* **4** 1301465
- [13] Chen S, Walsh A, Gong X-G and Wei S-H 2013 Classification of lattice defects in the kesterite  $\text{Cu}_2\text{ZnSnS}_4$  and  $\text{Cu}_2\text{ZnSnSe}_4$  earth-abundant solar cell absorbers *Adv. Mater.* **25** 1522
- [14] Gershon T, Lee Y S, Antunez P, Mankad R, Singh S, Bishop D, Gunawan O, Hopstaken M and Haight R 2016 Photovoltaic materials and devices based on the alloyed kesterite absorber  $(\text{Ag}_x\text{Cu}_{1-x})_2\text{ZnSnSe}_4$  *Adv. Energy Mater.* **6** 1502468
- [15] Valle Rios L E, Neldner K, Gurieva G and Schorr S 2016 Existence of off-stoichiometric single phase kesterite *J. Alloys Compd.* **657** 408
- [16] Gurieva G, Valle Rios L E, Franz A, Whitfield P and Schorr S 2018 Intrinsic point defects in off-stoichiometric  $\text{Cu}_2\text{ZnSnSe}_4$ : a neutron diffraction study *J. Appl. Phys.* **213** 161519
- [17] Lafond A, Choubrac L, Guillot-Deudon C, Deniard P and Jobic S 2012 Crystal structures of photovoltaic chalcogenides, an intricate puzzle to solve: the cases of CIGSe and CZTS materials *Z. Anorg. Allg. Chem.* **638** 2571
- [18] Gurieva G, Ferreira R, Knoll P and Schorr S 2018  $\text{Cu}_2\text{ZnSnSe}_4$ : how far does off-stoichiometry go? *Phys. Status Solidi A* **215** 1700957
- [19] Schorr S, Stephan C, Törndahl T, Gunder R and Többsen D M X-ray and neutron diffraction on materials for thin-film solar cells 2016 *Advanced Characterization Techniques for Thin Film Solar Cells* ed D Abou-Ras et al (New York: Wiley)
- [20] Raman C V and Krishnan K S 1928 A new type of secondary radiation *Nature* **121** 501
- [21] Landsberg G S 1958 *Selected Works* (Moscow: AN SSSR) pp 101–10 (in Russian)
- [22] Mandelstam L I 1947 *Complete Collection of Works* vol I (Moscow: AN SSSR) pp 293–305 (In Russian)
- [23] Yu P Y and Cardona M 2010 *Fundamentals of Semiconductors: Physics and Materials Properties* 4th edn (New York: Springer Heidelberg) pp 375–426
- [24] Gardiner D J and Graves P R 1989 *Practical Raman Spectroscopy* (New York: Springer-Verlag Berlin Heidelberg)
- [25] Lewis I R and Edwards H G M 2001 *Handbook of Raman Spectroscopy* (New York: Marcel Dekker Inc)
- [26] Sushinskii M M 1969 *Raman Scattering Spectra of Molecules and Crystals* (Moscow: Nauka) (in Russian)
- [27] Placzek G 1934 Rayleigh streuung und Raman effekt *Hdb. der Radiologie* **6** 209 (in German)
- [28] Pistor P, Ruiz A, Cabot A and Izquierdo-Roca V 2016 Advanced Raman spectroscopy of methylammonium lead iodide: development of a non-destructive characterisation methodology *Sci. Rep.* **6** 35973
- [29] Guc M, Tsini F, Rousset J, Romanyuk Y E, Izquierdo-Roca V and Pérez-Rodríguez A 2017 Non-destructive Raman scattering assessment of solution-processed ZnO doped layers for photovoltaic applications *J. Phys. Chem. C* **121** 3212
- [30] Nitsche R, Sargent D F and Wild P 1967 Crystal growth of quaternary 122464 chalcogenides by iodine vapor transport *J. Cryst. Growth* **1** 52
- [31] Schafer W and Nitsche R 1974 Tetrahedral quaternary chalcogenides of the type  $\text{Cu}_2\text{-II-IV-S}_4(\text{Se}_4)$  *Mater. Res. Bull.* **9** 645
- [32] Schorr S 2011 The crystal structure of kesterite type compounds: a neutron and x-ray diffraction study *Sol. Energy Mater. Sol. Cells* **95** 1482
- [33] Guc M, Levchenko S, Izquierdo-Roca V, Fontane X, Arushanov E and Pérez-Rodríguez A 2013 Polarized Raman scattering analysis of  $\text{Cu}_2\text{ZnSnSe}_4$  and  $\text{Cu}_2\text{ZnGeSe}_4$  single crystals *J. Appl. Phys.* **114** 193514
- [34] Himmrich M and Haeuselner H 1991 Far infrared studies on stannite and wurtzstannite type compounds *Spectrochim. Acta* **47A** 933
- [35] Dimitrievska M, Boero F, Litvinchuk A P, Delsante S, Borzone G, Perez-Rodríguez A and Izquierdo-Roca V 2017 Structural polymorphism in 'kesterite'  $\text{Cu}_2\text{ZnSnS}_4$ : Raman spectroscopy and first-principles calculations analysis *Inorg. Chem.* **56** 3467
- [36] Levchenko S, Nateprov A, Kravtsov V, Guc M, Pérez-Rodríguez A, Izquierdo-Roca V, Fontané X and Arushanov E 2014 Structural study and Raman scattering analysis of  $\text{Cu}_2\text{ZnSiTe}_4$  bulk crystals *Opt. Express* **22** A1936
- [37] Rincón C, Quintero M, Moreno E, Power C, Quintero E, Henao J A, Macías M A, Delgado G E, Tovar R and Morocoima M 2011 X-ray diffraction, Raman spectrum and magnetic susceptibility of the magnetic semiconductor  $\text{Cu}_2\text{FeSnS}_4$  *Solid State Commun.* **151** 947
- [38] Dumcenco D and Huang Y-S 2013 The vibrational properties study of kesterite  $\text{Cu}_2\text{ZnSnS}_4$  single crystals by using polarization dependent Raman spectroscopy *Opt. Mater.* **35** 419
- [39] Nam D, Kim J, Lee J-U, Nagaoka A, Yoshino K, Cha W, Kim H, Hwang I C, Yoon K B and Cheong H 2014 Polarized Raman spectroscopy of Cu-poor and Zn-rich single-crystal  $\text{Cu}_2\text{ZnSnSe}_4$  *Appl. Phys. Lett.* **105** 173903
- [40] Guc M, Levchenko S, Bodnar I V, Izquierdo-Roca V, Fontane X, Volkova L V, Arushanov E and Pérez-Rodríguez A 2016 Polarized Raman scattering study of kesterite type  $\text{Cu}_2\text{ZnSnS}_4$  single crystals *Sci. Rep.* **6** 19414
- [41] Guc M, Litvinchuk A P, Levchenko S, Valakh M Y, Bodnar I V, Dzhan V M, Izquierdo-Roca V, Arushanov E and Perez-Rodríguez A 2016 Optical phonons in the kesterite  $\text{Cu}_2\text{ZnGeS}_4$  semiconductor: polarized Raman spectroscopy and first-principle calculations *RSC Adv.* **6** 13278
- [42] Valakh M Y, Litvinchuk A P, Dzhan V M, Yukhymchuk V O, Yaremko A M, Romanyuk Y A, Guc M, Bodnar I V, Pérez-Rodríguez A and Zahn D R T 2016 Fermi resonance in the phonon spectra of quaternary chalcogenides of the type  $\text{Cu}_2\text{ZnGeS}_4$  *J. Phys. Condens. Matter* **28** 065401
- [43] Rincon C, Quintero M, Power C, Moreno E, Quintero E, Henao J A, Macias M A and Morocoima M 2015 Raman spectra of  $\text{Cu}_2\text{B}^{\text{II}}\text{C}^{\text{IV}}\text{X}_4^{\text{VI}}$  magnetic quaternary semiconductor compounds with tetragonal stannite type structure *J. Appl. Phys.* **117** 205701



- [43] Dimitrievska M, Fairbrother A, Fontane X, Jawhari T, Izquierdo-Roca V, Saucedo E and Perez-Rodríguez A 2014 Multiwavelength excitation Raman scattering study of polycrystalline kesterite  $\text{Cu}_2\text{ZnSnS}_4$  thin films *Appl. Phys. Lett.* **104** 021901
- [44] Dimitrievska M, Xie H, Fairbrother A, Fontane X, Gurieva G, Saucedo E, Perez-Rodríguez A, Schorr S and Izquierdo-Roca V 2014 Multiwavelength excitation Raman scattering of  $\text{Cu}_2\text{ZnSn}(\text{S}_x\text{Se}_{1-x})_4$  ( $0 \leq x \leq 1$ ) polycrystalline thin films: Vibrational properties of sulfoselenide solid solutions *Appl. Phys. Lett.* **105** 031913
- [45] Garcia-Llamas E, Guc M, Bodnar I V, Fontané X, Caballero R, Merino J M, León M and Izquierdo-Roca V 2017 Multiwavelength excitation Raman scattering of  $\text{Cu}_2\text{ZnSn}_{1-x}\text{Ge}_x(\text{S},\text{Se})_4$  single crystals for earth abundant photovoltaic applications *J. Alloy Compd.* **692** 249
- [46] Fontané X, Izquierdo-Roca V, Saucedo E, Schorr S, Yukhymchuk V O, Valakh M Y, Pérez-Rodríguez A and Morante J R 2012 Vibrational properties of stannite and kesterite type compounds: Raman scattering analysis of  $\text{Cu}_2(\text{Fe},\text{Zn})\text{SnS}_4$  *J. Alloy Compd.* **539** 190
- [47] Pilvet M, Kauk-Kuusik M, Altosaar M, Grossberg M, Danilson M, Timmo K, Mere A and Mikli V 2015 Compositionally tunable structure and optical properties of  $\text{Cu}_{1.85}(\text{Cd}_x\text{Zn}_{1-x})_{1.1}\text{SnS}_{4.1}$  ( $0 \leq x \leq 1$ ) monograin powders *Thin Solid Films* **582** 180
- [48] Rincón C, Quintero M, Moreno E, Power C, Quintero E, Henao J A and Macías M A 2015 Raman spectrum of  $\text{Cu}_2\text{CdSnSe}_4$  stannite structure semiconductor compound *Superlattice Microstruct.* **88** 99
- [49] Grossberg M, Krustok J, Raudoja J and Raadik T 2012 The role of structural properties on deep defect states in  $\text{Cu}_2\text{ZnSnS}_4$  studied by photoluminescence spectroscopy *Appl. Phys. Lett.* **101** 102102
- [50] Chen L, Deng H, Cuia J, Tao J, Zhou W, Cao H, Sun L, Yang P and Chu J 2015 Composition dependence of the structure and optical properties of  $\text{Cu}_2\text{Mn}_x\text{Zn}_{1-x}\text{SnS}_4$  thin films *J. Alloy Compd.* **627** 388
- [51] Amiri N B M and Postnikov A 2010 Electronic structure and lattice dynamics in kesterite-type  $\text{Cu}_2\text{ZnSnSe}_4$  from first-principles calculations *Phys. Rev. B* **82** 205204
- [52] Gurel T, Sevik C and Cagin T 2011 Characterization of vibrational and mechanical properties of quaternary compounds  $\text{Cu}_2\text{ZnSnS}_4$  and  $\text{Cu}_2\text{ZnSnSe}_4$  in kesterite and stannite structures *Phys. Rev. B* **84** 205201
- [53] Khare A, Himmetoglu B, Johnson M, Norris D J, Cococcioni M and Aydil E S 2012 Calculation of the lattice dynamics and Raman spectra of copper zinc tin chalcogenides and comparison to experiments *J. Appl. Phys.* **111** 083707
- [54] Khare A, Himmetoglu B, Cococcioni M and Aydil E S 2012 First principles calculation of the electronic properties and lattice dynamics of  $\text{Cu}_2\text{ZnSn}(\text{S}_{1-x}\text{Se}_x)_4$  *J. Appl. Phys.* **111** 123704
- [55] Valakh M Y, Litvinchuk A P, Dzhagan V M, Yukhymchuk V O, Havryliuk Y O, Guc M, Bodnar I V, Izquierdo-Roca V, Perez-Rodríguez A and Zahn D R T 2016 Optical properties of quaternary kesterite-type  $\text{Cu}_2\text{Zn}(\text{Sn}_{1-x}\text{Ge}_x)\text{S}_4$  crystalline alloys: Raman scattering, photoluminescence and first-principle calculations *RSC Adv.* **6** 67756
- [56] Li G, Blake G R and Palstra T T M 2017 Vacancies in functional materials for clean energy storage and harvesting: the perfect imperfection *Chem. Soc. Rev.* **46** 1693
- [57] Dimitrievska M, Fairbrother A, Perez-Rodríguez A, Saucedo E and Izquierdo-Roca V 2014 Raman scattering crystalline assessment of polycrystalline  $\text{Cu}_2\text{ZnSnS}_4$  thin films for sustainable photovoltaic technologies: phonon confinement model *Acta Mater.* **70** 272
- [58] Li C, Cao M, Huang J, Sun Y, Wang L J and Shen Y 2014 Effects of S and Se contents on the physical and photovoltaic properties of  $\text{Cu}_2\text{ZnSn}(\text{S}_x\text{Se}_{1-x})_4$  nanoparticles *J. Alloy Compd.* **616** 542
- [59] Li Y, Ling W, Han Q and Shi W 2014 Colloidal  $\text{Cu}_2\text{Zn}(\text{Sn}_{1-x}\text{Ge}_x)\text{S}_4$  nanocrystals: electrical properties and comparison between their wurtzite and kesterite structures *RSC Adv.* **4** 55016
- [60] Shavel A et al 2016 Scalable heating-up synthesis of monodisperse  $\text{Cu}_2\text{ZnSnS}_4$  nanocrystals *Chem. Mater.* **28** 720
- [61] Nemanich R J, Solin S A and Martin R M 1981 Light scattering study of boron nitride microcrystals *Phys. Rev. B* **23** 6348
- [62] Lafond A, Choubrac L, Guillot-Deudon C, Fertey P, Evain M and Jobic S 2014 X-ray resonant single-crystal diffraction technique, a powerful tool to investigate the kesterite structure of the photovoltaic  $\text{Cu}_2\text{ZnSnS}_4$  compound *Acta Cryst.* **B70** 390
- [63] Valakh M Y, Dzhagan V M, Babichuk I S, Fontane X, Perez-Rodríguez A and Schorr S 2013 Optically induced structural transformation in disordered kesterite  $\text{Cu}_2\text{ZnSnS}_4$  *JETP Lett.* **98** 255
- [64] Caballero R, Garcia-Llamas E, Merino J M, León M, Babichuk I, Dzhagan V, Strelchuk V and Valakh M 2014 Non-stoichiometry effect and disorder in  $\text{Cu}_2\text{ZnSnS}_4$  thin films obtained by flash evaporation: Raman scattering investigation *Acta Mater.* **65** 412
- [65] Paris M, Choubrac L, Lafond A, Guillot-Deudon C and Jobic S 2014 Solid-state NMR and Raman spectroscopy to address the local structure of defects and the tricky issue of the Cu/Zn disorder in Cu-poor, Zn-rich CZTS materials *Inorg. Chem.* **53** 8646
- [66] Dimitrievska M, Fairbrother A, Saucedo E, Perez-Rodríguez A and Izquierdo-Roca V 2015 Influence of compositionally induced defects on the vibrational properties of device grade  $\text{Cu}_2\text{ZnSnSe}_4$  absorbers for kesterite based solar cells *Appl. Phys. Lett.* **106** 073903
- [67] Oliva F, Giraldo S, Dimitrievska M, Pistor P, Martínez-Pérez A, Calvo-Barrio L, Saucedo E, Perez-Rodríguez A and Izquierdo-Roca V 2017 Raman scattering assessment of point defects in kesterite semiconductors: UV resonant Raman characterization for advanced photovoltaics *IEEE 44th Photovolt. Spec. Conf. (PVSC)* **3285**
- [68] Dimitrievska M, Oliva F, Guc M, Giraldo S, Saucedo E, Pérez-Rodríguez A and Izquierdo-Roca V 2019 Defect characterisation in  $\text{Cu}_2\text{ZnSnSe}_4$  kesterites via resonant Raman spectroscopy and impact onto optoelectronic solar cells properties *J. Mater. Chem. A* accepted **7** 13293
- [69] Scragg J J S, Choubrac L, Lafond A, Ericson T and Platzer-Bjorkman C 2014 A low-temperature order-disorder transition in  $\text{Cu}_2\text{ZnSnS}_4$  thin films *Appl. Phys. Lett.* **104** 041911
- [70] Scragg J J S, Larsen J K, Kumar M, Persson C, Sandler J, Siebentritt S and Platzer Bjorkman C 2016 Cu–Zn disorder and band gap fluctuations in  $\text{Cu}_2\text{ZnSn}(\text{S},\text{Se})_4$ : Theoretical and experimental investigations *Phys. Status Solidi B* **253** 247
- [71] Chang I F and Mitra S S 1968 Application of a modified random-element-isodisplacement model to long-wavelength optic phonons of mixed crystals *Phys. Rev. B* **172** 924
- [72] Grossberg M, Timmo K, Raadik T, Kärber E, Mikli V and Krustok J 2015 Study of structural and optoelectronic properties of  $\text{Cu}_2\text{Zn}(\text{Sn}_{1-x}\text{Ge}_x)\text{Se}_4$  ( $x = 0$  to 1) alloy compounds *Thin Solid Films* **582** 176
- [73] Garcia-Llamas E, Merino J M, Serna R, Fontané X, Victorov I A, Pérez-Rodríguez A, León M, Bodnar I V, Izquierdo-Roca V and Caballero R 2016 Wide band-gap tuning  $\text{Cu}_2\text{ZnSn}_{1-x}\text{Ge}_x\text{S}_4$  single crystals: optical and vibrational properties *Sol. Energy Mater. Sol. Cells* **158** 147
- [74] Grossberg M, Krustok J, Raudoja J, Timmo K, Altosaar M and Raadik T 2011 Photoluminescence and Raman study of  $\text{Cu}_2\text{ZnSn}(\text{Se}_x\text{S}_{1-x})_4$  monograins for photovoltaic applications *Thin Solid Films* **519** 7403
- [75] Dimitrievska M, Gurieva G, Xie H, Carrete A, Cabot A, Saucedo E, Pérez-Rodríguez A, Schorr S and Izquierdo-Roca V 2015 Raman scattering quantitative analysis of the anion chemical composition in kesterite  $\text{Cu}_2\text{ZnSn}(\text{S}_x\text{Se}_{1-x})_4$  solid solutions *J. Alloy Compd.* **628** 464

- [76] Fernandes P A, Salomé P M P and da Cunha A F 2009 Growth and Raman scattering characterization of  $\text{Cu}_2\text{ZnSnS}_4$  thin films *Thin Solid Films* **517** 2519
- [77] Salomé P M P, Fernandes P A and da Cunha A F 2009 Morphological and structural characterization of  $\text{Cu}_2\text{ZnSnSe}_4$  thin films grown by selenization of elemental precursor layers *Thin Solid Films* **517** 2531
- [78] Fernandes P A, Salomé P M P and da Cunha A F 2011 Study of polycrystalline  $\text{Cu}_2\text{ZnSnS}_4$  films by Raman scattering *J. Alloy Compd.* **509** 7600
- [79] Fontané X, Calvo-Barrio L, Izquierdo-Roca V, Saucedo E, Pérez-Rodríguez A, Morante J R, Berg D M, Dale P J and Siebentritt S 2011 In-depth resolved Raman scattering analysis for the identification of secondary phases: characterization of  $\text{Cu}_2\text{ZnSnS}_4$  layers for solar cell applications *Appl. Phys. Lett.* **98** 181905
- [80] Berg D M, Arasimowicz M, Djemour R, Gütay L, Siebentritt S, Schorr S, Fontané X, Izquierdo-Roca V, Pérez-Rodríguez A and Dale P J 2014 Discrimination and detection limits of secondary phases in  $\text{Cu}_2\text{ZnSnS}_4$  using x-ray diffraction and Raman spectroscopy *Thin Solid Films* **569** 113
- [81] Fairbrother A, García-Hemme E, Izquierdo-Roca V, Fontané X, Pulgarín-Agudelo F A, Vigil-Galán O, Pérez-Rodríguez A and Saucedo E 2012 Development of a selective chemical etch to improve the conversion efficiency of Zn-rich  $\text{Cu}_2\text{ZnSnS}_4$  solar cells *J. Am. Chem. Soc.* **134** 8018
- [82] Fairbrother A, Izquierdo-Roca V, Fontané X, Ibáñez M, Cabot A, Saucedo E and Pérez-Rodríguez A 2014 ZnS grain size effects on near-resonant Raman scattering: optical non-destructive grain size estimation *Cryst. Eng. Comm.* **16** 4120
- [83] Fairbrother A et al 2014 Secondary phase formation in Zn-rich  $\text{Cu}_2\text{ZnSnSe}_4$ -based solar cells annealed in low pressure and temperature conditions *Prog. Photovoltaics Res. Appl.* **22** 479
- [84] Becerril-Romero I et al 2017 CZTSe solar cells developed on polymer substrates: Effects of low-temperature processing *Prog Photovoltaics Res. Appl.* **26** 55
- [85] Giraldo S et al 2018 How small amounts of Ge modify the formation pathways and crystallization of kesterites *Energy Environ. Sci.* **11** 582
- [86] Espindola-Rodríguez M, Sylla D, Sánchez Y, Oliva F, Grini S, Neuschitzer M, Vines L, Izquierdo-Roca V, Saucedo E and Placidi M 2017 Bifacial kesterite solar cells on FTO substrates *ACS Sustainable Chem. Eng.* **5** 11516
- [87] Hages C J, Levenco S, Miskin C K, Alsmeyer J H, Abou-Ras D, Wilks R G, Bär M, Unold T and Agrawal R 2015 Improved performance of Ge-alloyed CZTGeS<sub>2</sub> thin film solar cells through control of elemental losses *Prog. Photovoltaics Res. Appl.* **23** 376
- [88] Zhong J et al 2014 Sulfurization induced surface constitution and its correlation to the performance of solution-processed  $\text{Cu}_2\text{ZnSn(S,Se)}_4$  solar cells *Sci. Rep.* **4** 6288
- [89] Kim I, Kim K, Oh Y, Woo K, Cao G, Jeong S and Moon J 2014 Bandgap-graded  $\text{Cu}_2\text{Zn(Sn}_{1-x}\text{Ge}_x)_4$  thin-film solar cells derived from metal chalcogenide complex ligand capped nanocrystals *Chem. Mater.* **26** 3957
- [90] Ge J, Koirala P, Grice C R, Roland P J, Yu Y, Tan X, Ellingson R J, Collins R W and Yan Y 2017 Oxygenated CdS buffer layers enabling high open-circuit voltages in earth-abundant  $\text{Cu}_2\text{BaSnS}_4$  thin-film solar cells *Adv. Energy Mater.* **7** 1601803
- [91] Lie S, Tan J M R, Li W, Leow S W, Tay Y F, Bishop D M, Gunawan O and Wong L H 2018 Reducing interfacial defect density of CZTSSe solar cell by Mn substitution *J. Mater. Chem. A* **6** 1540
- [92] Caballero R, Haass S G, Andres C, Arques L, Oliva F, Izquierdo-Roca V and Romanyuk Y E 2018 Effect of magnesium incorporation on solution-processed kesterite solar cells *Front. Chem.* **6** 5
- [93] Grossberg M, Krustok J, Timmo K and Altosaar M 2009 Radiative recombination in  $\text{Cu}_2\text{ZnSnSe}_4$  monograins studied by photoluminescence spectroscopy *Thin Solid Films* **517** 2489
- [94] Luckert F et al 2011 Optical properties of high quality  $\text{Cu}_2\text{ZnSnSe}_4$  thin films *Appl. Phys. Lett.* **99** 062104
- [95] Gurieva G, Guc M, Bruk L I, Izquierdo-Roca V, Pérez Rodríguez A, Schorr S and Arushanov E 2013  $\text{Cu}_2\text{ZnSnS}_4$  thin films grown by spray pyrolysis: characterization by Raman spectroscopy and x-ray diffraction *Phys. Status Solidi C* **10** 1082
- [96] León M et al 2014 Spectroscopic ellipsometry study of  $\text{Cu}_2\text{ZnSnSe}_4$  bulk crystals *Appl. Phys. Lett.* **105** 061909
- [97] Caballero R, Victorov I, Serna R, Cano-Torres J M, Maffiotte C, Garcia-Llamas E, Merino J M, Valakh M, Bodnar I and Leon M 2014 Band-gap engineering of  $\text{Cu}_2\text{ZnSn}_{1-x}\text{Ge}_x\text{S}_4$  single crystals and influence of the surface properties *Acta Mater.* **79** 181
- [98] Semenenko M O, Babichuk I S, Kyriienko O, Bodnar I V, Caballero R and Leon M 2017 RF electromagnetic field treatment of tetragonal kesterite CZTSSe light absorbers *Nanoscale Res. Lett.* **12** 408
- [99] Neuschitzer M, Espindola-Rodríguez M, Guc M, Márquez Prieto J A, Giraldo S, Forbes I, Perez-Rodríguez A and Saucedo E 2018 Revealing the beneficial effects of Ge doping on  $\text{Cu}_2\text{ZnSnSe}_4$  thin film solar cells *J. Mater. Chem. A* **6** 11759
- [100] Levenco S et al 2018 Spectroscopic ellipsometry study of  $\text{Cu}_2\text{ZnSnS}_4$  bulk poly-crystals *Appl. Phys. Lett.* **112** 161901
- [101] Klavina I, Kaljuev T, Timmo K, Raudoja J, Traksmaa R, Altosaar M and Meissner D 2011 Study of  $\text{Cu}_2\text{ZnSnSe}_4$  monograin formation in molten KI starting from binary chalcogenides *Thin Solid Films* **519** 7399
- [102] Park D, Nam D, Jung S, An S J, Gwak J, Yoon K, Yun J H and Cheong H 2011 Optical characterization of  $\text{Cu}_2\text{ZnSnSe}_4$  grown by thermal co-evaporation *Thin Solid Films* **519** 7386
- [103] Cheng A-J, Manno M, Khare A, Leighton C, Campbell S A and Aydil E S 2011 Imaging and phase identification of  $\text{Cu}_2\text{ZnSnS}_4$  thin films using confocal Raman spectroscopy *J. Vac. Sci. Technol. A* **29** 051203
- [104] Fairbrother A, Fontané X, Izquierdo-Roca V, Espindola-Rodríguez M, Lopez-Marino S, Placidi M, Calvo-Barrio L, Perez-Rodríguez A and Saucedo E 2013 On the formation mechanisms of Zn-rich  $\text{Cu}_2\text{ZnSnS}_4$  films prepared by sulfurization of metallic stacks *Sol. Energy Mater. Sol. Cells* **112** 97
- [105] Xie H, Dimitrievska M, Fontané X, Sánchez Y, López-Marino S, Izquierdo-Roca V, Bermúdez V, Pérez-Rodríguez A and Saucedo E 2015 Formation and impact of secondary phases in Cu-poor Zn-rich  $\text{Cu}_2\text{ZnSn(S}_{1-y}\text{Se}_y)_4$  ( $0 \leq y \leq 1$ ) based solar cells *Sol. Energy Mater. Sol. Cells* **140** 289
- [106] Hernandez Martinez A, Placidi M, Arques L, Giraldo S, Sánchez Y, Izquierdo-Roca V, Pistor P, Valentini M, Malerba C and Saucedo E 2018 Insights into the formation pathways of  $\text{Cu}_2\text{ZnSnSe}_4$  using rapid thermal processes *ACS Appl. Energy Mater.* **1** 1981
- [107] Yoo H and Kim J H 2011 Comparative study of  $\text{Cu}_2\text{ZnSnS}_4$  film growth *Sol. Energy Mater. Sol. Cells* **95** 239
- [108] Shin S W, Pawar S M, Park C Y, Yun J H, Moon J-H, Kim J H and Lee J Y 2011 Studies on  $\text{Cu}_2\text{ZnSnS}_4$  (CZTS) absorber layer using different stacking orders in precursor thin films *Sol. Energy Mater. Sol. Cells* **95** 3202
- [109] Fairbrother A, Fourdrinier L, Fontané X, Izquierdo-Roca V, Dimitrievska M, Pérez-Rodríguez A and Saucedo E 2014 Precursor stack ordering effects in  $\text{Cu}_2\text{ZnSnSe}_4$  thin films prepared by rapid thermal processing *J. Phys. Chem. C* **118** 17291
- [110] Nama D, Cho S, Sim J-H, Yang K-J, Son D-H, Kim D-H, Kang J-K, Kwon M-S, Jeon C-W and Cheong H 2016 Solar conversion efficiency and distribution of ZnS secondary phase in  $\text{Cu}_2\text{ZnSnS}_4$  solar cells *Sol. Energy Mater. Sol. Cells* **149** 226
- [111] Guo B L, Chen Y H, Liu X J, Liu W C and Li A D 2014 Optical and electrical properties study of sol-gel derived  $\text{Cu}_2\text{ZnSnS}_4$  thin films for solar cells *AIP Adv.* **4** 097115

- [112] Nam D, Opanasyuk A S, Koval P V, Ponomarev A G, Jeong A R, Kim G Y, Jo W and Cheong H 2014 Composition variations in  $\text{Cu}_2\text{ZnSnSe}_4$  thin films analyzed by x-ray diffraction, energy dispersive x-ray spectroscopy, particle induced x-ray emission, photoluminescence, and Raman spectroscopy *Thin Solid Films* **562** 109
- [113] Chen Q, Bernardi S and Zhang Y 2017 Spatially resolved laser-induced modification Raman spectroscopy for probing the microscopic variations in the quaternary alloy  $\text{Cu}_2\text{ZnSnSe}_4$  *Phys. Rev. Appl.* **8** 034008
- [114] Dimitrievska M, Fairbrother A, Izquierdo-Roca V, Pérez-Rodríguez A and Saucedo E 2014 Two ideal compositions for kesterite-based solar cell devices *IEEE 40th Photovolt. Spec. Conf. (PVSC)* **2307**
- [115] Wei Z, Newman M J, Tsoi W C and Watson T M 2016 Raman mapping analysis for removal of surface secondary phases of CZTS films using chemical etching *Appl. Phys. Lett.* **109** 123902
- [116] Dimitrievska M, Fairbrother A, Saucedo E, Pérez-Rodríguez A and Izquierdo-Roca V 2016 Secondary phase and Cu substitutional defect dynamics in kesterite solar cells: Impact on optoelectronic properties *Sol. Energy Mater. Sol. Cells* **149** 304
- [117] Schöppe P, Schönherr S, Wuerz R, Wisniewski W, Martínez-Criado G, Ritzer M, Ritter K, Ronning C and Schnohr C S 2017 Rubidium segregation at random grain boundaries in  $\text{Cu}(\text{In,Ga})\text{Se}_2$  absorbers *Nano Energy* **42** 307
- [118] Schöppe P, Schönherr S, Jackson P, Wuerz R, Wisniewski W, Ritzer M, Zapf M, Johannes A, Schnohr C S and Ronning C 2018 Overall distribution of rubidium in highly efficient  $\text{Cu}(\text{In,Ga})\text{Se}_2$  solar cells *ACS Appl. Mater. Interfaces* **10** 40592
- [119] Schöppe P, Gurieva G, Giraldo S, Martínez-Criado G, Ronning C, Saucedo E, Schorr S and Schnohr C S 2017 Discrepancy between integral and local composition in off-stoichiometric  $\text{Cu}_2\text{ZnSnSe}_4$  kesterites: a pitfall for classification *Appl. Phys. Lett.* **110** 043901
- [120] Martínez-Criado G et al 2016 ID16B: a hard x-ray nanoprobe beamline at the ESRF for nano-analysis *J. Synchrotron Radiat.* **23** 344
- [121] Schwarz T, Cojocar-Mirédin O, Choi P-P, Mousel M, Redinger A, Siebentritt S and Raabe D 2013 Atom probe study of  $\text{Cu}_2\text{ZnSnSe}_4$  thin-films prepared by co-evaporation and post-deposition annealing *Appl. Phys. Lett.* **102** 042101
- [122] Schwarz T, Cojocar-Mirédin O, Mousel M, Redinger A, Raabe D and Choi P-P 2017 Formation of nanometer-sized Cu-Sn-Se particles in  $\text{Cu}_2\text{ZnSnSe}_4$  thin films and their effect on solar cell efficiency *Acta Mater.* **132** 276
- [123] Woo K, Kim Y, Yang W, Kim K, Kim I, Oh Y, Kim J Y and Moon J 2013 Band-gap-graded  $\text{Cu}_2\text{ZnSn}(\text{S}_{1-x}\text{Se}_x)_4$  solar cells fabricated by an ethanol-based, particulate precursor ink route *Sci. Rep.* **3** 3069
- [124] Aguiar J A, Erkan M E, Pruzan D S, Nagaoka A, Yoshino K, Moutinho H, Al-Jassim M and Scarpulla M A 2016 Cation ratio fluctuations in  $\text{Cu}_2\text{ZnSnS}_4$  at the 20nm length scale investigated by analytical electron microscopy *Phys. Status Solidi A* **213** 2392
- [125] Schnohr C S and Ridgway M C 2015 Introduction to x-ray absorption spectroscopy x-ray absorption spectroscopy of semiconductors ed C S Schnohr and M C Ridgway *Springer Series in Optical Sciences* vol 190 (Berlin: Springer) p 1
- [126] Just J, Lützenkirchen-Hecht D, Frahm R, Schorr S and Unold T 2011 Determination of secondary phases in kesterite  $\text{Cu}_2\text{ZnSnS}_4$  thin films by x-ray absorption near edge structure analysis *Appl. Phys. Lett.* **99** 262105
- [127] Just J, Sutter-Fella C M, Lützenkirchen-Hecht D, Frahm R, Schorr S and Unold T 2016 Secondary phases and their influence on the composition of the kesterite phase in CZTS and CZTSe thin films *Phys. Chem. Chem. Phys.* **18** 15988
- [128] Siah S C, Jaramillo R, Chakraborty R, Erslev P T, Sun C-J, Weng T-C, Toney M F, Teeter G and Buonassisi T 2015 X-ray absorption spectroscopy study of structure and stability of disordered  $(\text{Cu}_2\text{SnS}_3)_{1-x}(\text{ZnS})_x$  alloys *IEEE J. Photovoltaics* **5** 372
- [129] Colina-Ruiz R A, Mustre de León J, Lezama-Pacheco J S, Caballero-Briones F, Acosta-Alejandro M and Espinosa-Faller F J 2017 Local atomic structure and analysis of secondary phases in non-stoichiometric  $\text{Cu}_2\text{ZnSnS}_4$  using x-ray absorption fine structure spectroscopy *J. Alloys Compd.* **714** 381
- [130] Just J, Lützenkirchen-Hecht D, Müller O, Frahm R and Unold T 2017 Depth distribution of secondary phases in kesterite  $\text{Cu}_2\text{ZnSnS}_4$  by angle-resolved x-ray absorption spectroscopy *APL Mater.* **5** 126106
- [131] Toyama T, Konishi T, Seo Y, Tsuji R, Terai K, Nakashima Y, Okamoto H and Tsutsumi Y 2013 Grain growth in  $\text{Cu}_2\text{ZnSnS}_4$  thin films using sn vapor transport for photovoltaic applications *Appl. Phys. Exp.* **6** 075503
- [132] Ji S, Shi T, Qiu X, Zhang J, Xu G, Chen C, Jiang Z and Ye C 2013 A route to phase controllable  $\text{Cu}_2\text{ZnSn}(\text{S}_{1-x}\text{Se}_x)_4$  nanocrystals with tunable energy bands *Sci. Rep.* **3** 2733
- [133] Ritscher A, Just J, Dolotko O, Schorr S and Lerch M 2016 A mechanochemical route to single phase  $\text{Cu}_2\text{ZnSnS}_4$  powder *J. Alloys Compd.* **670** 289
- [134] Melitz W, Shen J, Kummel A C and Lee S 2011 Kelvin probe force microscopy and its application *Surf. Sci. Rep.* **66** 1–27
- [135] Sadewasser S, Glatzel T, Rusu M, Jäger-Waldau A and Lux-Steiner M C 2002 High-resolution work function imaging of single grains of semiconductor surfaces *Appl. Phys. Lett.* **80** 2979
- [136] Vishwakarma M, Varandani D, Andres C, Romanyuk Y E, Haass S G, Tiwari A N and Mehta B R 2018 A direct measurement of higher photovoltage at grain boundaries in  $\text{CdS}/\text{CZTSe}$  solar cells using KPFM technique *Sol. Energy Mater. Sol. Cells* **183** 34–40
- [137] Kim J, Kim G Y, Jo W, Yang K-J, Sim J-H, Kim D-H and Kang J-K 2016 Effects of Mo back-contact annealing on surface potential and carrier transport in  $\text{Cu}_2\text{ZnSnS}_4$  thin film solar cells *RSC Adv.* **6** 103337–45
- [138] Sardashti K, Haight R, Gokmen T, Wang W, Chang L-Y, Mitzi D B and Kummel A C 2015 Impact of nanoscale elemental distribution in high-performance kesterite solar cells *Adv. Energy Mater.* **5** 1402180
- [139] Muhunthan N, Singh O P, Toutam V and Singh V N 2015 Electrical characterization of grain boundaries of CZTS thin films using conductive atomic force microscopy techniques *Mater. Res. Bull.* **70** 373–8
- [140] Kim J, Kim G Y, Son D-H, Yang K-J, Kim D-H, Kang J-K and Jo W 2018 High photo-conversion efficiency  $\text{Cu}_2\text{ZnSn}(\text{S,Se})_4$  thin-film solar cells prepared by compound-precursors and metal-precursors *Sol. Energy Mater. Sol. Cells* **183** 129–36
- [141] Yang K-J, Kim S, Sim J-H, Son D-H, Kim D-H, Kim J, Jo W, Yoo H, Kim J H and Kang J-K 2018 The alterations of carrier separation in kesterite solar cells *Nano Energy* **52** 38–53
- [142] Xin H, Vorpahl S M, Collord A D, Braly I L, Uhl A R, Krueger B W, Ginger D S and Hillhouse H W 2015 Lithium-doping inverts the nanoscale electric field at the grain boundaries in  $\text{Cu}_2\text{ZnSn}(\text{S,Se})_4$  and increases photovoltaic efficiency *Phys. Chem. Chem. Phys.* **17** 23859–66
- [143] Kim G Y, Son D-H, Nguyen T T T, Yoon S, Kwon M, Jeon C-W, Kim D-H, Kang J-K and Jo W 2016 Enhancement of photo-conversion efficiency in  $\text{Cu}_2\text{ZnSn}(\text{S,Se})_4$  thin-film solar cells by control of ZnS precursor-layer thickness *Prog. Photovoltaics Res. Appl.* **24** 292–306
- [144] Vishwakarma M, Varandani D, Shivaprasad S M and Mehta B R 2018 Structural, optical, electrical properties and energy band diagram of  $\text{Cu}_2\text{ZnSiS}_4$  thin films *Sol. Energy Mater. Sol. Cells* **174** 577–83
- [145] Gupta S, Varandani D, Sharma A K, Satsangi V R and Mehta B R 2015 Nanoscale interface mapping of a  $\text{CdS}-\text{CZTS}$  single nanorod heterojunction using Kelvin probe force microscopy *Appl. Surf. Sci.* **331** 327–32
- [146] Sardashti K, Chagarov E, Antunez P D, Gershon T S, Ueda S T, Gokmen T, Bishop D, Haight R and Kummel A C 2017 Nanoscale characterization of back surfaces and interfaces in thin-film kesterite solar cells *ACS Appl. Mater. Interfaces* **9** 17024–33
- [147] Chen S, Gong X G, Walsh A and Wei S-H 2009 Crystal and electronic band structure of  $\text{Cu}_2\text{ZnSnX}_4$  ( $X = \text{S}$  and  $\text{Se}$ ) photovoltaic absorbers: first-principles insights *Appl. Phys. Lett.* **94** 041903

- [148] Chen S, Gong X G, Walsh A and Wei S-H 2009 Electronic structure and stability of quaternary chalcogenide semiconductors derived from cation cross-substitution of II–VI and I–III–VI<sub>2</sub> compounds *Phys. Rev. B* **79** 165211
- [149] Chen S, Gong X G, Walsh A and Wei S-H 2010 Defect physics of the kesterite thin-film solar cell absorber Cu<sub>2</sub>ZnSnS<sub>4</sub> *Appl. Phys. Lett.* **96** 021902
- [150] Ozaki S and Namba T 2012 Optical properties and electronic band structure of Cu<sub>2</sub>ZnSnSe<sub>4</sub> kesterite semiconductor *Phys. Status Solidi C* **9** 2403
- [151] Choi S G, Zhao H Y, Persson C, Perkins C L, Donohue A L, To B, Norman A G, Li J and Repins I L 2012 Dielectric function spectra and critical-point energies of Cu<sub>2</sub>ZnSnSe<sub>4</sub> from 0.5 to 9.0 eV *J. Appl. Phys.* **111** 033506
- [152] Li W, Jiang K, Zhang J, Chen X, Hu Z, Chen S, Sun L and Chu J 2012 Temperature dependence of phonon modes, dielectric functions, and interband electronic transitions in Cu<sub>2</sub>ZnSnS<sub>4</sub> semiconductor films *Phys. Chem. Chem. Phys.* **14** 9936
- [153] Chen D and Ravindra N M 2013 Electronic and optical properties of Cu<sub>2</sub>ZnGeX<sub>4</sub> (X = S, Se and Te) quaternary semiconductors *J. Alloys Compd.* **579** 468
- [154] Choi S G, Park J-S, Donohue A L, Christensen S T, To B, Beall C, Wei S-H and Repins I L 2015 Electronic structure and optical properties of Cu<sub>2</sub>ZnGeSe<sub>4</sub>: first-principles calculations and vacuum-ultraviolet spectroscopic ellipsometric studies *Phys. Rev. Appl.* **4** 054006
- [155] Sun L, He J, Chen Y, Yue F, Yang P and Chu J 2012 Comparative study on Cu<sub>2</sub>ZnSnS<sub>4</sub> thin films deposited by sputtering and pulsed laser deposition from a single quaternary sulfide target *J. Cryst. Growth* **361** 147
- [156] Hirate Y, Tampo H, Minoura S, Kadowaki H, Nakane A, Kim K M, Shibata H, Niki S and Fujiwara H 2015 Dielectric functions of Cu<sub>2</sub>ZnSnSe<sub>4</sub> and Cu<sub>2</sub>SnSe<sub>3</sub> semiconductors *J. Appl. Phys.* **117** 015702
- [157] Botti S, Kammerlander D and Marques M A L 2011 Band structures of Cu<sub>2</sub>ZnSnS<sub>4</sub> and Cu<sub>2</sub>ZnSnSe<sub>4</sub> from many-body methods *Appl. Phys. Lett.* **98** 241915
- [158] Crovetto A, Cazzaniga A, Ettliger R B, Schou J and Hansen O 2015 Optical properties and surface characterization of pulsed laser-deposited Cu<sub>2</sub>ZnSnS<sub>4</sub> by spectroscopic ellipsometry *Thin Solid Films* **582** 203
- [159] León M, Levchenko S, Serna R, Gurieva G, Nateprov A, Merino J M, Friedrich E J, Fillat U, Schorr S and Arushanov E 2010 Optical constants of Cu<sub>2</sub>ZnGeS<sub>4</sub> bulk crystals *J. Appl. Phys.* **108** 093502
- [160] León M, Levchenko S, Serna R, Nateprov A, Gurieva G, Merino J M, Schorr S and Arushanov E 2013 Spectroscopic ellipsometry study of Cu<sub>2</sub>ZnGeSe<sub>4</sub> and Cu<sub>2</sub>ZnSiSe<sub>4</sub> poly-crystals *Mater. Chem. Phys.* **141** 58
- [161] Garcia-Llamas E, Merino J M, Serna R, Fontané X, Victorov I A, Pérez-Rodríguez A, León M, Bodnar I V, Izquierdo-Roca V and Caballero R 2016 Wide band-gap tuning Cu<sub>2</sub>ZnSn<sub>1-x</sub>Ge<sub>x</sub>S<sub>4</sub> single crystals: optical and vibrational properties *Sol. Energy Mater. Sol. Cells* **158** 147
- [162] Caballero R, Victorov I A, Serna R, Cano-Torres J M, Maffiotte C, Garcia-Llamas E, Merino J M, Valakh M, Bodnar I V and León M 2014 Band-gap engineering of Cu<sub>2</sub>ZnSn<sub>1-x</sub>Ge<sub>x</sub>S<sub>4</sub> single crystals and influence of the surface properties *Acta Mater.* **79** 181
- [163] Sengar B S, Garg V, Awasthi V, Aaryashree, Kumar S, Mukherjee C, Gupta M and Mukherjee S 2016 Growth and characterization of dual ion beam sputtered Cu<sub>2</sub>ZnSn(S, Se)<sub>4</sub> thin films for cost-effective photovoltaic application *Sol. Energy* **139** 1
- [164] Schorr S 2007 Structural aspects of adamantane like multinary chalcogenides *Thin Solid Films* **515** 5985
- [165] Litvinchuk A P 2016 Optical properties and lattice dynamics of Cu<sub>2</sub>ZnGeSe<sub>4</sub> quaternary semiconductor: a density-functional study *Phys. Status Solidi B* **253** 323
- [166] Ming T, Weller M T, Kissling G P, Peter L M, Dale P, Babbe F, de Wild J, Wenger B, Snaith H J and Lane D 2017 Optoelectronic and spectroscopic characterization of vapour-transport grown Cu<sub>2</sub>ZnSnS<sub>4</sub> single crystals *J. Mater. Chem. A* **5** 1192
- [167] Crovetto A, Cazzaniga A, Ettliger R B, Schou J and Hansen O 2018 Large process-dependent variations in band alignment and interface band gaps of Cu<sub>2</sub>ZnSnS<sub>4</sub>/CdS solar cells *Sol. Energy Mater. Sol. Cells* **187** 233
- [168] Li S-Y, Häggglund C, Ren Y, Scragg J J S, Larsen J K, Frisk C, Rudisch K, Englund S and Platzter-Björkman C 2016 Optical properties of reactively sputtered Cu<sub>2</sub>ZnSnS<sub>4</sub> solar absorbers determined by spectroscopic ellipsometry and spectrophotometry *Sol. Energy Mater. Sol. Cells* **149** 170